Immunogenic calreticulin signaling in lung and glioblastoma cancer cells after x-ray and proton irradiation

Protocol development and optimization

MSc Project

Emma Kim Thingstad

Department of Physics
Faculty of Mathematics and Natural Sciences

UNIVERSITY OF OSLO

November / 2019

Acknowledgements

First and foremost, I would like to thank my supervisors Nina F. Edin, Eirik Malinen and Sunniva Siem. A special thanks to Nina for professional advices, but also ongoing support, patience and understanding. Also, I would like to thank Joe A. Sandvik for assistance in the cell lab throughout the last year.

Thanks to Adrian E. Mariampillai and Randi G. Syljuåsen for providing a protocol for the detection of calreticulin that served as a basis for further protocol development used in this thesis, and for the exchange of ideas in interpreting the results of experiments.

I would also like to thank Anne Marit Rykkelid for all her advices, and for ensuring that things went smoothly during proton irradiation experiments. Thank you also to Vera H. Tormodsrud for company throughout five years of studies.

Abstract

The use of immunotherapy in cancer treatment has emerged as a field with promising potential over the past decades. However, we are just in the beginning of understanding the mechanisms in which the immune system can be triggered to attack cancer cells. One such mechanism is induction of immunogenic cell death by irradiation.

Radiation has been shown to induce immunogenic cell death in which the dying cells sends out danger signals (DAMPs) that function as an ‘eat me’ signal for the immune system. One such DAMP is membrane-bound calreticulin after translocation from inside the cell.

This thesis aimed to measure membrane-bound calreticulin in T98G (human glioblastoma) and A549 (human lung carcinoma) cells as a function of dose and linear energy transfer (LET). The cells were irradiated with either x-rays or protons using different doses and dose fractions. The LET of the proton irradiation was varied by positioning the cells at the front of or at the back of the Bragg peak. The cells were analyzed 48 hours post-irradiation and the calreticulin signal was measured by flow cytometry.

A number of experiments were conducted before it was discovered that reproducibility of the results was generally lacking. A background signal made large contributions to the fluorescence detected and this background signal was increased by irradiation. This questioned the integrity of the results to such a degree that it could not be concluded that it was calreticulin that was being measured. A lot of effort was therefore put into identification of artefacts and optimization of the protocol, and autofluorescence was identified as a main contributor to the measured fluorescence.

A change of antibody to a fluorochrome-conjugated antibody finally appeared to improve the reliability of the results even though there still was a problem with background fluorescence. Consequently, only the proton data obtained in the last experiment are trusted to generate reliable results. From these data, it was seen that A549 cells generally have a stronger membrane-bound calreticulin signal response to irradiation than T98G cells. When the data were analyzed by linear regression, statistically significant dose- and LET-dependencies were found for both T98G and A549 cells. Multivariate regression gave even stronger correlations, indicating that the measured fluorescence from the calreticulin-binding antibody was dependent on both dose and LET.

Sammendrag

Immunterapi innen kreftbehandling har vist seg å være et felt med lovende potensial de siste tiårene. Imidlertid er vi bare i begynnelsen av å forstå mekanismene som aktiverer immunforsvaret til å angripe kreftceller. En slik mekanisme er induksjon av immunogen celledød ved bestråling.

Stråling har vist seg å indusere immunogen celledød der de døende cellene sender ut faresignaler (DAMPs) som fungerer som et 'spis meg' signal for immunforsvaret. Et eksempel på et slikt signal er membranbundet calreticulin som emigrerer fra innsiden av cellen til celleoverflaten.

Denne oppgaven tok sikte på å måle membranbundet calreticulin i T98G (humant glioblastom) og A549 (humant lungekarsinom) celler som en funksjon av dose og lineær energioverføring (LET). Cellene ble bestrålt med røntgenstråler eller protoner ved forskjellige doser og dosefraksjoner. Variasjonen i LET ved protonbestråling ble kontrollert ved å plassere cellene foran eller bakerst i Bragg-toppen. Cellene ble analysert 48 timer etter bestråling og calreticulin-signalet ble målt ved flow cytometri.

Flere eksperimenter ble utført før det ble oppdaget at reproduserbarheten av resultatene generelt manglet. Et bakgrunnssignal ga store bidrag til den detekterte fluorescensen, og dette bakgrunnssignalet økte ved bestråling. Dette sådde tvil om integriteten i resultatene til en slik grad at det ikke kunne konkluderes med at det var calreticulin som ble målt. Det ble derfor lagt ned mye arbeid i å identifisere artefakter og optimalisere protokollen, og autofluorescens ble identifisert som en hovedbidragsyter til den målte fluorescensen.

Ved å endre antistoffet fra ukonjugert antistoff til fluorokrom-konjugert antistoff så det ut til at påliteligheten til resultatene ble forbedret, selv om det fremdeles var et problem med bakgrunnsfluorescens. Følgelig er det bare proton-dataene som ble målt i det siste eksperimentet som kan sies å ha gitt pålitelige resultater. Fra disse dataene ble det observert at A549-celler generelt har en sterkere membranbundet calreticulin-signalrespons ved bestråling enn T98G-celler. Når dataene ble analysert ved lineær regresjon, ble det funnet en statistisk signifikant dose- og LET-avhengighet for både T98G og A549 celler. Multippel regresjon ga enda sterkere korrelasjoner, noe som indikerte at den målte fluorescensen fra det calreticulin-bindende antistoffet var avhengig av både dose og LET.

Table of Contents

Abbreviations

LET – linear energy transfer	**DAMP** – damage associated molecular patterns
RBE – relative biological effect	**ICD** – immunogenic cell death
CRT - calreticulin	**HMGB1** – high mobility group-box 1
NOD – net optical density	**FACS** – fluorescence-activated cell sorting
SSB – single-strand break	**CA** – chromosomal aberrations
DSB – double-strand break	**ATP** – adenosine triphosphate
UV - ultraviolet	**DC** – dendritic cells
BER – base excision repair	**ER** – endoplasmic reticulum
NER – nucleotide excision repair	**FSC** – forward scatter
HRR – homologous recombination repair	**SSC** – side scatter
NHEJ – nonhomologous end joining	**PD** – photo diode
IC – ionization chamber	**PMT** – photo multiplier tube

MC – monitor chamber	**AB** - antibody
SSD – source-skin distance	**OCL** – Oslo Cyclotron Laboratory
LAF-bench – laminar air flow-bench	**PBS** – phosphate-buffered saline
BSA – bovine serum albumin	**BED** – biological effective dose
PI – propidium iodine	**FAD** – flavin nucleotide cofactor
NADH – the reduced nicotinamide adenine dinucleotide	

1 Introduction

The use of radiotherapy, chemotherapy and surgery has long been the standard of treatment in many cancer types. In recent years, immunotherapy has emerged as a fourth pillar in cancer treatment. However, immunotherapy only works for a limited number of patients. As part of cancer development, cancer cells with an ability to evade immune detection are selected. Immunotherapy targets the control system that prevent autoimmune responses (Tormoen, 2018) . It is believed that the patients that benefit from immunotherapy are those that already have an immunogenic tumor signature possibly through a high mutation rate, which allows the immune system to detect the cancer cells.

The basis for radiotherapy is that radiation induces DNA double-strand breaks with subsequent death of the cell. However, in addition to the direct effect of cell kill, there have been observations of a so-called abscopal effect, in which tumors outside the radiation field were eradicated. The observed abscopal effect was first identified by Mole et al in 1953 but has only recently been connected to the induction of immunogenicity resulting in a tumor-immune response to irradiation (Ko, 2018). This has led to a new understanding of how radiation can be used to improve the efficacy of immunotherapy.

Several investigations have reported the use of radiotherapy as an inducer of immunogenic cell death, in which signals are sent from the dying cancer cell to the immune system. These signals have been reported to include cell surface translocation of calreticulin (CRT) and the extracellular release of HMGB1 and ATP. For instance, Golden et al. (2014), found that there was a dose-dependent increase in cell-surface calreticulin when the cells (TSA mammary carcinoma) were treated with x-ray radiotherapy (Golden, 2014). Although most studies are based on x-ray irradiation, there are also examples of studies using particle irradiation. An investigation of prostate (LNCap) carcinoma cells treated with 10 Gy of ^{223}Ra found that the surface translocation of calreticulin increased compared to untreated cells (Malamas, 2016). In addition, Gameiro et al. were able to show that 8 Gy proton irradiation increased the cell surface translocation of calreticulin in several carcinoma cell lines (lung, prostate, breast) – similar to those cells treated with 8 Gy photon irradiation (Gameiro, 2016). However, Gameiro et al. used 200 MeV protons and a RBE conversion factor of 1.1.

Norway will get its first proton therapy center in 2023. Protons deposit their energy differently than conventional X-rays, in particular at the end of the track there is a region (the Bragg peak) where most of the dose is deposited. As the dose falls off at the end of the Bragg peak, it has a higher relative efficiency due to an increase in linear energy transfer (LET). In the present experiments, we aimed to investigate if this difference could influence the induction of immunogenic cell death. The cell surface translocation of calreticulin induced by low energy (15 MeV) protons was compared to x-rays. By irradiating the cells at the front of the Bragg peak and at the back of the Bragg peak, the effect of LET in the track of the proton beam could be observed. In that way, the dependence of calreticulin signal on both dose and LET could be investigated.

2 Theory

2.1 Radiation Physics

2.1.1 Ionizing and non-ionizing radiation

Our knowledge of ionizing radiation started with the discovery of x-rays by Wilhelm Röntgen in 1895 (Röntgen, 1895) and the discovery of radioactivity by Henri Becquerel in 1896. Radiation physics can be divided into two main categories; ionizing radiation and non-ionizing radiation. In short, non-ionizing radiation represents the electromagnetic radiation that carries insufficient amounts of energy to ionize an atom or molecule. Ionizing radiation on the other hand, encompasses the part of the electromagnetic spectrum containing energies high enough to ionize atoms and molecules, in addition to particle radiation such as protons, α-particles, neutrons etc. It is further divided into directly and indirectly ionizing radiation; directly ionizing radiation involves a direct process comprising the deposition of energy in the absorber through many, small Coulomb-interactions between the ionizing charged particle and orbital electrons (Podgorsak, 2010) . Indirectly ionizing radiation such as photons and neutrons, ionize in a secondary process, meaning that they first interact with - and set in motion - a charged particle, which in turn deposits its energy in matter. Such indirectly ionizing radiations deposit their energy in a few, large interactions.

2.1.2 Interactions in matter

Photons

In this chapter (2.1) the following sections are based upon "Radiation Physics for Medical Physicists" (Podgorsak, 2010) and "Handbook of Radiotherapy Physics, Theory and Practice" (Mayles, 2007).

When photons interact with the absorbing medium in which they traverse, it is either with the orbital electrons or the nuclei of the atom. When the interaction is with orbital electrons, it can be either with a loosely bound electron, meaning that the binding energy, E_B, of the electron is much smaller than that of the incoming photon energy, $h\nu$, giving $E_B << h\nu$ (Thompson scattering, Compton scattering or triplet production), or the interaction can be with a tightly

bound electron where $E_B \lesssim h\nu$ (photoelectric effect, Rayleigh scattering). The nuclear interactions on the other hand, can be direct photo-nucleus (photodisintegration) or with the electrostatic field of the nucleus (pair production).

The photon interactions of most importance in medical physics and radiation dosimetry include photoelectric effect, Compton scattering and pair production.

Photoelectric effect:

When an incoming photon interacts with a tightly bound orbital electron of the absorber, the effect is said to be photoelectric. The incoming photon with energy $h\nu$, is completely absorbed, and the orbital electron is ejected with a kinetic energy E_K, corresponding to the initial energy of the incoming photon, minus the binding energy, E_B, of the electron. The concept is illustrated in Figure 1.

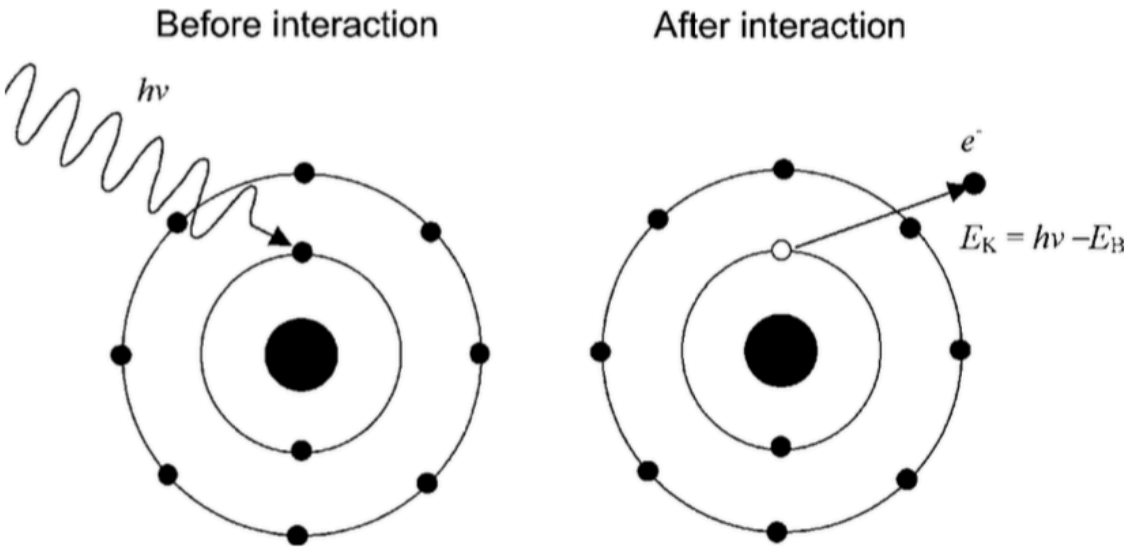

Figure 1 The photoelectric effect; the incoming photon with energy $h\nu$ is completely absorbed, and a tightly bound, orbital electron is ejected with kinetic energy, E_K (Podgorsak, 2010)

After the photoelectric absorption has taken place, the atom is left with a vacancy caused by the departure of the accelerated electron. Subsequently, an electron from an outer shell will fill this vacancy, resulting in the emission of energy corresponding to the difference in binding energy between the two shells. The release of this energy can be carried away by the emission of a photon or an electron.

The atomic cross section, τ^a, for photoelectric effect is

$$\tau^a \propto \frac{Z^4}{(h\upsilon)^3}$$

where Z is the atomic number of the absorbing material, and hν is the photon energy. As a consequence, photoelectric effect has a high cross section at low photon energies and for high Z materials.

Compton scattering:

Also known as incoherent scattering, Compton scattering builds on the assumption that a photon interacts with a free and stationary electron. This assumption is made due to the high speed and energy of the incoming photon, relative to that of the electron. As the incoming photon with an energy hν interacts with the electron, the photon is scattered with a new energy hν', and the recoil electron that is ejected from the atom receives a kinetic energy E_K (Figure 2). The scattering angle between the path of the incident photon and the scattered photon is referred to as θ, and the angle between the incident photon and the ejected electron is ϕ.

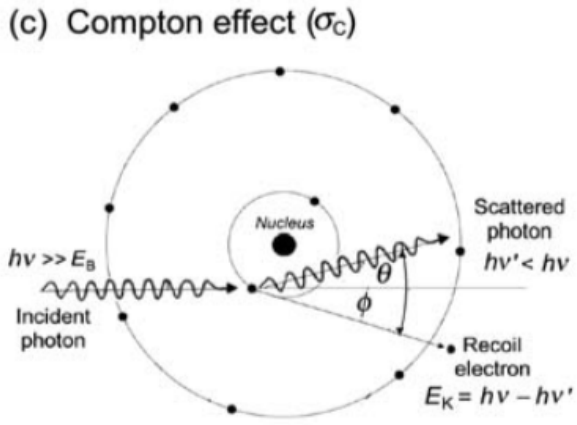

Figure 2 The Compton effect; the incoming photon with energy, hν, interacts with the loosely bound electron and is scattered with a new energy hν'. The electron is ejected from the atom with the kinetic energy E_K = hν - hν' (Podgorsak, 2010)

The atomic cross section, $\sigma_C{}^a$, for Compton scattering is

$$\sigma_C{}^a \propto Z$$

and comprise the most important photon interaction for the energies used in clinical radiotherapy today.

Pair production:

In the case where the incoming photon has an energy exceeding 1.02 MeV, which is the sum of the rest energy of an electron-positron pair, it becomes energetically possible for such a pair to be produced. The criteria for this to occur, is that energy, charge and momentum is conserved. In the electric field of the nucleus, the photon is absorbed, and the electron-positron pair is emitted (Figure 3).

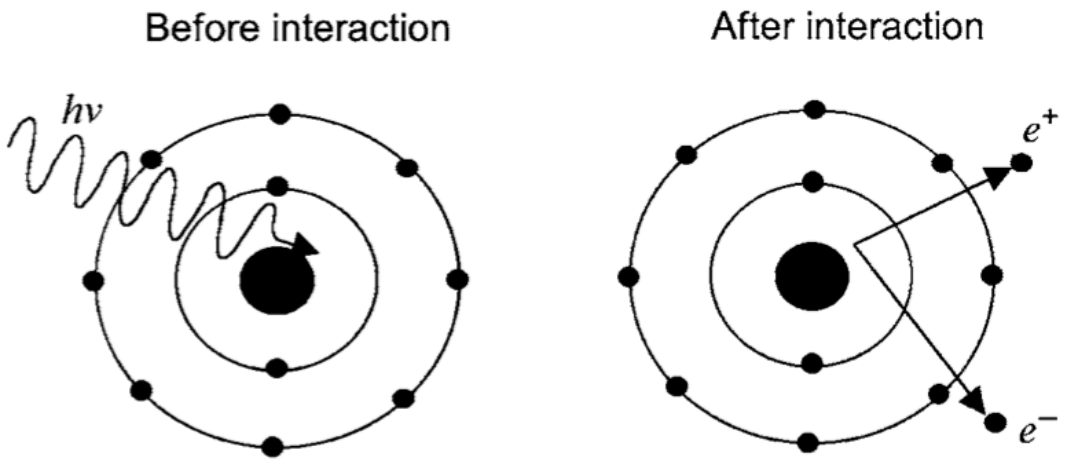

Figure 3 Pair production; the incoming photon with an energy > 1.02 MeV interacts with the electric field of the nucleus and is absorbed, followed by the creation of an electron-positron pair (Podgorsak, 2010)

The atomic cross section, κ^a, for pair production is zero at low energies (below threshold), and then increases rapidly at higher energies;

$$\kappa^a \propto Z^2$$

Mass attenuation, energy transfer and energy absorption coefficients:

In characterizing the penetration of photon rays into an absorbing medium we define the linear attenuation coefficient, μ. It is dependent on the energy of the photon beam, and the material (atomic number) of the absorber and gives an estimate of the probability per unit length of an interaction taking place. The **linear attenuation coefficient** has the unit m^{-1}. In many cases, however, it is preferable to talk about the **mass attenuation coefficient**, μ_m, which is found by dividing the linear attenuation coefficient, μ, by the mass density, ρ, of the absorbing material, making it independent of the absorber density. The unit is given as m^2/kg or cm^2/g.

If we call the linear attenuation coefficient for the photoelectric effect, the Compton effect, the Rayleigh scattering and pair production τ, σ_R, σ_C, κ respectively, the total mass attenuation coefficient representing the sum of the individual contributions can be written as:

$$\frac{\mu}{\rho} = \sum_i \left(\frac{\mu}{\rho}\right)_i = \frac{1}{\rho}(\tau + \sigma_R + \sigma_C + \kappa)$$

The total mass attenuation coefficient, $\frac{\mu}{\rho}$ can be seen for carbon (Figure 4) and lead (Figure 5).

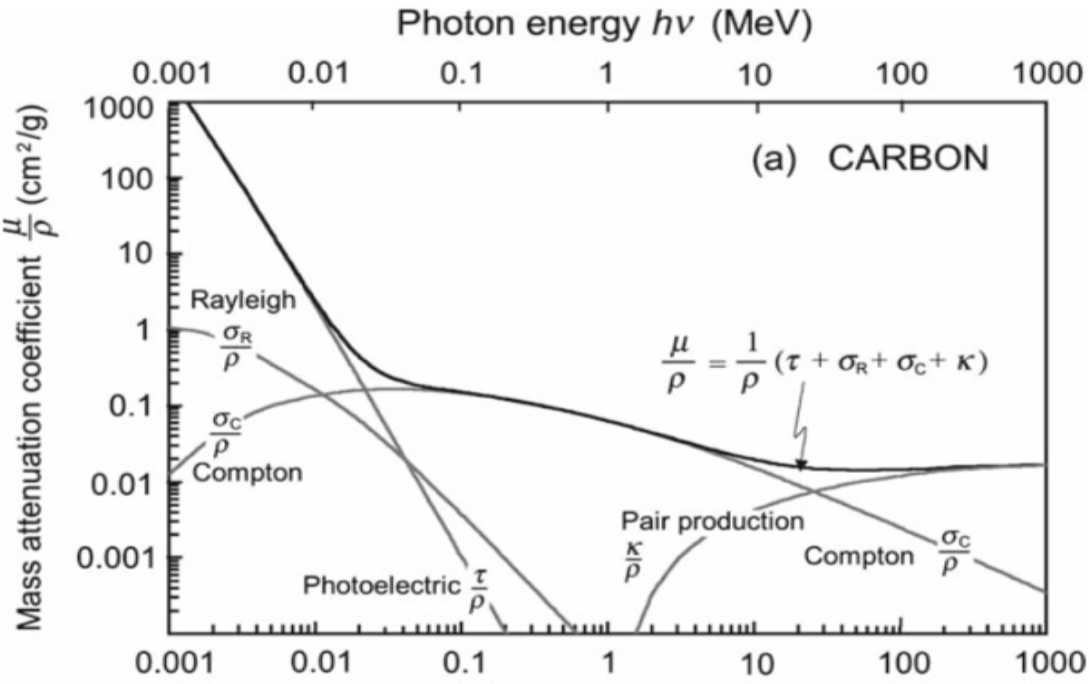

Figure 4 The mass attenuation coefficient for carbon as a function of photon energy (MeV). The individual coefficients for Rayleigh, Compton, photoelectric effect and pair production are also shown (Podgorsak, 2010)

Carbon is a low atomic number absorber and shows a different total mass attenuation coefficient than lead, which is an absorber of high atomic number. For any absorber material, the photoelectric effect predominates for lower photon energies. The mass attenuation contribution from the Compton effect, $\frac{\sigma_C}{\rho}$, is greater at intermediate photon energies and the width of the Compton scatter region is larger the lower the atomic number of the absorber material. For water and tissue the Compton region ranges from 20 keV to 20 MeV making it the most relevant photon interaction in clinical radiotherapy. For higher energies above 10 MeV pair production dominates. The mass coefficient for Rayleigh scattering only plays a secondary role for all energies.

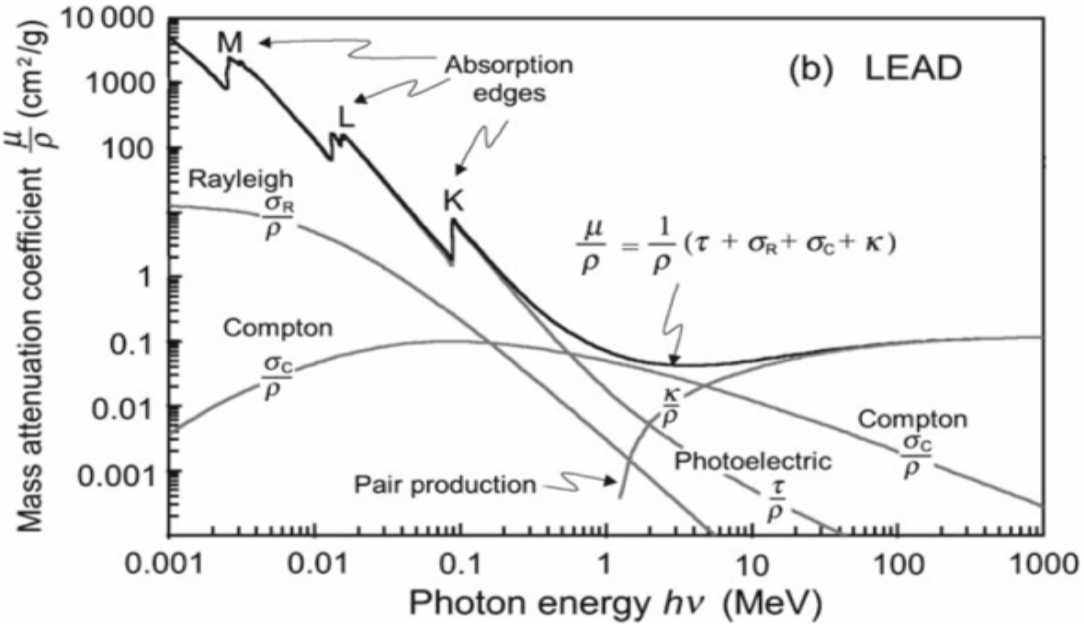

Figure 5 The mass attenuation coefficient for lead. Shown are also the individual coefficients for Rayleigh, Compton, pair production and photoelectric effect (Podgorsak, 2010)

The kinetic energy that is transferred to the secondary electrons through the photon interactions is useful in dosimetry because these secondary electrons impart their energy close to where they were released. The **total mass energy transfer coefficient**, $\frac{\mu_{tr}}{\rho}$, is defined as:

$$\frac{\mu_{tr}}{\rho} = \frac{\mu}{\rho}\frac{\langle T \rangle}{h\nu}$$

Where $\langle T \rangle$ is the expectation value of the kinetic energy gained by the secondary electrons, and $\frac{\mu_{tr}}{\rho}$ represents the sum of the individual contributions of the different photon interactions.

However, as the electrons are slowing down they may lose energy to secondary photons. The **total mass energy absorption coefficient** for all types of photon interactions takes this into account:

$$\frac{\mu_{en}}{\rho} = \frac{\mu_{tr}}{\rho}(1 - \delta)$$

Where δ represents the fraction of the kinetic energy of the secondary electrons that is lost to photons through bremsstrahlung and in-flight annihilation.

Charged particles:

As previously mentioned, charged particles deposit their energy through Coulomb-interactions when traversing matter (Podgorsak, 2010). The Coulomb scattering between two charged particles - a projectile and a target, have been the subject of several scientific experiments in the past.

One famous experiment of historical importance that lay the groundwork for our understanding of how the atom is built up, was the experiment of Geiger and Marsden under the supervision of Ernest Rutherford of 1909 called "*On a Diffuse Reflection of the α-Particles*". In this experiment, Geiger and Marsden scattered 5.5 MeV α-particles on a thin gold foil and used a microscope to measure the scattered particles by counting the scintillations produced in a zinc sulphide (ZnS) receptor (Geiger, 1909). By looking at the angular distribution of these scattered particles, Rutherford concluded that the major part of the atomic mass and positive charge were concentrated in its center – the mass nucleus (Podgorsak, 2010). This experiment lay the foundation for Rutherfords scattering theory for charged particles, which in turn has formed the basis of other theories developed over the years adding correction factors to Rutherfords original scattering theory (Podgorsak, 2010).

The Coulomb-force interactions of charged particles are classically characterized by the impact parameter, *b*, describing the distance a charge particle passes the atom of interaction vs. the atomic radius, *a* (Attix, 1986). Three cases are emphasized in this context;

b >> a (soft collision); refers to when the charged particle passes the atom at a large distance, interacting with the atom as a whole. In such cases, the result is excitation or in some cases ionization by ejection of a valence (loosely bound) electron. Only a small transfer of energy to the absorbing medium occurs in such soft collisions. This is the most probable interaction type out of the three, and accounts for about half of the total energy transfer to the absorber.

b ≈ a (hard collision); when the incoming particle strikes close to the atoms of the absorbing medium, the interaction that takes place is with a single electron of the atom, providing the electron with a high amount of kinetic energy. This is referred to as a delta-ray and will undergo additional interactions with atoms in its own, separate pathway. Since hard collisions have a lower probability of occurring, these events are more rare but still account for roughly the other half of the total energy transferred from the primary particle to the absorber.

b << a (Coulomb-force interactions with the external nuclear field); in cases when the impact parameter b is smaller than the atomic radius a, the interactions can be said to be mainly with the nucleus. Such interactions are mostly relevant for electrons, and in most cases, the electrons are scattered elastically *without* exciting the nucleus or emitting an x-ray photon (Attix, 1986). However, in a few cases, the scattering is inelastic, and results in a great energy loss by the charged particle, with a subsequent emission of an x-ray photon. This process is called bremsstrahlung collision (Podgorsak, 2010).

In the case of heavy charged particles such as protons, an inelastic collision with the nucleus may occur in addition to the previously mentioned Coulomb-interactions. If b << a, and the energy of the incoming particle is high enough (approximately 100 MeV), individual nucleons (protons, neutrons) may be driven out of the nucleus. The nucleus is then left highly excited and will decay by emission of light nucleons and γ-rays that carry the kinetic energy they have gained away from the point of interaction (Attix, 1986).

Stopping power:

To parameterize the rate of energy loss by the charged particle as it penetrates through the absorber, we define **stopping power**. The expectation value of stopping power is given as $S = \left(\frac{dT}{dx}\right)_{Y,T,Z}$ where T is the kinetic energy of the charged particle, x is the unit path length, Y is the type of charged particle and Z is the atomic number of the medium at interest (Attix, 1986). The unit is typically given as MeV/cm or J/m. A common usage of the stopping power formula is to divide it by the density, ρ, of the absorber, and thereby obtaining the **mass stopping power**, $\frac{S}{\rho} = \frac{dT}{\rho dx}$, with units in MeV·cm^2/g.

The energy lost through charged particle interactions with orbital electrons (soft and hard collisions) is defined as the *collision stopping power,* S_c, whereas the energy lost as a result of nuclear interactions between the incoming particle and the atoms of the absorber is defined as the *radiative stopping power,* S_r, and mainly includes bremsstrahlung and delta rays. This radiative stopping power component is only relevant for light particles such as electrons and positrons in calculations (Podgorsak, 2010). The final formula for the stopping power then becomes;

$$S_{tot} = S_{col}^{hard} + S_{col}^{soft} + S_{rad}$$

The stopping power for heavy charged particles can be obtained by using the relativistic *Bethe-Bloch formula*:

$$-\frac{dT}{dx} = \frac{4\pi e^2(ze)^2}{mv^2} nZ \left[ln\frac{2mv^2}{I} - ln(1-\beta^2) - \beta^2 \right]$$

where;

v is the velocity of the incoming particle

ze is the charge of the incoming particle

m is the mass of the electron

n is the number of atoms pr. cm^3

Z is the effective atomic number

I is the mean ionization potential and depends on Z; $I = 13.5 \cdot Z\ (eV)$

β is the speed of the particle relative to the speed of light

From the formula it can be seen that the rate of energy loss by the charged particle increases in materials with a high density of electrons (nZ). Furthermore, the rate of energy loss shows an inverse dependence on the speed (or energy) of the incoming particle. As the particle loses energy and the speed decreases, the rate of energy loss increases.

Protons:

Protons belong in the category of heavy charged particles and comprise the nuclei of Hydrogen-1 atoms (1_1H), consisting of a proton and an electron. Such particles lose energy through Coulomb-interactions with orbital electrons in the absorber material. In contrast to photons, protons show a drastic increase in energy loss per unit distance traversed, and this occurs close to the maximum depth penetrated by the beam. The result is a high dose deposition at this depth, with a following abrupt fall-off beyond this point. This is in line with the Bethe-Bloch formula. The peak of the high dose deposition is referred to as the *Bragg peak*, and is a distinct characterization of the dose delivery of charged particles. The depth of the Bragg peak is dependent on the mass and energy of a given charged particle beam.

2.1.3 Ionizing radiation production/devices

X-rays and gamma rays are the types of electromagnetic radiation used clinically today. They are identical in nature and properties but differ in the way they are produced. X-rays are produced extranuclearly (i.e. x-ray tubes or accelerators), whereas γ-rays are produced intranuclearly (i.e. radioactive isotopes) (Hall, 2012). Particle accelerators are used clinically and in research to accelerate charged particles to high speeds and energies.

Relevant for this thesis is the x-ray tube generating x-rays and the cyclotron producing Hydrogen nuclei (protons).

X-ray tube

The following text is based upon "The AAPM/RSNA Physics Tutorial for Residents" (Zink, 1997).

X-rays are generated by accelerating electrons from the cathode towards the anode via a potential difference. This potential difference is produced by a generator and dictates the maximum energy of the x-rays produced. The generator also produces a current in the filament – usually tungsten – at the cathode and the applied voltage determines the number of electrons emitted at the filament. As a result of the generated current, the filament is heated through thermionic emission, and electrons are released. As the electrons experience the high voltage potential difference, they are accelerated towards the anode target and photons are generated. The anode target must be of a high Z-material, to maximize the output of bremsstrahlung. Tungsten is normally used due to its high atomic number and high melting point. It is important that the electrons travel through vacuum, and the tube envelope is therefore evacuated. A schematic of the main components comprising the x-ray tube is shown in Figure 6.

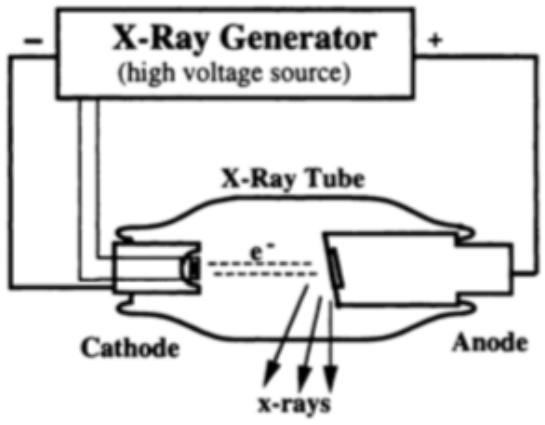

Figure 6 A simplified schematic of the main components comprising an x-ray tube (Zink, 1997)

The process of generating x-rays in such an x-ray tube is highly inefficient. Only about 1

% of the electric energy is converted to photons, the remaining is released as heat. This heat must be carried away, and the layer between the tube envelope and the housing therefore contains oil to ensure tube cooling and electric insulation.

Finally, the photons generated exits the tube through the restricting exit port. Normally, filtering is applied to remove the low energy photons. The energy spectra obtained consists of two types of radiation; *bremsstrahlung* and *characteristic x-rays*.

Bremsstrahlung

The x-rays produced from the slowing down of the electrons is referred to as bremsstrahlung. As an electron passes close to the nucleus of a target atom, they experience a deceleration due to the positive charge of the nucleus. As the electron is decelerated it releases energy in the form of an x-ray. The amount of energy the electron releases depends of how close to the nucleus it passes. The resulting energy spectrum is therefore a continuous one, with a maximum energy corresponding to the potential difference applied.

Characteristic x-rays

In addition to the x-rays generated by bremsstrahlung, characteristic lines will appear in the energy spectrum (Figure 7). This is a result of the accelerated electrons knocking out inner shell electrons of the atoms. In order for this to occur, the accelerated electrons must have an energy higher than the binding energy of these atomic electrons. The resulting process is that electrons from outer shells falls down to fill the vacancy left by the released electrons, liberating energy corresponding to the difference in binding energy between the outer and inner shells.

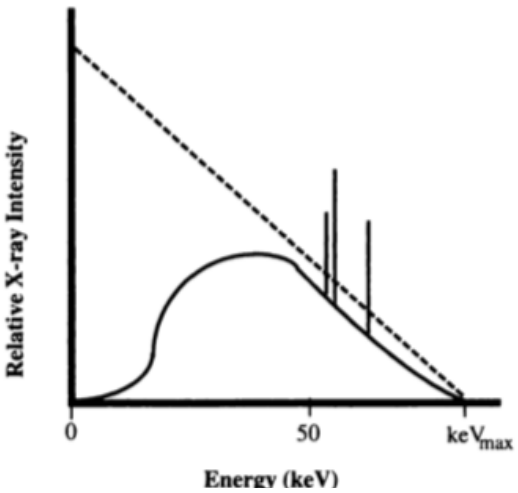

Figure 7 The emission spectrum of a tungsten target. The dotted line simulates the unfiltered bremsstrahlung portion of the spectrum. The use of a filter to remove low energy bremsstrahlung will result in a spectrum represented by the solid line. The spikes show the characteristic x-rays (Zink, 1997)

Cyclotron

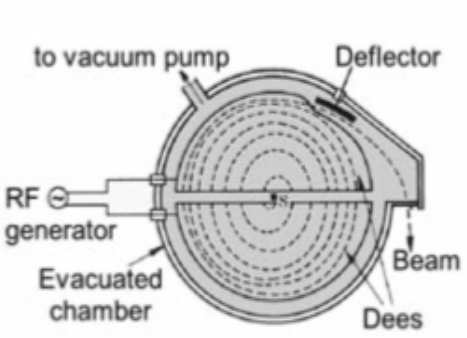

Figure 8 The cyclotron; a cross-sectional view showing the evacuated chamber with the ion pump feeding the chamber with the particles to be accelerated. The RF generator accelerates the particles as they cross the gap between the Dees (Podgorsak 2010)

The cyclotron is used to accelerate charged particles and was developed by Ernest O. Lawrence in 1930. Lawrence later received a Nobel Prize for his invention and development of the cyclotron (Podgorsak, 2010).

An ion source injects the charged particle into the two, hollow D-shaped electrodes, referred to as Dees. A magnetic circuit and coils ensure the circular motion of the charged particle, by imposing a magnetic field perpendicular to the trajectory of the particle. The acceleration is achieved by applying a high alternating voltage to the electrodes, such that when the charged particle is in the area between the two electrodes, it experiences an accelerating force. The subsequent motion of the charged particle is a circular one, with increasing radius as it is re-accelerated over and over again (Figure 8). Similar to the x-ray tube, the system of the cyclotron must be evacuated. Also, extensive cooling is required to dissipate the heat produced.

By equating the Lorentz force, F_L, exerted on the particle by the magnet field, B, and the centrifugal force we get;

$$F_L = qvB = \frac{mv^2}{r}, \quad \text{or} \quad qBr = mv$$

Where q is the charge of the particle, m is the mass, v is the velocity of the particle and r is the radius of the path during one revolution. As m, q and B are constant, we see that the particle velocity increases with increasing radius.

The output energy of the particles is reached at the periphery of the Dees (r=R) and becomes:

$$E = \frac{1}{2}mv^2 = \frac{q^2B^2R^2}{2m}$$

For a given type of particle this means that the final energy of the particles is limited by the strength of the magnetic field and the radius of the Dees.

The angular frequency, ω, becomes:

$$\omega = \frac{v}{r} = \frac{qB}{m} = \omega_{cyclotron}$$

and is only dependent on the charge and mass of the particle and the magnetic field. When the alternating voltage is applied at this constant frequency, the particle will continue to receive an accelerating boost at each gap passage (provided the particle is not relativistic).

2.2 Cell Biology

The following chapter (2.2) is based upon "Molecular Biology of the Cell" (Alberts, 2015).

2.2.1 The cell

All living organisms are made up of cells. Many of these organisms are made up of a single cell. Others consist of a vast number of cells, each having their own function and purpose, resulting in extraordinarily complex machineries such as the human species. The prokaryotic cell, found in bacteria and archaea, is simple in appearance and has no cell nucleus containing its DNA. The eukaryotic cell, on the other hand, is a complex structure and contains membrane-bound organelles that prokaryotic cells lack.

Figure 9 shows the main features of a eukaryotic cell, which is the type of cell plants, fungi and animals are made up of.

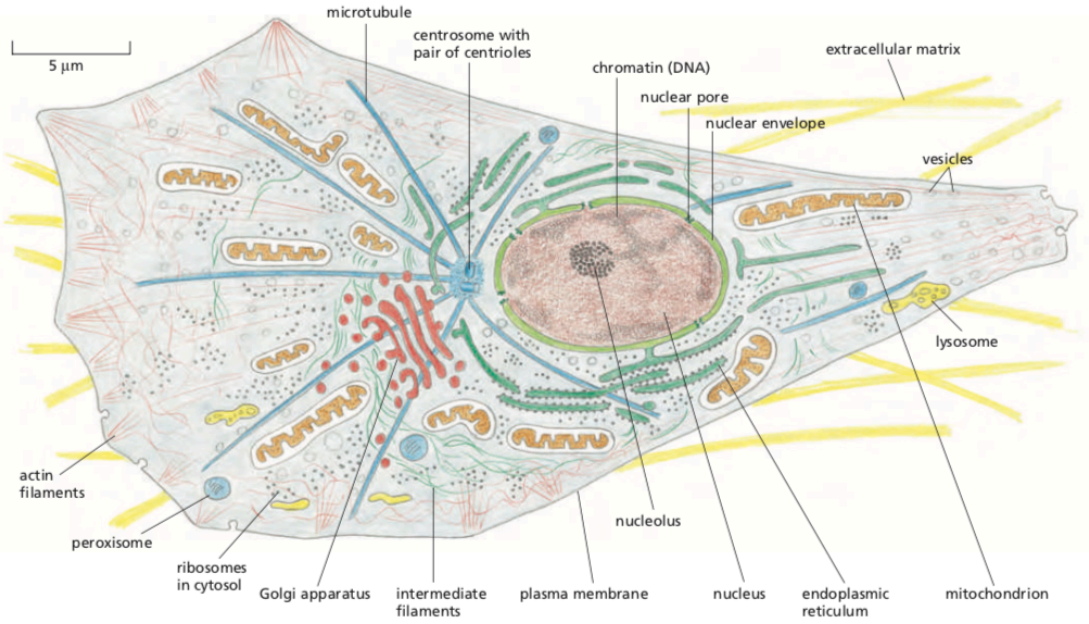

Figure 9 The eukaryotic cell and its main constituents (Alberts, 2015)

In the eukaryotic cell, the hereditary information called DNA is located inside the cell nucleus. The nuclear envelope separates the cytoplasm with all its constituents from the DNA in the cell nucleus.

Despite the 10^{13} cells that make up the human body, everything originated from a single cell and can be attributed to the cell's capability to divide and pass on a perfect copy of its hereditary information.

2.2.2 The phases of the cell-cycle

The cell cycle is the process in which a cell duplicates its DNA and divides into two identical daughter cells. To start this process, the cell receives a signal to grow and divide given that the conditions of the extracellular environment are favorable. The process is carefully regulated by control mechanisms such as checkpoints, to ensure the completion and correct end result.

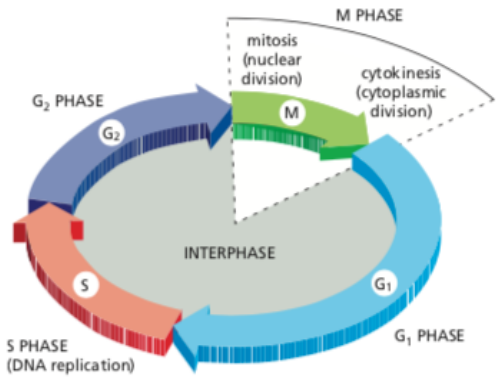

Figure 10 The phases of the cell cycle and their designated checkpoints (Alberts, 2015)

The cell cycle can be divided into two main phases; interphase and M phase (mitosis). During interphase, the cell grows and doubles its content. This is the most time-consuming event of the cell cycle, and to allow enough time for this growth to take place, interphase consists of gap phases. One gap phase called G1, is located between M- and S-phase (S for synthesis), and a second gap phase, G2, between S-phase and M-phase. These gap phases also serve as important checkpoint-stations (Figure 10). In mammalian cells, the S-phase typically lasts for 10-12 hours, whereas M-phase only lasts for about 1 hour.

If a cell has received a signal to grow and divide, but the extracellular conditions are unfavorable, the cell can enter a resting phase known as G0, where it can remain for extended periods of time, even permanently, if for instance conditions remain unfavorable. Cells can also remain in G0 if the cell has differentiated or simply if there is no need for the cell to divide, i.e. no mitogens and growth factors are present. In fact, the importance that cells enter the resting phase when the signals to undergo cell cycle are absent is one of the most powerful mechanisms in preventing uncontrolled proliferation. However, once the cell is sent through the restriction point at the end of G1, it is committed to DNA replication.

As mentioned, chromosome duplication occurs during S-phase. During M-phase, the segregation of chromosomes and division of the cell take place. M-phase is further divided into prophase (the sister chromatids condense and the mitotic spindle assembles between the centrosomes), prometaphase (nuclear envelope breaks down, chromosomes attach to microtubule), metaphase (chromosomes lie at equator between spindle poles), anaphase (sister chromatids move towards spindle poles forming daughter chromatids) and telophase (a new, nuclear envelope arises around each daughter chromatid), and cytokinesis (cells complete division), see Figure 11.

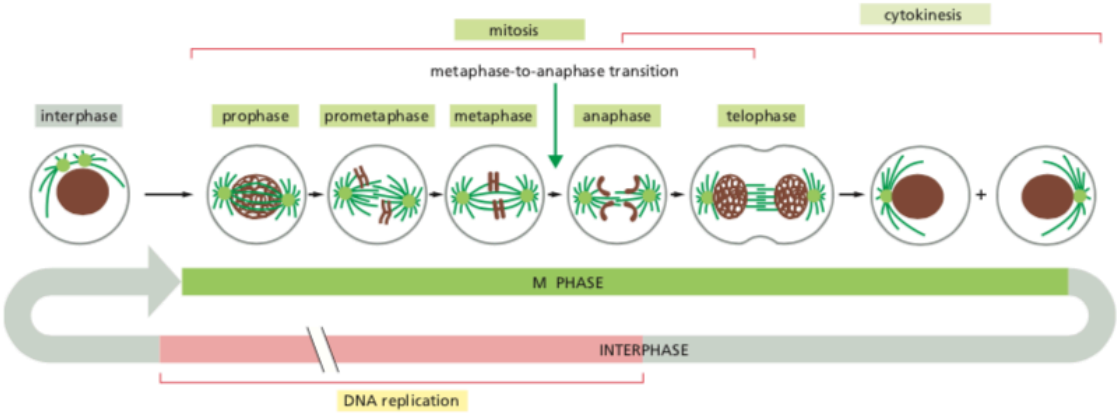

Figure 11 The events of M-phase; prophase, prometaphase, metaphase, anaphase, telophase and cytokinesis constitute the M-phase where the segregation of chromosomes and cell division occurs (Alberts, 2015)

2.2.3 DNA replication

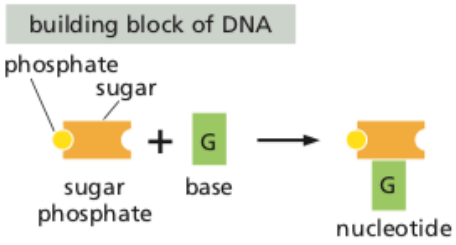

Figure 12 Nucleotide formed out of guanine (Alberts 2015)

When the cell receives a signal to start the cell cycle, the most basic function of this process is to duplicate the DNA found in the chromosomes and divide into two genetically identical daughter cells.

Our DNA is made up of subunits, nucleotides (Figure 12), each composed of a sugar-phosphate molecule covalently bounded to each other, that make up the backbone of the DNA strand, and a nitrogen-containing part known as a base attached to it. There are four types of bases, adenine (A), guanine (G) which constitute the purine bases, and cytosine (C) and thymine (T) known as the pyrimidine bases, forming four different nucleotides (see figure 10), and these nucleotides connected together form the DNA strand. The pairing can only be A-T and G-C, which is fundamental for the replication method to work.

The human DNA is made up of two such strands, shaped as a double-helix located in the cell nucleus. When the cell receives a signal to divide, it is crucial that the genome is replicated correctly in order to produce two identical daughter cells.

The DNA replication process is carefully regulated with a complex armory of components working together – known as the replication machinery. *DNA polymerase* is an important enzyme catalyzing the DNA synthesis by adding nucleotides to the template strands. Since

adenine (A) can only attach to thymidine (T) and guanine (G) can only pair with cytosine (C), the template strand is sufficient to dictate the correct sequence of the newly synthesized strand.

The replication process starts at specific locations known as *origins of replication*, recognized by *DNA polymerase*. The *DNA helicase* cleaves the double-helix, by breaking the hydrogen bonds between bases of opposite strands. Since the replication machinery can only synthesize in the 5'-to-3' direction, the consequence is that we get a *leading strand* and a *lagging strand*. The replication machinery continuously synthesizes the complementary DNA strand as it moves along the leading strand. The lagging strand, however, requires *DNA primase* to add RNA primers to be placed along the strand with gaps in between, so that the replication machinery can synthesize DNA in the 5'-to-3' direction between these primers – a process known as backstitching. The newly synthesized DNA is called Okazaki-fragments, and an enzyme known as *DNA ligase* joins the ends of the newly synthesized DNA fragments together (Figure 13).

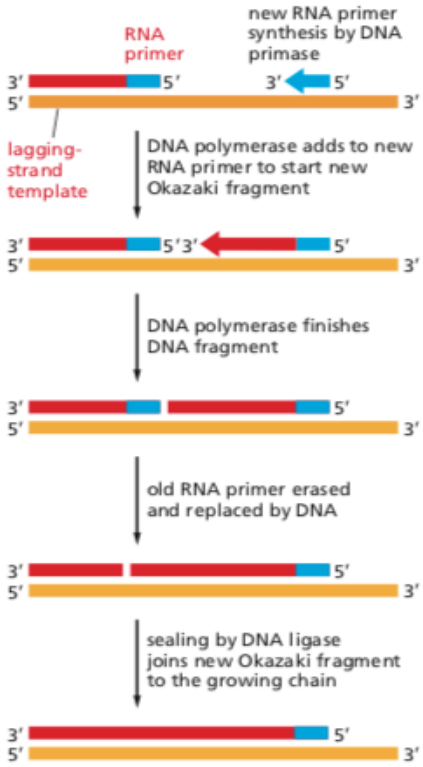

Figure 13 DNA replication, lagging strand; DNA primase adds RNA primers along the strand with gaps in between. The replication machinery can then synthesize DNA in the 5'-to-3' direction. DNA ligase joins the end of the newly synthesized fragments together (Alberts, 2015)

2.2.4 Cell cycle regulation and the control system

After a cell has committed to progress through the cell cycle, one of the functions of the control system, is to allow for enough time for the completion of each event of the cell cycle. This is facilitated by the fact that the control system is able to receive feedback from the processes it controls, and act thereby. As an example, if for some reason, the completion of DNA synthesis is not done successfully, the control system receives signals to delay progression to M phase. As a result of this, valuable time can be provided to ensure the repair of damage that otherwise could lead to disastrous outcomes for the cell such as mutations or cell death.

The three main transition points of the control system in most eukaryotic cells are located at the restriction point in late G1, where the cell commits to cell cycle entry, at the G2/M-

transition controlling the entry of the cell into mitosis and the early mitotic events, and lastly, at the metaphase-to-anaphase transition leading to the completion of mitosis and cytokinesis. Thus, the control system prevents further progression through any of these transition sites if conditions are unfavorable both inside or outside the cell.

Important components of the control system are a type of protein kinases called *cyclin-dependent kinases (Cdks)*. These kinases' main activity is to phosphorylate proteins that control the events of the cell cycle. As the name indicates, these kinases are dependent on a protein called *cyclin* to be activated. When a complex is formed of a Cdk and a cyclin, the Cdk can be activated and can further trigger certain cell-cycle events. Without the presence of the cyclin, the Cdk is inactive. It should be noted that the level of Cdk proteins present is constant, whereas cyclins are synthesized and degenerated cyclically. As a result of this, the activity of Cdks varies throughout the cell cycle. The cyclins can further be classified by which phase of the cell cycle they act on by binding to a Cdk in eukaryotic cells;

- **G1/S-cyclins:** act in late G1 by binding to Cdks and help drive the cell into the cell-cycle through the commitment point known as *Start*. Levels fall in S-phase.

- **S-cyclins:** bind to Cdks shortly after progression through restriction point and work by stimulating chromosome duplication. They also contribute in some early mitotic events. Levels remain high until mitosis.

- **M-cyclins:** in complexes with Cdks trigger entry into mitosis. Levels reach their height in beginning of mitosis, and fall in mid-mitosis.

Additionally, most cells have **G1-cyclins** that helps govern the activities of G1/S-cyclins. The variations in cyclin-Cdk activity can be seen in Figure 14.

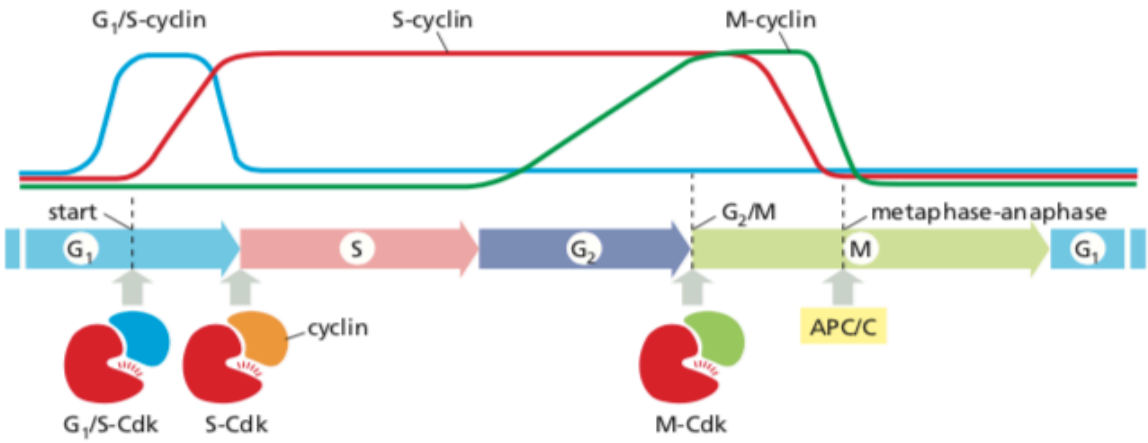

Figure 14 The cyclin-Cdk activity varies according to the phases of the cell cycle (Alberts, 2015)

As previously mentioned, the activation of Cdks happens when a cyclin binds to the Cdk. However, the complex is only partially activated in this state. Complete activation occurs when the *Cdk-activating kinase (CAK)* phosphorylates an amino acid near the active site of the Cdk (see Figure 15).

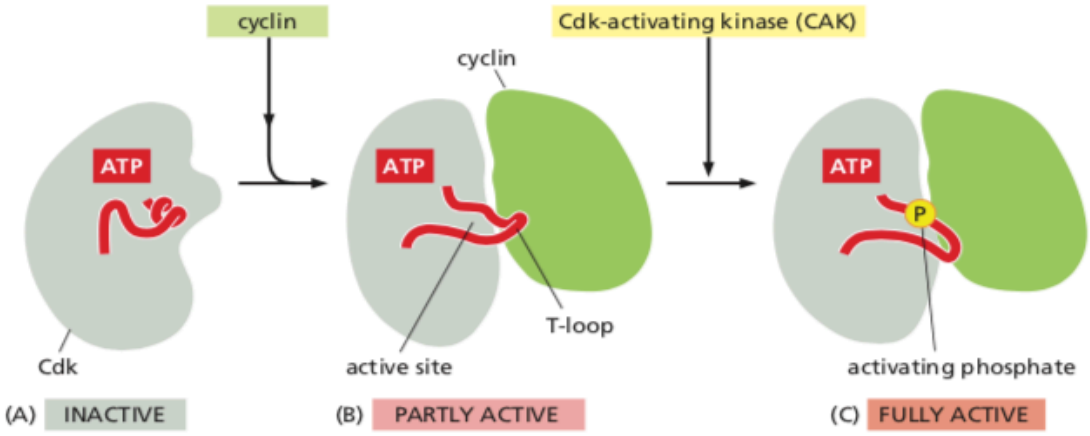

Figure 15 The steps involved in the activation of Cdks; activation starts when the cyclin and Cdk bind together. The Cdk-activating kinase (CAK) assist in complete activation by phosphorylating an amino acid near the active site of the Cdk (Alberts, 2015)

While the cyclin-Cdk complexes are essential in driving the cell through Start and the G2/M transition points, other mechanisms are at play to trigger the metaphase-to-anaphase transition. In contrast to the transitioning driven by cyclin-Cdks by phosphorylation, the

metaphase-to-anaphase transition is triggered by protein destruction. The enzyme *anaphase-promoting complex* or *cyclosome* (APC/C) drive the ubiquitylation of two proteins; securin and the S- and M-cyclins, so that the completion of the cell cycle can occur.

In sum, the control system of the cell cycle consists of several complexes with well-defined tasks to ensure the correct progression and completion of the cell cycle.

2.2.5 Cell death

In the study of how living organisms develop, the mechanisms in which cells die is equally important as knowing how they grow and divide. Cells may die to maintain tissue size, as is the case of adults who no longer need to grow larger in size. Controlled forms of cell death are also crucial in the shaping of limbs such as the fingers during embryogenesis. Additionally, cell death occurs to protect the healthy organism for example during infections. These examples of cell death are driven by a systematic and controlled sequence of events, in which the cell ensures its own destruction. The surrounding cells eat the dying cell, leaving no trace of its existence. Cells that die during this *programmed cell death*, usually undergo **apoptosis** which involves a series of morphological changes; the cell shrinks and condenses followed by the collapse of the cytoskeleton, the nuclear envelope dismantles and the chromatin rupture into fragments. The result is that neighboring cells or a macrophage are able to engulf the membrane-enclosed fragments (apoptotic bodies) avoiding any spill-out of the content of the cell. The death of a cell through apoptosis is a neat way of dying causing no inflammatory response. In contrast, acute incidents such as trauma or inadequate blood supply may lead to another form of cell death called **necrosis**. During necrosis the cell bursts, spilling its content onto nearby cells evoking an inflammatory response. The two death processes can be seen in Figure 16.

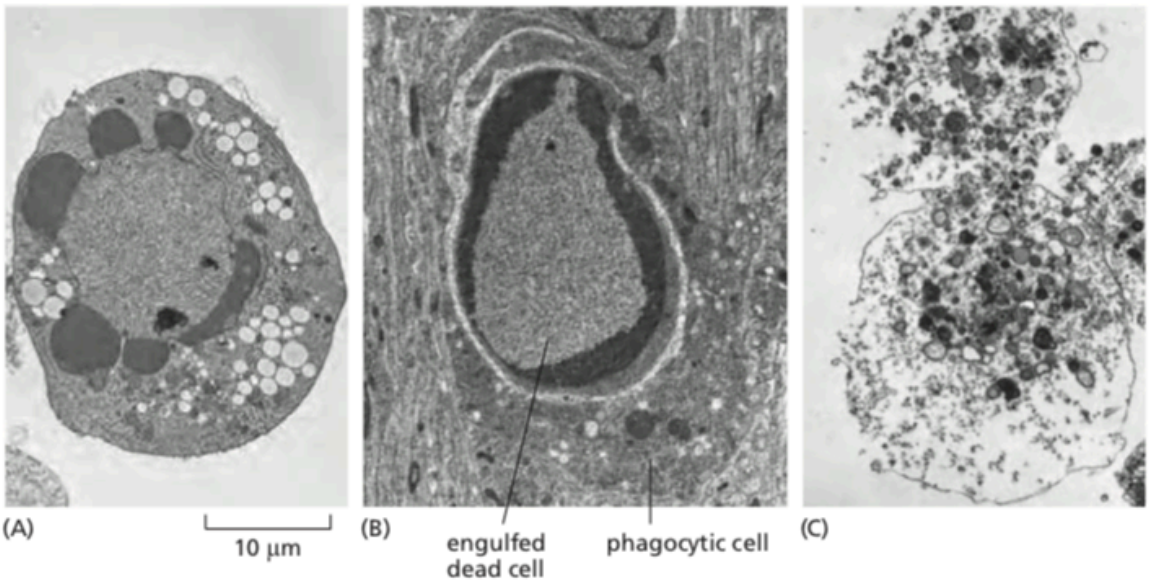

Figure 16 The two forms of cell death. (A); Apoptosis. This cell died in a culture dish. (B); Apoptosis, the cell has been engulfed by a phagocyte in developing tissue, (C); death by necrosis. The cell died in a culture dish (Alberts, 2015)

2.3 Radiobiology

2.3.1 Direct and indirect effects of radiation

The following text has been adapted from "Radiobiology for the Radiologist" (Hall, 2012).

It has been well established that the radiosensitive target of the cell is the DNA. Several experiments have supported this (Kaplan, 1964) (Harris, 1975) (Hofer, 1978), inter alia an experiment incorporating short range Auger-emitting isotopes into DNA, showing that the cell survival was drastically lower than when the isotope was bound to other components of the cell.

When ionizing radiation is absorbed in biological material the subsequent effects can be classified into *direct* or *indirect* actions. In those cases where the ionizing radiation interacts directly with the atoms of the target molecule (DNA), causing ionizations and excitations, the process is said to be direct. In contrast, indirect action involves a two-step process where the radiation first interacts with other atoms or molecules which results in free radicals that are able to diffuse a distance from where the interactions took place. Such free radicals are characterized by having an unpaired orbital electron in the outer shell, making them highly reactive and able to transfer chemical damage to the molecules with which they react. Since

our cells are composed of 80% water, water radicals are most frequently produced through such indirect actions.

Table 1 lists the two main processes in the creation of water radicals. One process involves the ionization of a water molecule by the ionizing radiation, releasing an electron from the molecule (Step 1). The resulting polarized molecule and ejected electron can then both undergo further processes (Step 2) leading to the formation of the two water radicals $H^{\cdot}$ and $OH^{\cdot}$. The other process occurs when the ionizing radiation excites the water molecule, which then releases its excess energy by separating into the two water radicals. Notice that also e^{-} can become a water radical by hydration, meaning that it is enveloped by surrounding water molecules. In this state the electron is referred to as e_{aq}^{-} and is considered relatively stable for a few milliseconds.

Table 1 Water radicals produced through the interaction between biological material and ionizing radiation

	Step 1	**Step 2**
Ionization	$H_2O + ionizing\ radiation \rightarrow \boldsymbol{H_2O^+ + e^-}$	$H_2O^+ \rightarrow \boldsymbol{H^+ + OH^{\cdot}}$ $e^- + H_2O \rightarrow \boldsymbol{OH^- + H^{\cdot}}$
Excitation	$H_2O + ionizing\ radiation \rightarrow \boldsymbol{H_2O^*}$	$H_2O^* \rightarrow \boldsymbol{H^{\cdot} + OH^{\cdot}}$

The direct effect is the dominant process of high LET radiation, whereas the indirect effect is more associated with low LET radiation.

2.3.2 Linear energy transfer (LET) and relative biological effectiveness (RBE)

The linear energy transfer (LET) is characterized by the ionization density in tissue by a given type of ionizing radiation beam. It is a measure of the rate of local linear energy *deposition* in a given medium rather than the rate of energy loss of the particle, which can be attributed to stopping power. The LET does not include the effects of radiative losses and delta rays, which is covered by the radiative component in the stopping power formula. Furthermore, LET says something about the quality of the radiation beam and can be divided into low LET radiation

and high LET radiation, where the unit is given as keV/µm (Podgorsak, 2010). Table 2 shows some radiation beams and the LET they produce.

Table 2 Types of radiation and their corresponding LET (Podgorsak, 2010)

Low LET radiation	LET (keV/μm)	High LET radiation	LET (keV/μm)
X rays: 250 kVp	2	Electrons: 1 keV	12.3
γ rays: Co − 60	0.3	Neutrons: 14 MeV	12
X rays: 3 MeV	0.3	Protons: 2 MeV	17
Electrons: 10 keV	2.3	Carbon ions: 100 MeV	160
Electrons: 1 MeV	0.25	Heavy ions:	100–2000

While LET characterizes the amount of energy transferred to the absorbing medium, *relative biological effectiveness (RBE)* can be attributed to the effects of different radiations in a medium. Specifically, it is defined as the dose ratio of two different types of radiation that gives the same biological effect;

$$RBE = \frac{dose\ of\ reference\ radiation}{dose\ of\ radiation\ under\ investigation}$$

with the reference radiation normally being a low-LET quality, e.g. 250 kV x-rays. Figure 17 shows the relationship between RBE and (mean) LET for cell survival levels of 0.8, 0.1 and 0.01. For LET-values up to about 10 keV/µm, the RBE increases slowly. Beyond this point, there is a rapid increase in RBE, with a maximum reached at 100 keV/µm, before the RBE again falls to a lower value. This optimum LET at 100 keV/µm in terms of biological damage can be attributed to the density of ionizations at this energy. At this density, the average distance between ionizations coincides with the diameter of the double-helix (2 nm). This means that for sparsely ionizing radiation such as x-rays, the probability of causing a double-strand break is low, and usually, more tracks are required to achieve this. In contrast, for more densely ionizing radiation (>100 keV/µm), energy is 'wasted' even though double-strand breaks are readily produced, since the ionizing events occur too close together in space.

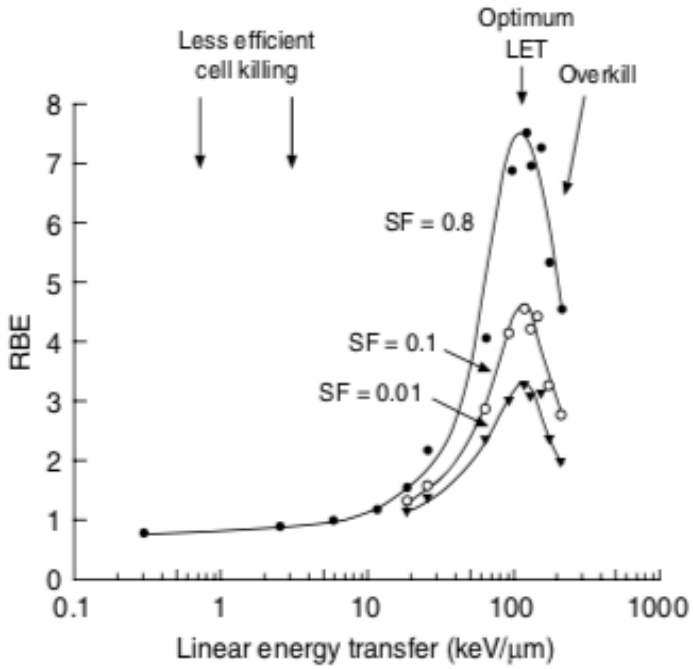

Figure 17 The relationship between RBE and LET; the three curves displayed represent different levels of cell survival. The optimal LET in terms of biological damage is seen to be at 100 keV/µm (Mayles, 2007)

2.3.3 DNA damages

It has already been mentioned that DNA is the sensitive target of our cells. Damages to DNA can be fatal for the cell or the organism if not properly dealt with. As have been noted earlier, powerful control systems within our cells exist to handle such damages. The type of damages that occur can be classified into *sublethal*, *potentially lethal* and *lethal* damages. A sublethal damage is – as the name indicates – not lethal on its own and can efficiently be repaired. However, in the event that another sublethal damage takes place close enough in space and time, the sublethal damages can together become potentially lethal. A potentially lethal damage will kill the cell *if* the cell is not able to sufficiently repair the damage in time before it becomes lethal. A damage that will inevitably kill the cell is said to be lethal.

Several damages occur spontaneously in our DNA, even under normal cell conditions, such as *oxidative damage*, *hydrolytic attack (hydrolysis)* and *methylation* (see Figure 18).

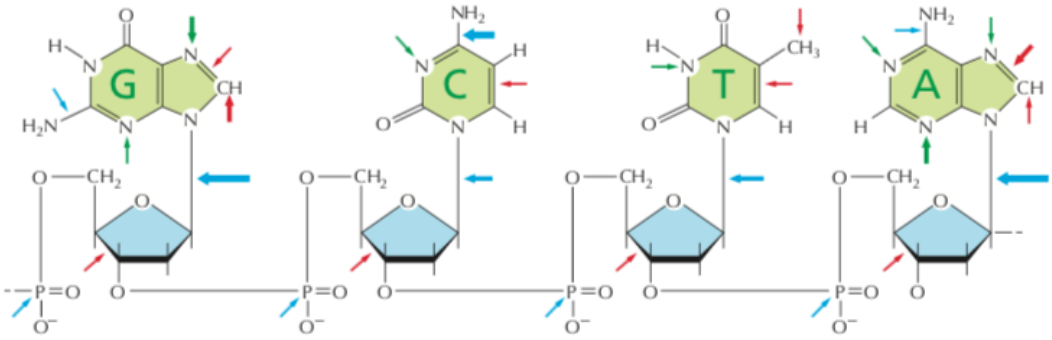

Figure 18 Spontaneous damages to DNA occur regularly. The red arrows represent oxidative damage, the blue arrows represent hydrolytic attack and the green arrows represent methylation (Alberts, 2015)

The hydrolysis can lead to *depurination*, where purine bases (adenine and guanine) are lost, and *deamination* where i.e. cytosine is converted to uracil (an RNA-base) (see Figure 19). These types of base damages are promptly repaired and are classified as sublethal damages.

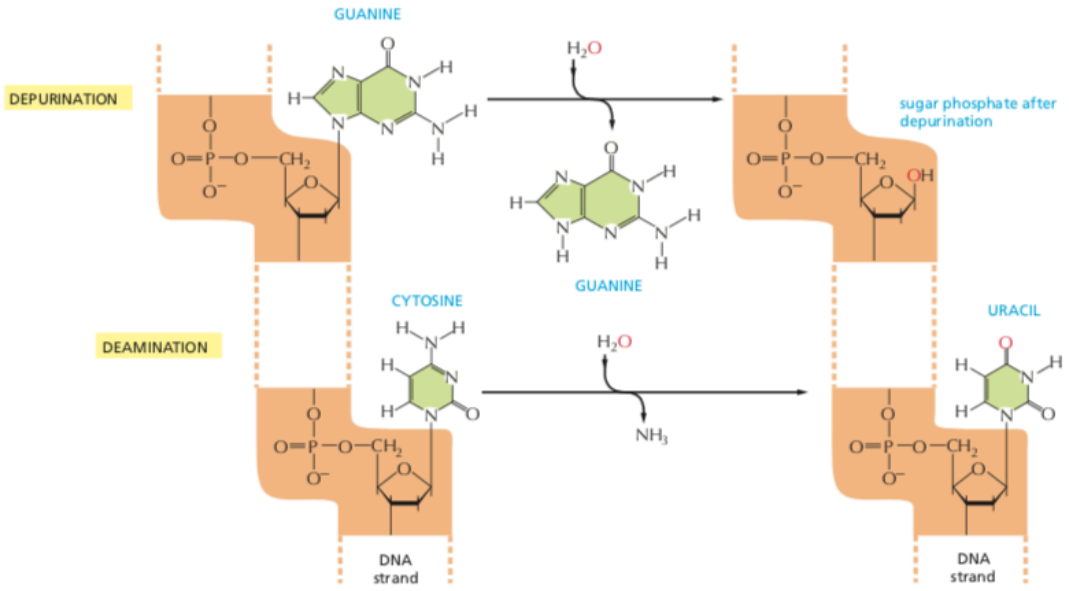

Figure 19 Damages such as depurination and deamination can follow hydrolysis. In depurination, purine bases are lost. In deamination, cytosine is converted to uracil (Alberts, 2015)

In addition, reactive metabolites and chemical exposures contribute to the variety of damages inflicted on the DNA in our cells. Also, ultra violet (UV) radiation can link adjacent pyrimidine bases covalently, forming *pyrimidine dimers*, resulting in yet another DNA damage that must be readily repaired (Figure 20).

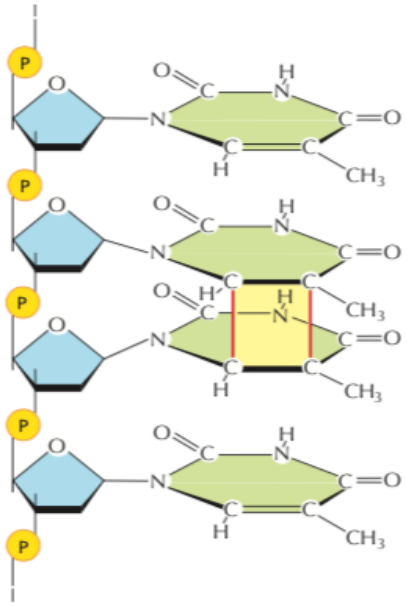

Figure 20 The figure shows a thymine dimer where adjacent pyrimidine bases have been linked covalently (Alberts, 2015)

Exposure to external radiation, oxidizing agents, replication errors and the production of other metabolites can cause DNA strand breaks. When a break occurs in the sugar-phosphate backbone of only one strand, it is referred to as a single strand-break (SSB). The damages mentioned above are examples of this. A single strand-break is considered to be of the sublethal type of damage and several mechanisms exist to repair such damages.

A double strand-break (DSB) on the other hand, either caused by one interaction or two separate interactions close in space and time, is a more severe damage. If not dealt with in time, such a damage can result in the fragmentation of chromosomes and ultimately the loss of genes during cell division. A double strand-break is therefore considered to be potentially lethal to the cell.

Erroneous DSB repair may lead to another type of fatal damage. If the cell enters S-phase with DSBs, chromosomal aberrations (CA) may be formed. If the cell goes on to enter mitosis with these chromosomal aberrations the damage has become lethal and will likely lead to

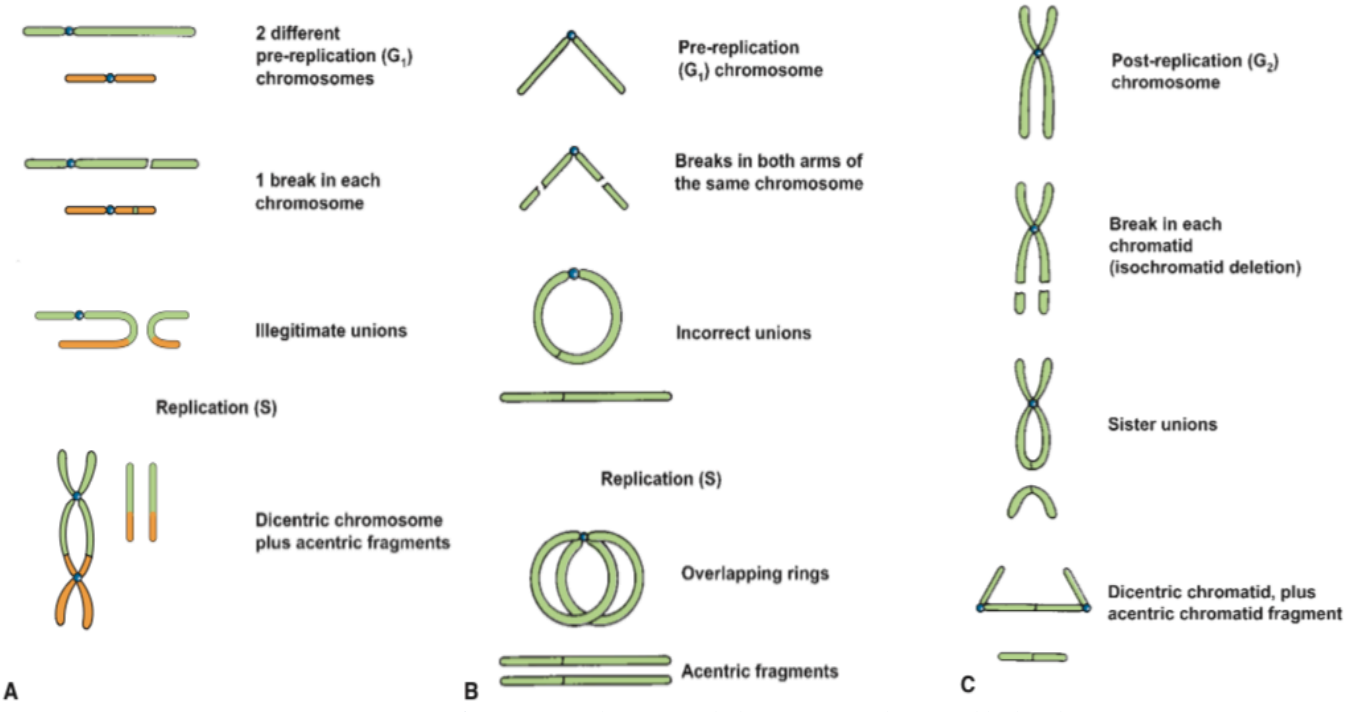

Figure 21 Various types of asymmetric chromosomal aberrations can be caused by breaks in the chromosome; A: dicentric, B: ring, C: anaphase bridge (Hall, 2012)

death of the cell. The different types of asymmetric chromosomal aberrations can be seen in Figure 21. Notice that two DSBs are required for the chromosomal aberrations illustrated.

Indeed, numerous DNA damages occur in individual cells of our body every single day, yet – in most cases – no harm is done to us as a whole. This is credited to the sophisticated repair mechanism that continuously govern the integrity of our DNA.

2.3.4 DNA repair

The repair mechanism in our cells has a tremendous task in repairing all the damages that arise in our DNA every day. Effective mechanisms exist to repair base damages, single-strand breaks (SSBs) and double-strand breaks (DSBs), which, if left unrepaired, could be fatal for our cells. Failure in the repair capacity has been identified in many human diseases, leading to an increased mutation rate and an increased risk of developing cancer.

Both type of damage and at which stage of the cell cycle these damages occur determine the exact repair processes that are initiated. All eukaryotic cells have a double-helix structure of DNA – in fact, only a few viruses have single-stranded DNA – a feature that is effectively taken advantage of by the DNA repair mechanism.

Two of the most common repair pathways associated with base damage and SSB involve removing the damage by excision and using the undamaged strand as a template. DNA polymerase adds the corresponding nucleotides and DNA ligase seals the remaining break (see Figure 22). The ***base excision repair (BER)*** involves the recognition of base damages by enzymes called *DNA glycosylases* which then remove a damaged base from its sugar. *AP endonuclease* recognizes this missing base, and cleaves the backbone leaving a gap that can be filled in and sealed. The other pathway, ***nucleotide excision repair (NER)***, starts with a multienzyme complex recognizing a distortion in the structure of the DNA double helix. A *helicase* unwinds the double helix and the *excision nuclease* cleaves the backbone on each side of the damage, about 30 nucleotides in length. The large gap is then filled in and sealed by DNA polymerase and ligase. Bulky lesions such as thymine dimers (Figure 20) are effectively repaired by the NER mechanism.

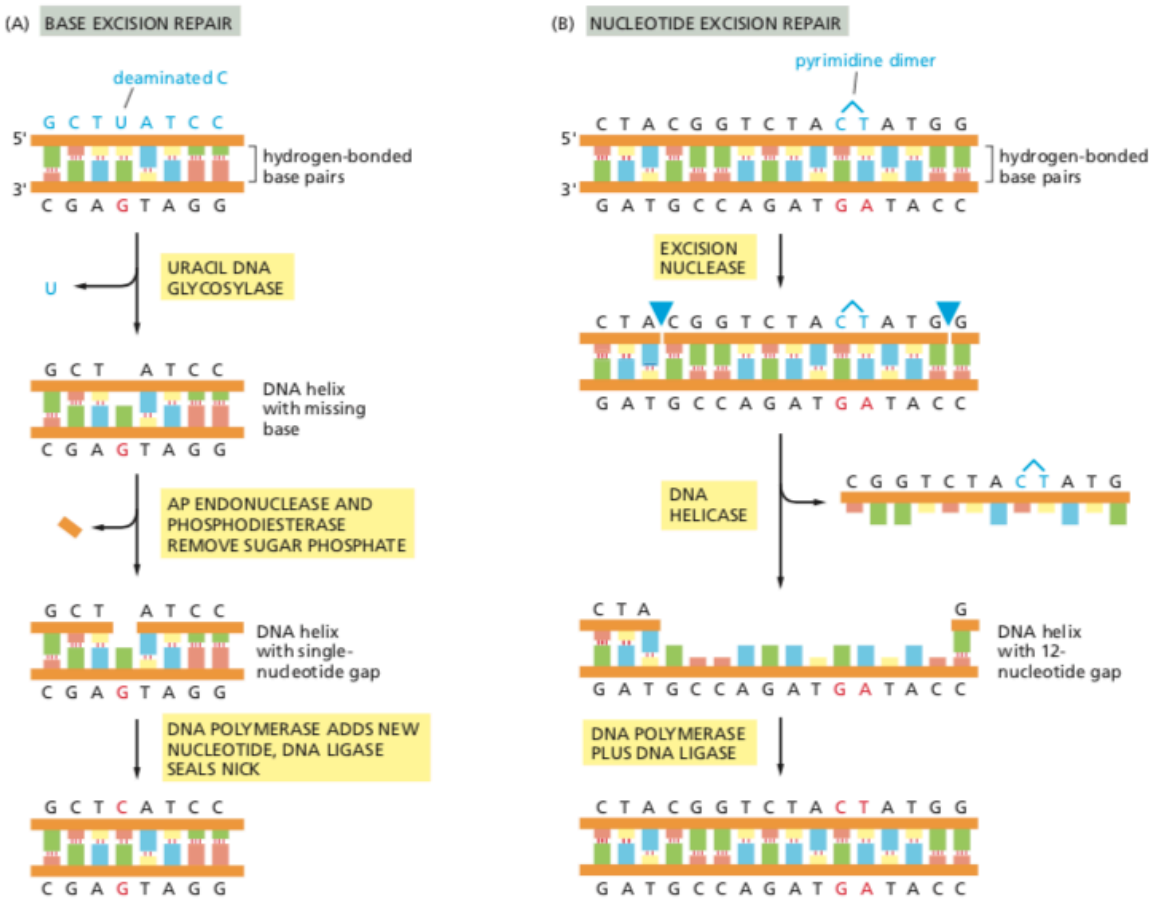

Figure 22 (A) Base excision repair; the base damage is excised and removed, and DNA polymerase adds the right nucleotide which is then sealed by DNA ligase. (B) In the nucleotide excision repair, helicase unwinds the DNA helix and the excision nucleus cleaves the area of the sugar-phosphate backbone containing the damaged site. DNA polymerase adds the right nucleotides in the gap before it is sealed by DNA ligase (Alberts, 2015)

A double-strand break, which is an especially dangerous type of damage typically induced by ionizing radiation, can lead to the loss of genes during cell division. A consequence of this could be that a *tumor suppressor gene* is lost, giving rise to dangerous mutations.

Two of the main mechanisms existing to deal with DSBs are ***nonhomologous end joining (NHEJ)*** and ***homologous recombination repair (HRR)***. NHEJ is considered the 'quick fix' in dealing with DSBs. The ends where the DSB has occurred is simply joined together again by DNA ligation, typically with the loss of a few nucleotides at the damage site. NHEJ is normally used during G1, when DNA duplication has not yet occurred.

A more sophisticated form of repair is HRR, where sister chromatids are used as a template to repair DNA. As a consequence, this form of repair can only occur after the DNA has been replicated, namely in S and G2. This repair mechanism represents the most accurate form of repair of DNA double-strand breaks, see Figure 23.

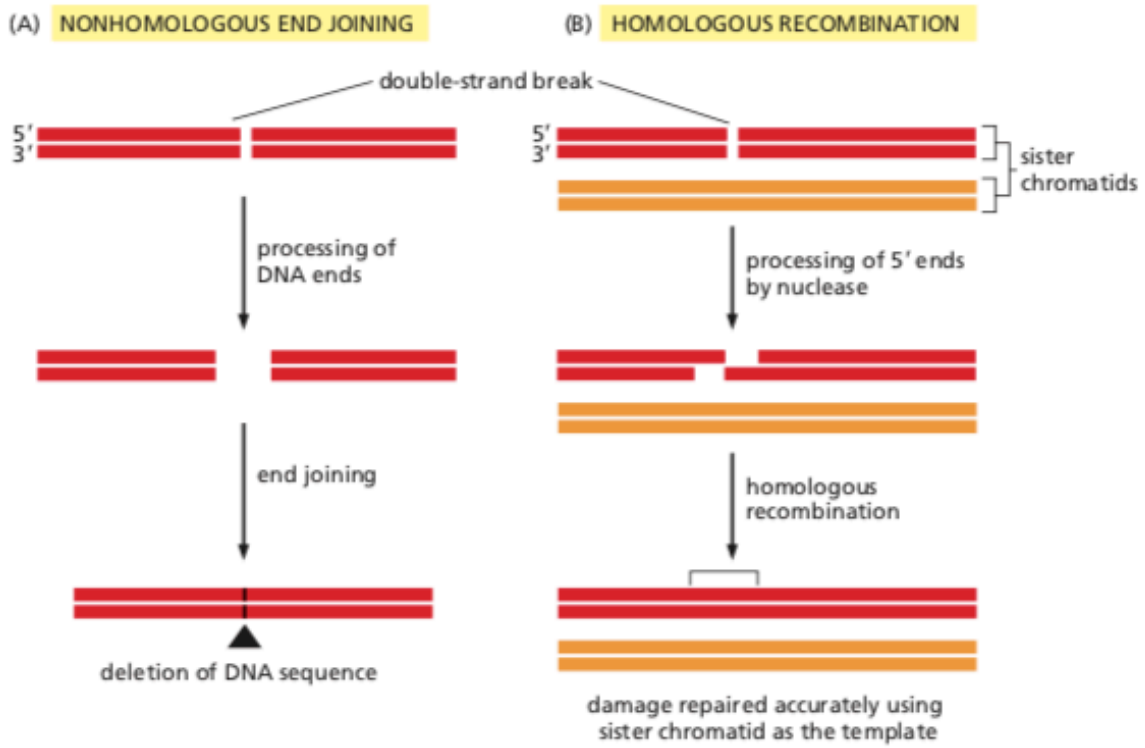

Figure 23 (A) NHEJ; the first step is the degradation of the broken nucleotides that cannot be ligated. The ends are then joined together. The Ku protein plays an important role in this repair pathway. (B) In HRR each of the strands in the DNA duplex containing the DSB uses the complementary strand of the intact DNA duplex as a template. The 3' end of the damaged strand invades the intact strand in search of homologous sequences through base pairing. DNA polymerase synthesizes DNA on the broken strand. The repaired strand can then be used as a template for the remaining broken strand (Alberts, 2015).

γH2AX: As previously mentioned, the DNA of eukaryotic cells is found in the cell nucleus. Here the DNA is organized into a structural hierarchy called chromatin. The chromatin consists of building blocks known as nucleosomes; a nucleosome is a complex of eight histone proteins with the DNA double-helix wrapped around. The histone variant H2AX is one of these fundamental components in the packaging of chromatin in eukaryotic genomes. In 1998 H2AX was found to be rapidly phosphorylated at Serine-39 in humans and mouse after being given treatments that cause double-strand breaks (Rogakou, 1998). Specifically, the generation of double-strand breaks results in the phosphorylation of H2AX on the serine oxygen in the gamma position creating discrete γH2AX foci. Burma et al. (2001) identified *ataxia telangiectasia mutated (ATM)* to be the main kinase responsible for the phosphorylation of H2AX (Burma, 2001). The functional role of γH2AX is to act as an amplifier of the damage signal and lay the foundation for mobilizing the necessary steps to complete the repair process. On the basis of these factors, γH2AX can be used as a marker for DSBs (Pinto, 2010).

2.4 Immunology

Ehrlich was one of the first to propose the idea that the immune system possessed capabilities of an anti-tumor response in 1909. However, immunology as a science field only began to gain interest in the mid 20th century, and with the work of Old & Boyse (1964) and Klein (1966), identifying the existence of "tumor-specific antigens', the idea of cancer immunosurveillance could be established. The formal hypothesis of immunosurveillance was proposed by Sir Macfarlane Burnet, which incorporated work done by Lewis Thomas;

"*In large, long-lived animals, like most of the warm-blooded vertebrates, inheritable genetic changes must be common in somatic cells and a pro- portion of these changes will represent a step toward malignancy. It is an evolutionary necessity that there should be some mechanism for eliminating or inactivating such potentially dangerous mutant cells and it is postulated that this mechanism is of immunological character*" (Burnet, 1970).

In response, research followed aiming to challenge the immunosurveillance hypothesis, by investigating whether an increase in chemically induced or spontaneous tumors could be demonstrated in hosts of defect immune systems. However, the lack of understanding at the time of mouse models of immunodeficiency, led to the use of fallible animal models and the research was largely inconclusive, resulting in the abandonment of the immunosurveillance hypothesis by 1978.

Only about three decades later, with the use of genetically defined mouse models of complete immunodeficiency and the increased knowledge of the molecular mechanisms of tumor antigens, the topic again gained attention. Dunn et al. proposed a new definition they termed "cancer immunoediting" where they incorporated both the host-protecting and the tumor-sculpting contributions of the immune system on tumor development. These mechanisms could be both tumor suppressing as well as tumor tolerating (Dunn, 2002).

Although most neoplastic lesions will be effectively rejected by the host immune system, some of the more aggressive neoplastic lesions exhibiting a high mutational diversity may suppress the anti-cancer immunosurveillance and defence mechanisms against uncontrolled proliferation. In that case, the host immune system can perform immunoediting ultimately leading to cancer development resisting antitumor immunity. Such cancerous cells exhibit low immunogenicity (Dunn, 2002).

2.4.1 Immunogenic cell death

Up until the concept of danger theory was introduced by Matzinger in 1994, the field of immunology was dominated by the self-non-self theory developed by Burnet in the 1940s. The self-non-self theory was based on the idea that only foreign elements (non-self) will infer an immune reaction in the body, endogenous elements (self) on the other hand, will not. Matzinger abandoned this belief and suggested instead that "*the immune system is far more concerned with danger and potential destruction than with the distinction between self and non-self*" (Matzinger, 1994). Her motivation for this shift in perspective was due to her dissatisfaction with how the former theory failed to explain certain phenomena. Though the usefulness of the danger theory has been criticized (Pradeu, 2012), the last decade of research has showed that the immunogenicity of dying cancer cells can be elevated by the emission of danger signals – so-called damage associated molecular patterns (DAMPs). By encouraging a cancer cell death sequence, with the activation of danger signaling pathways leading to the pre-mortem emission of DAMPs, the immunogenicity of dying cancer cells can be increased. Such a pathway is called *immunogenic cell death, ICD* (Garg, 2015).

ICD is induced by the emission of DAMPs through oxidative-endoplasmic reticulum (ER) stress, autophagy and necrotic plasma membrane permeabilization (Kepp, 2014).

The emission of DAMPs as a direct effect of ICD can be divided into three categories; *surface exposed chaperones*, *secreted nucleotides or nucleic acids* and *release of endogenous toll-like receptor (TLR) agonists* (Garg, 2015). *Calreticulin (CRT)* is one of the main chaperones associated with immunogenic cell death. A danger signal crucial for ICD is the secretion of the nucleotide *adenosine triphosphate (ATP)* from dying cancer cells (Garg, 2015) which leads to the activation of the $P2RX_7$-receptor on dendritic cells (DCs), which further activates the inflammasome NLRP3. The activation of NLRP3 mediates caspase-1 resulting in secretion of IL-1β which is an important anti-tumor immunity cytokine (Showalter, 2017). Another DAMP associated with ICD is the toll-like receptor (TLR) agonist *high mobility group-box 1 (HMGB1).* Although normally found in the nucleus, HMGB1 is released post-mortem by cancer cells exposed to stress or as they are dying, leading to TLR signaling and immunity protection (Showalter, 2017).

2.4.2 Calreticulin

Calreticulin was first discovered by Oswald and MacLennan in 1974, when they studied proteins that bind to calcium (Ca^{2+}) in the sarcoplasmic reticulum. Out of the seven proteins isolated only one showed a high affinity to calcium and they named this protein "high affinity calcium binding protein" (HABP) (Ostwald, 1974). The name 'calreticulin' was only given 15 years later (Smith, 1989) and is now the consensus in literature.

Calreticulin is a chaperone protein, primarily located in the lumen of the endoplasmic reticulum (ER) of normal cells. It is composed of three domains; the N-domain, the P-domain and the C-domain (Figure 24). The globular N-terminal region is composed of eight anti-parallel β-strands and can act as a binding site of α-integrins and steroid receptors. The presence of cysteine residues forming disulphide bonds in the N-region facilitates the interaction with the P-domain, which can then catalyze important chaperone functions. The P-domain consists of the lectin-like chaperone structures that form the basis for the protein-folding capabilities of calreticulin. These chaperone structures contain two sets of three repetitive amino acid sequences. Furthermore, the P-region is characterized by high-affinity, low-capacity to Ca^{2+}. The C-domain, on the other hand, has a low-affinity, high-capacity to Ca^{2+}, thanks to the acidic environment facilitating Ca^{2+}-buffering functions. Additionally, the C-domain contains a KDEL sequence which functions as an ER-retrieval signal, emphasizing the enriched location of calreticulin in the lumen of the ER (Lu, 2015).

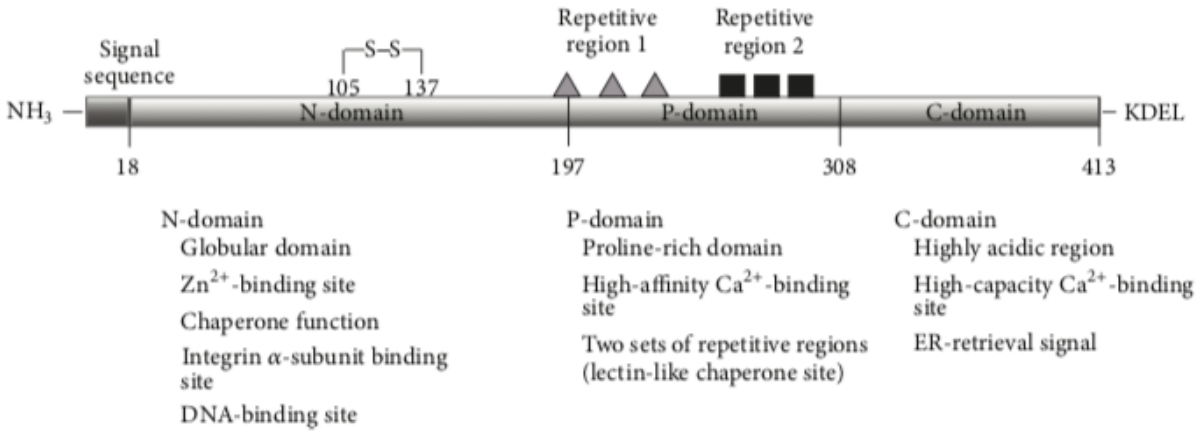

Figure 24 The three domains of calreticulin (Lu, 2015)

The main functions of calreticulin are to act as a chaperone in the ER, i.e. help in the folding of proteins, and to regulate Ca^{2+} homeostasis. Under normal conditions, Ca^{2+} is found in the lumen of the ER and is an important molecule in developmental and cellular processes.

Calreticulin is one of the primary associates of Ca^{2+} due to the Ca^{2+}-binding sites in the P- and C-domain. As a consequence, higher levels of calreticulin can lead to an increase in the intracellular storage levels of Ca^{2+} (Lu, 2015).

Other important functions of CRT besides being a protein chaperone and maintaining Ca^{2+} homeostasis include cell migration and function, RNA stability, phagocytic signal and cell proliferation (Di Martino, 2017), see Table 3.

Table 3 Functional roles of calreticulin. Adapted from (Di Martino, 2017) and (Lu, 2015).

Function	Action
Protein chaperone	Calreticulin helps with the correct folding of proteins
Calcium homeostasis	Calreticulin is a Ca^{2+} regulator due to its two binding sites
Cell migration and adhesion	Calreticulin is crucial in regulating cell migration and adhesion
RNA stability	Calreticulin regulates mRNA stability by being a trans-acting factor
Phagocytic signal	Calreticulin works as a signal to induce phagocytic uptake in dying cancer cells
Cell proliferation	Calreticulin has been found to upregulate or downregulate cell proliferation depending on cell type

Calreticulin on the cell membrane plays an important role in the destruction of cancer cells via the activation of the immune system. Several types of cancer have shown a higher expression of calreticulin on the cell surface than normal cells including acute myeloid and lymphoblastic leukemias, non-Hodgkin lymphoma, bladder cancer, glioblastoma and ovarian cancer (Chao, 2014).

2.5 Dosimetry

2.5.1 Ionization chamber

Sections 2.5.1 and 2.5.2 are based upon "Handbook of Radiotherapy Physics, Theory and Practice" (Mayles, 2007) and "Introduction to radiological physics and radiation dosimetry" (Attix, 1986).

Absolute and relative dose measurements can be performed by the use of ionization chambers. The ionization chamber contains a gas, usually air, as the sensitive medium and two electrodes between which a voltage is applied. As the beam ionizes the gas, a current is measured by the electrometer, which can then be related to dose.

Any ionization chamber to be used in the clinic needs to be calibrated by a certified calibration laboratory such as the Primary Standard Dosimetry Laboratories (PSDLs). In Norway, one such PSDL is the Norwegian Radiation Protection Authority (NRPA). These institutions use a free-air ionization chamber to determine the calibration factor air kerma, K_{air}. The free-air ionization chamber is designed so that the walls of the chamber have no impact on the response. The idea is to achieve charged particle equilibrium, placing requirements on the dimensions of the chamber to achieve this.

The ionization chambers used in the clinic is normally cavity chambers. These can be cylindrical or plane-parallel. Both chambers act as Bragg-Gray cavities; the walls are assumed thin enough to not perturb the charged-particle field and the absorbed dose is entirely due to the charged particles crossing it (Attix, 1986).

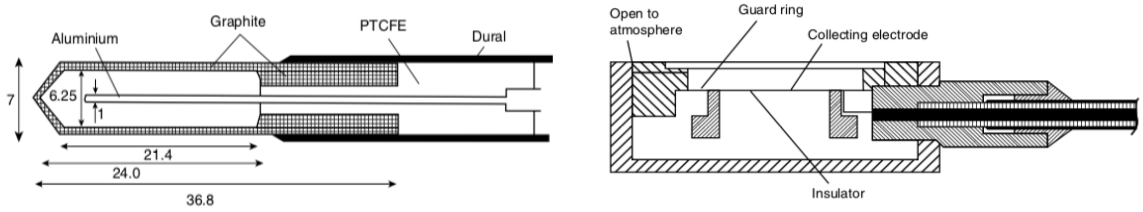

Figure 25 Left: The cylindrical Farmer chamber. Right: The NACP plane-parallel chamber (Mayles, 2007)

The Farmer chamber, a common type of cylindrical ionization chamber can be seen to the left in Figure 25. The outer cylindrical layer made of graphite makes up one of the electrodes. The other electrode is an aluminium rod placed in the center of the chamber. During irradiation, the central axis of the cylindrical chamber is placed perpendicular to the beam direction.

The plane-parallel chamber on the other hand, is irradiated with the central axis parallel to the direction of the beam (see right panel of Figure 25). The collecting electrode is a thin layer made of graphited rexolite.

However, it is important to note that the dose to air measured by the ionization chambers does not represent the dose to tissue (water) that is relevant to quantify for clinical purposes. Additional calculations such as cavity theory can be employed to relate the dose to air, D_{air}, to the dose to medium, D_{med};

$$D_{med} = D_{air}\, S_{med,air}\, p_{wall}\, p_{cav}\, p_{cel}$$

where $S_{med,air}$ is the ratio of the stopping power in water to that in air, p_{wall} is a perturbation factor correcting for the effect of the wall, p_{cav} is a perturbation factor that applies only for electron beams and corrects for the effect that more electrons are scattered into than out of the cavity, and p_{cel} includes the effect of the central electrode material differing from the material of the medium.

2.5.2 Transmission monitor chamber

A transmission monitor chamber can be used in situations where the radiation generator fluctuates. Whenever the radiation output is not constant in time, some kind of monitoring is needed to relate the measurements to the actual dose received. The dose rate and the beam position can be monitored throughout the irradiation. This requires a relatively large diameter

compared to the ionization chamber. Additionally, the electrodes must be thin to reduce perturbation of the beam. It is essential that the irradiation duration is the identical for the transmission monitor chamber and the ionization chamber. The transmission monitor chamber usually stays put in a fixed position upstream from the beam exit window.

2.5.3 Gafchromic EBT3 Dosimetry Films

The following text is based upon the Gafchromic user manual (Gafchromic, 2014).

The Gafchromic EBT3 film is useful for dose measurements of high-energy beams. The composition can be seen in Figure 26, and the film contains three layers, with the active layer being sandwiched between two layers of polyester. The active layer consists of the active component, yellow marker dye and stabilizers. The yellow marker dye reduces the light sensitivity and aid the use of multichannel dosimetry. Due to its symmetric structure, the film can be irradiated from both sides, and the film comes in sheets of sizes 8” x 10”.

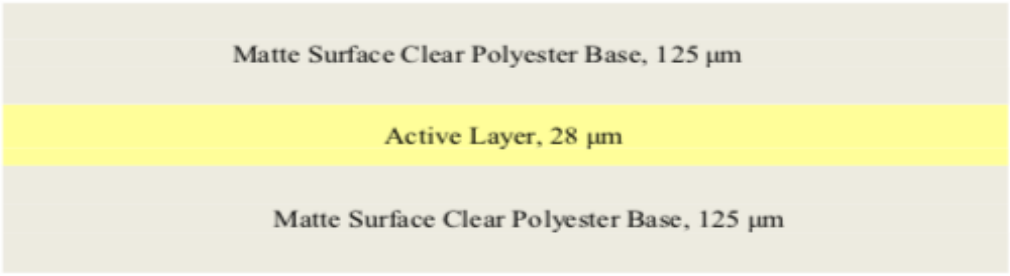

Figure 26 The Gafchromic EBT3 film consists of three layers with the active layer in the middle (Gafchromic, 2014)

Upon irradiation, the film is dyed and the optical density (OD), d_x, can be measured and related to dose. The scanning is done by using a flatbed RGB scanner that digitalizes the image. The film response is measured over red, green and blue wavelength bands. The net optical density (NOD) can be found by taken the OD-values from the irradiated films and subtracting the OD-values of unirradiated control films. Dose-response curves can then be made by plotting the NOD as a function of dose, and the data can be fitted to the function:

$$NOD = -ln\left(\frac{a + bD}{a + D}\right)$$

where D is the delivered dose and a and b are independent parameters.

2.6 Methods of analysis

2.6.1 Flow cytometry

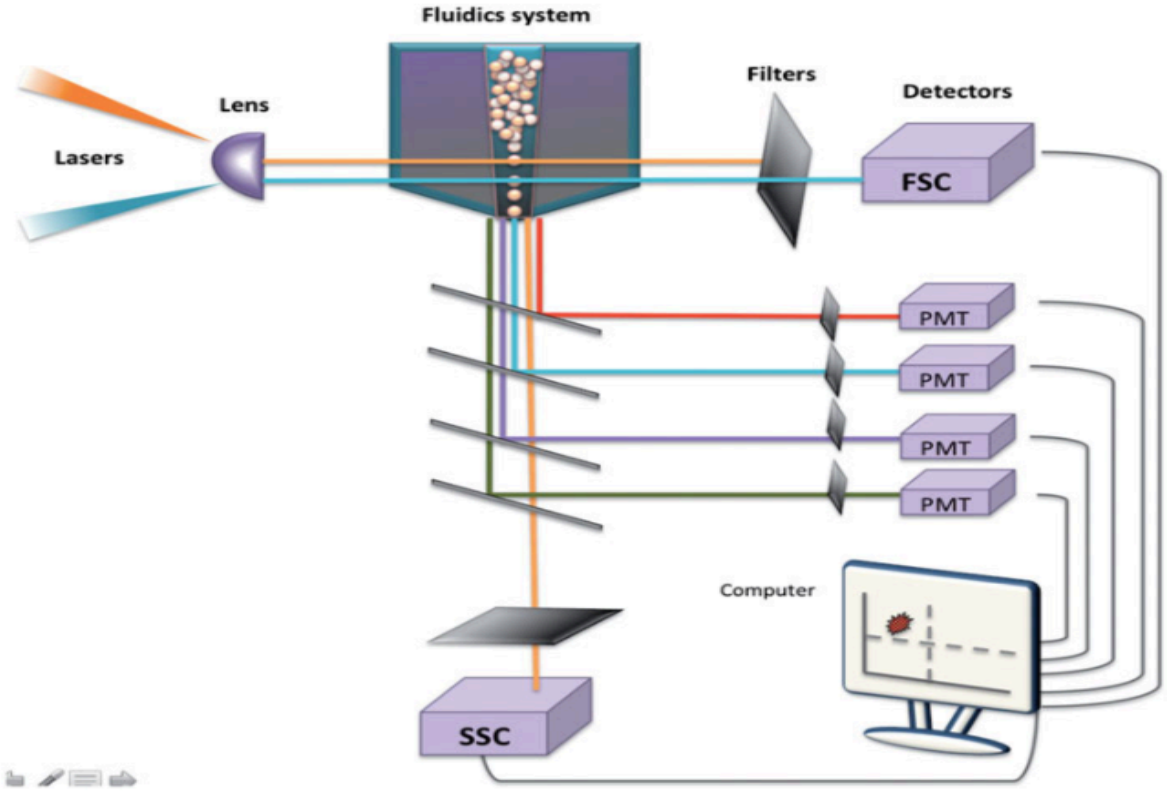

Figure 27 The flow cytometry system; the lasers and lens can be seen at the upper left corner, the cells enter and are sent through the fluidics system, the bandpass filters are used to distinguish wavelength spectra and assign them to the corresponding PMTs (detectors). The collected measurements are then processed and displayed on the computer (Adan, 2016)

The flow cytometer is an instrument with multiple uses in the investigation of cells characteristics such as size, optical density, granularity and fluorescence features. The underlying principle is connected to light scattering and fluorescence emission. Three main components comprise the flow cytometer; *the fluidic system*, *the optical system* and *the signal detection and processing* (Figure 27). A cell suspension is placed at the flow cytometer and cells are sent through the system – one by one – commonly by the use of pressure. The *fluidics* transports the cell from the cell suspension into the system in towards the laser beam. The rate at which the cells are transported can be manipulated by the user to match the purpose of the analysis. *The optical system* consists of the laser, lenses and the collection optics. The laser and lenses focus light towards the cell at an angle, and the forward scatter (FSC) and side scatter (SSC) are detected. In general, the forward scatter (FSC) is

proportional to the size of the cell, whereas the side scatter (SSC) says something about the granularity or internal complexity of the cell (Figure 28). The collection optics consists of the lenses that collect the light from the interaction and a system of mirrors and filters that separate and direct the collected light to the appropriate optical detectors. During the *signal detection and processing* the light signals are converted to voltages by photodiodes (PDs) or photomultiplier tubes (PMTs). Analog-to-digital converters process the signals to digital data that can be displayed as plots or histogram (Adan, 2016).

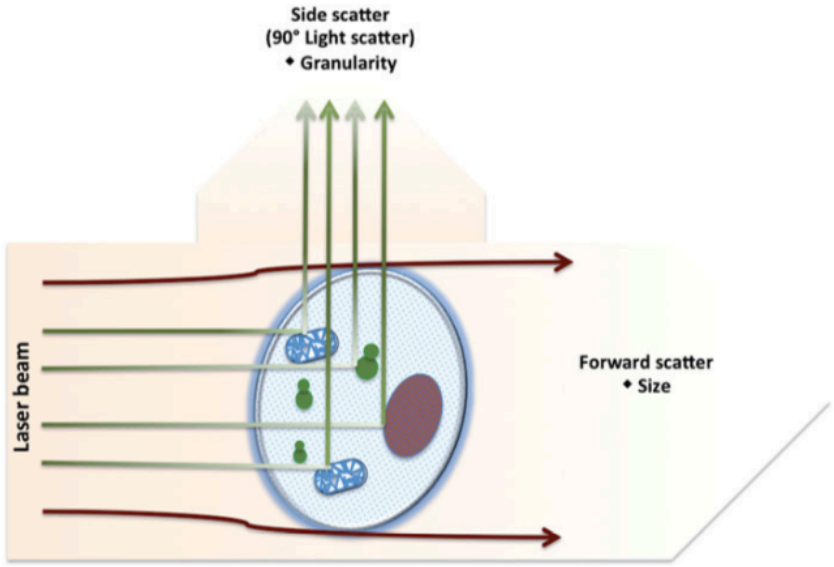

Figure 28 The principle of FSC and SSC are used to characterize size and granularity (Adan, 2016)

At the basis of flow cytometry is the principle of excitation and emission. The use of fluorochromes, also referred to as fluorophores or fluorescent dyes, takes advantage of the excitation/emission spectra of these labels when excited by a laser. When a fluorochrome absorbs light energy, an electron is excited and raised from its ground state to a level of higher energy (excitation). As the electron falls back to its ground state, a photon is sent out with energy corresponding to the difference between the excited state and the ground state (fluorescence). Staining the cell with such fluorochromes enable the user to retrieve information about a wide range of cell characteristics including cell-surface proteins, intracellular components, and DNA content to mention a few. The wavelength of the emitted photon is always longer than the excitation wavelength, and the separation between the two is referred to as the Stoke's shift. Generally, the larger the separation, the better the

fluorochrome. Since the excitation wavelengths and the emission wavelengths are of different colors, the optical filters can be used to separate the two. It should be noted that the excitation and emission of fluorochromes consist of a spectrum of wavelengths, with a maximum within these spectra. In flow cytometry applications, fluorochromes can be used to label antibodies of interest that are then incubated together with the cells to bind to the target antigen (Adan, 2016).

3 Materials and methods

3.1 Tumor-cell lines and techniques

3.1.1 Cell lines

The two cell lines used in the experiments of this thesis are T98G human glioblastoma multiforme cells and A549 human epithelial lung carcinoma cells. The T98G cell line originates from a 61-year old Caucasian male, whereas the A549 cell line is extracted from a 58-year old Caucasian male. The cell lines were purchased from the American Type Culture Collection, ATCC.

3.1.2 Cell cultivation and seeding

The experiments performed in this thesis lasted for maximum five working days. Due to the short duration of each experiment less stringent requirements were necessary in terms of cultivation and seeding. First of all, for the majority of the experiments, cells were "ordered" from Joe Alexander Sandvik, who provided pre-seeded cells so that only irradiation and analysis were necessary. However, for a couple of the experiments the seeding was done by the author.

Heated Trypsin EDTA was used to loosen the cells from the flasks in order to obtain a cell suspension. The cells were then seeded with various degrees of dilution depending on the cell line used, and the sizing of the flasks/dishes. Additionally, the number of days from the seeding took place to the analysis was to be performed predicted the dilution of the cell suspension. All cell treatment during seeding and cultivation was performed under sterile conditions in the Laminar Air Flow (LAF) bench (Gelaire, Australia and Safe 2020, Thermo Scientific).

The cells were grown in flasks or dishes of various sizes depending on the format of the experiment. The T98G cell line was cultivated in RPMI 1640 medium (Lonza, Belgium) with serum added. The A549 cell line was maintained in DMEM/F12 medium (Lonza, Belgium). During incubation, the flasks or dishes were maintained in either Thermo Scientific Steri-Cycle CO2 incubator (Thermo Scientific Forma, USA), Steri-Cult 200 CO2 incubator

(Thermo Forma 3307, USA) or Thermo Forma Series II, Water Jacketed CO2 Incubator (Forma Scientific, USA) at 37° C, 80% humidity and 5% CO_2. During all handling with cells, sterile gloves (Gammex, Ansell) or unsterile gloves (Nitrile, VWR) were used.

3.2 X-ray irradiation

3.2.1 Preparation

Each experiment that required x-ray irradiation was performed at the Røntgen laboratory in the basement of the chemistry building at UIO (room VK08). At the day of the experiment, the x-ray machine (PANTAK PMC 1000, Pantak, USA) and the water bath was turned on approximately thirty minutes before irradiation in order to warm up the system. The steel trays that were used to house the cell dishes during irradiation were cleaned with ethanol and placed inside the LAF bench, also in the basement, which holds a temperature of 37°C. Trying to maintain a temperature of 37°C for the cells is an attempt to keep conditions close to that of an in vivo setting. Additionally, the LAF bench in the cell-lab at the third floor of the chemistry building was turned on approximately thirty minutes before irradiation. This LAF bench was used to seal the cell dishes with a strip of parafilm during irradiation, and the parafilm was added just before the cell dishes were taken down to the basement. In those cases that cell flasks were to be irradiated, no parafilm was needed, instead the lid of the flasks were closed tightly. In order to keep conditions as sterile as possible, the cell dishes and flasks were transported to the basement on a sterile tray and wrapped in a sterile cloth.

3.2.2 Set-up and dosimetry

During the first experiments the dosimetry was already performed by someone else, so that the dose rate at a given source-skin distance (SSD) was used to calculate the time period of irradiation to achieve the required dose. In March the set-up of the x-ray machine was changed, additional shelves were added and the water bath was removed and replaced by an internal temperature regulator. This new set-up required a new dosimetry to be performed. By using a plane-parallel chamber (Scanditronix, Welhofer, IBA) connected to an electrometer (MAX-4000) in different positions in a plane, the field size and dose rate at various shelf-levels (SSDs) were identified. The dose rate could then be used to identify the time of irradiation necessary to achieve a certain dose. The new configuration meant that the

irradiation could be performed quicker if few dishes or flasks were to be irradiated, as this required a smaller field size and the irradiation could then be performed closer to the source (low SSD).

3.2.3 X-ray irradiation

The steel tray containing the cell dishes where placed at the tray inside the x-ray unit and the settings were adjusted at the control unit. The voltage was set to 220 kV for all experiments and the current to 10 mA. Then the irradiation time was entered according to what dose was to be delivered at that particular experiment. Once the irradiation was completed, the dishes were taken back to the incubator at the cell lab upstairs wrapped in the cloth, and carried at the tray. The x-ray tube was cooled down and then turned off approximately thirty minutes after irradiation.

3.3 Proton irradiation

All proton irradiation experiments were performed at Oslo Cyclotron Laboratory (OCL) using the Scanditronix MC-35 cyclotron (Scanditronix, Uppsala, Sweden).

3.3.1 Preparation

The allocated time at the OCL was given in bulks of 3 and 5 consecutive days for each proton experiment. This meant that preparation had to be done beforehand, in order to have enough time to perform the irradiations. As we were three master and PhD students sharing the allocated time between us, clear plans in terms of time management had to be in place. Therefore, all equipment necessary at the days of irradiation were placed at the laboratory at OCL the prior week. The equipment included autoclaved or sterile laboratory coats, trays, cloths and gloves. In addition, an electronic pipette (Pipetus, Hirscmann) and the corresponding pipettes (Sarstedt), a waste tray for disposal of medium, adhesive tape to attach the cell dishes to the PMMA cell containers and a trash bin were stacked at the laboratory. Parafilm (Parafilm M Laboratory film, Bemis) was cut into strips and lids and soaked in 70% ethanol for 20 minutes and left to dry over-night in the LAF-bench (Thermo Scientific) before being placed in sterile, closed glass dishes.

On the day of the irradiations, medium was heated for use, and taken to the laboratory. The cell dishes were placed in the incubator at the laboratory and the PMMA containers to hold the cell dishes during irradiation were sterilized and heated.

At the time of irradiation, each cell dish was placed in the LAF-bench and medium was removed. This was due to the vertical position the cell dishes had to be in while irradiated. The time period each dish was without medium was recorded. For those dishes that were to receive low-LET radiation (at the front of the Bragg peak), the parafilm lid was applied and secured with adhesive tape. The dishes to be irradiated behind the Bragg peak, were irradiated with the original lids on secured with tape.

3.3.2 Set-up and dosimetry

Dosimetry had to be performed at the beginning of each irradiation day due to fluctuations in the energy of the proton beam. As a result, the position of the Bragg peak also needed to be established each day. Firstly, EBT3 films were placed in front of the beam exit window and irradiated to measure the beam homogeneity. The beam centration was then checked and tuned. Next, dosimetry measurements were done by using a monitor chamber (MC) and an ionization chamber (IC). A tungsten scattering filter of 50 μm was placed at the beam exit window. The monitor chamber measured the fluence of particles and the calibration was done by measuring the dose rate of the ionization chamber for a given monitor chamber fluence. The ionization chamber was therefore placed in the position where we wanted to irradiate the cells, which was at the front and at the back of the Bragg peak. The ionization chamber then gave the dose at these positions at a given fluence. During irradiation of the cells the MC stayed in the set-up to monitor the fluence, whereas the ionization chamber was removed and replaced by the cell container. Additional irradiations of these positions by the use of EBT3 films were also done to later be able to analyze the dose profiles. The monitor chamber was placed at 35 cm from the exit window. The set-up can be seen in Figure 29.

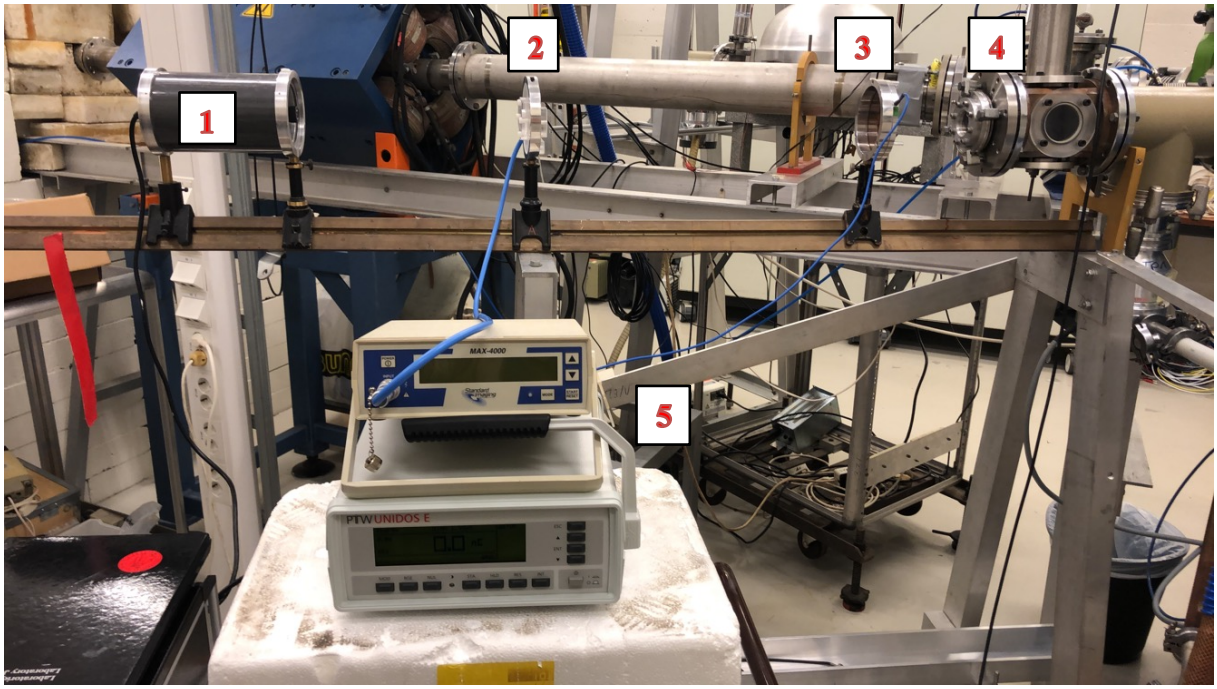

Figure 29 The set-up used during the proton irradiations; 1. Cell container, 2. Ionization chamber, 3. Monitor chamber, 4. Beam exit window, 5. Electrometers

In order to irradiate the cells with the preferred doses and positions of the Bragg curve, we needed to firstly identify the positions at the front, at the top of and at the back of the Bragg peak, and secondly measure the dose rate at these positions with a given fluence.

To find the front of the Bragg peak the lid of the cell dishes had to be removed. This is because the lid would otherwise act as an absorber and thereby make it impossible to irradiate at the front of the Bragg peak. Therefore, sterile parafilm sheets were used instead of a lid for those cell dishes that were to be irradiated in position a. Then, to identify the position corresponding to the back of the Bragg peak the lid was added and the position of the ionization chamber containing the cell dish was adjusted to the position that gave the same dose and dose rate as was found for the front of the Bragg peak. By identifying the two positions (front and back of Bragg peak) that gave the same dose and dose rate, we could make the assumption that any difference in results was due purely to an LET-effect. The top of the Bragg peak was then assumed to be in the midpoint between these two positions.

3.3.3 Proton irradiation

During irradiation one cell dish at a time was transferred from the incubator to the LAF bench, the medium was removed and the lid was either removed and replaced by a parafilm

lid (front of Bragg peak) or the lid was kept and sealed with a strip of parafilm (behind Bragg peak). Then the dish was placed in the cell container and which had been warmed up to 37°C in the incubator. The cell container with the cell dish was then quickly transferred to the heated cell container in the irradiation position and irradiated before it was returned to the LAF bench, parafilm was removed and medium added and the dish was placed back in the incubator. During the irradiation of one cell dish, the next one was prepared. All dishes that required irradiation in a specific position were irradiated consecutively, before another dosimetry was performed to find the next position and so on.

3.4 Calreticulin assay

The detection of calreticulin was largely based on the protocol received from Adrian Eek Mariampillai and his team of the Radiation Biology and DNA Damage Signaling group at the Institute for Cancer Research at Radiumhospitalet but necessarily adapted to fit our experiments.

The samples were analyzed 48 hours post-irradiation. The unirradiated control cells were stained (barcoded) with DyLight 650/medium for approximately 30 minutes. The irradiated samples were trypsinized with TrypLE Express and made into a cell suspension with the complementing medium depending on cell line. Then, the irradiated cells were centrifuged (Beckman) and re-suspended in Phosphate Buffered Saline (PBS) (Lonza, Belgium). The barcoded control cells were then added to the irradiated samples and each sample split into two, followed by a washing step and then put on ice. One of the two samples was stained with the primary antibody CRT in bovine serum albumin (BSA) in PBS. The other split sample was only given the same volume of BSA/PBS. All samples were incubated in the dark for 30 minutes and then washed two times. The secondary antibody Alexa Fluor 488 was then added and the samples were again incubated in the dark for 30 minutes followed by two washing steps. 5 minutes prior to flow cytometry analysis, 1 μl of 1mg/μl propidium iodide (PI) was added for live/dead staining. The dilution of barcoding (DyLight 650), primary antibody, secondary antibody or fluorochrome-conjugated antibody is specified in each result display of the experiments. The protocol is found in Appendix C.

For clarity, each sample that was analyzed in the flow cytometer contained a mixture of control cells and irradiated cells. Additionally, each sample containing the two cell

populations had a complementary sample. Specifically, one sample was treated with both the primary and the secondary antibody, whereas the complementary sample was only treated with secondary antibody.

Note: when the fluorochrome-conjugated antibody was purchased, the incubation of antibody steps was reduced from two to one, which meant that the splitting of samples was also eliminated.

3.5 Flow cytometry analysis

The analysis of the cell characteristics for both x-ray and proton irradiation were performed using the BD Biosciences Accuri C6 flow cytometer located at the Biophysics department at UiO.

The flow cytometer contains a blue and a red laser, two light scatter detectors and four fluorescence detectors (Figure 30). The fluidics is driven by a low-pressure pumping system, and up to 10,000 events pr. second can be counted.

Figure 30 The BD Accuri C6 flow cytometer showing the four fluorescence detectors (Biosciences, 2013)

Table 4 Recommended optical choices for the specified fluorochromes (Adapted from (Biosciences, 2013))

Dye	Laser	Standard filters	Detector	Experimental use
Alexa Fluor 488	488 nm (blue)	533/30	FL1	Calreticulin
PI	488 nm (blue)	585/40	FL2	Viability
-	488 nm	>670	FL3	Not used
Alexa Fluor 650	640 nm (red)	675/25	FL4	Barcoding

FCS and SSC was used to remove the debris and dead cells. Additionally, the FL-2 channel displaying proprium iodine (PI) content was used to further exclude dead cells. PI is assumed to not be present in viable cells so that cells in the process of dying with a broken membrane will have an uptake of PI. The viable cell population was then analyzed by display in the FL-4 channel to distinguish the control cells from the irradiated cells by amount of DyLight 650 content. Lastly, the FL-1 channel was used to identify the median calreticulin level for the control cells and the irradiated cells separately.

3.6 Statistical analysis

3.6.1 Wilcoxon signed-rank test

The Wilcoxon signed-rank test is a nonparametric statistical test appropriate for data sets where the underlying assumptions of parametric tests are not met (e.g. paired t-test requires a normal distribution of the differences) (Whitley, 2002). A comparison is made between a sample data relative to a reference value and the magnitude of the difference is taken into account (Nahm, 2016). The significance level (p-value) and the use of a one- or two-tailed hypothesis can be chosen and employed in combination with the Wilcoxon signed-rank test.

3.6.2 Linear regression

Linear regression analysis provides a tool to look at relationships among various factors and is commonly used in statistical analysis of medical data. It is based on studying the behavior of a continuous, dependent variable, Y, of interest. The independent variable, X, provides some sort of information about the behavior of this dependent variable and can be continuous, binary or categorical.

The data should initially be displayed in a scatter plot to get a sense of whether there is a linear relationship between the dependent and independent variables or not. Other techniques of analysis must be used if the relationship is nonlinear.

Linear regression can be *univariable* or *multivariable*. In univariable linear regression, the relationship between the dependent variable and a single, independent variable is analyzed. The model then characterizes the dependent variable by a straight line:

$$Y = a + bX$$

where *a* is where the line intersects the ordinate and *b* describes the slope of the line and is referred to as the regression coefficient. This regression coefficient indicates the degree of contribution of the independent variable in describing the dependent variable.

The coefficient of determination, r^2, gives an estimate of how well the variance of the data is described by the regression model. Specifically, the coefficient of determination means that the variance in the dependent variable is due to the independent variable, and a high r^2 value is therefore desirable. r^2 is calculated as follows:

$$r^2 = \frac{\sum_{i=1}^{n}(\hat{y}_i - \bar{y})^2}{\sum_{i=1}^{i}(y_i - \bar{y})^2} = \frac{explained\ variance}{overall\ variance}$$

where $\hat{y}_i$ is the model's estimated values, y_i are the observed values and $\bar{y}$ is the mean of the values. However, the coefficient of determination has a weakness in that it can be manipulated to become high by increasing the number of independent variables. Consequently, *the adjusted coefficient of determination,* r^2_{adj}, is a better option. A rise in the adjusted coefficient of determination when increasing the number of independent variables only occurs if the rise in r^2 is greater than what would be expected by chance.

Multivariable linear regression can be used whenever various independent variables are needed to describe the dependent variable. In such cases, the regression line becomes:

$$Y = a + b_1X_1 + b_2X_2 + \cdots + b_nX_n,$$

and a regression coefficient, b_i, is calculated for each independent variable, X_i *(Schneider, 2010)*.

4 Results and analysis

The table below shows an outline of all experiments that were performed during the work of this thesis. Experiments that have been completely excluded from the results for various reasons are outlined in red.

Table 5 Overview of all experiments performed during this thesis (2018-2019). Experiments that were left out of the analysis for various reasons are highlighted in red.

Experiment no.	Date	Irradiation	Cell line	Comment
1	12.09-14.09	X-rays	T98G	
2	01.10-05.10	X-rays	T98G	No controls in samples
3	09.10-12.10	X-rays	T98G	
4	29.10-02.11	X-rays	T98G	
5	13.11-16.11	X-rays	T98G	
6	20.11-22.11	X-rays	A549	Very low cell count
7	26.11-30.11	Protons	T98G	
8	09.12-11.12	X-rays	T98G A549	Flow cytometer broke down, all samples had to be thrown out
9	15.01-18.01	X-rays	T98G	Flow cytometry performed at the Radiumhospital
10	30.01-01.02	X-rays	T98G	Flow cytometry performed at the Radiumhospital
11	04.02-07.02	X-rays	T98G A549	Hard to distinguish irradiated cells from control cells for T98G, impossible for A549

12	18.02-23.02	Protons	T98G A549	
13	11.03-15.03	X-rays	T98G	BC test, Confluence test Autofluorescence test
14	25.03-27.03	X-rays	T98G	Dilution test for new, conjugated AB
15	26.03-28.03	X-rays	T98G	Autofluorescence test
16	03.04-05.04	X-rays	T98G	Fixation test
17	08.04-12.04	Protons	T98G A549	
18	26.06-28.06	X-rays	T98G	Confocal microscopy test run (no data retrieved)

The processing and analysis of the data are primarily divided into a more qualitative protocol specific analysis and evaluation of the data by more formal methods such as linear regression and bar plots. Note that when the term ‘measured fluorescence’ is used in the following chapters, it refers to the median fluorescence values measured by the FL-1 channel that is used for calreticulin detection unless otherwise specified.

4.1 X-rays

Over the course of this thesis, the subject of interest included calreticulin accumulation on the cell surface following x-ray irradiation. Due to practical problems and time constraints, all experiments with x-rays were done with T98G cells. The doses varied from 4 to 8 Gy for each fraction and up to two fractions were given. The analysis of the experiments using x-ray

irradiation were mainly performed using the unconjugated antibodies, which required two steps of labeling. The control cells added to each irradiated sample provided a baseline in the evaluation of the fluorescence. Bar plots were chosen to be the best display method and each bar was generated by using the following calculation from the median fluorescence values:

$$Ratio = \frac{Irradiated\ (p+s) - Irradiated\ (s)}{Control\ (p+s) - Control\ (s)}$$

where 'irradiated' represents the cells irradiated with a certain dose and 'control' refers to the unirradiated cells. 'p' and 's' represents the primary antibody and the secondary antibody respectively. The results varied with some experiments showing a clear increase in membrane-bound calreticulin after irradiation and others not showing any response.

4.1.1 Data showing membrane bound calreticulin after x-ray irradiation

Three separate experiments are displayed in Figure 31. The x-ray doses vary between one and two fractions of 4 or 8 Gy. Primary and secondary antibody (unconjugated antibody) has been used in all the x-ray experiments displayed. Each bar represents the median fluorescence measured in the FL-1 channel of an irradiated sample divided by the median fluorescence of the barcoded control sample. The top panel (purple bars) shows two duplicates from September that have been treated with the same fractionation and dose. Variation in the fluorescence is seen. The mid-panel displays an experiment from November where a combination of doses and fractionations have been used. Notice that the highest ratio of fluorescence between the irradiated samples and the control samples is found when using two fractions. The lower panel displaying data from January demonstrate the largest fluorescence ratio for the sample receiving two fractions of 8 Gy. However, one fraction of 4 Gy and one fraction of 8 Gy rendered a ratio of close to one, implying no significant difference between the fluorescence of the irradiated sample compared to the control sample.

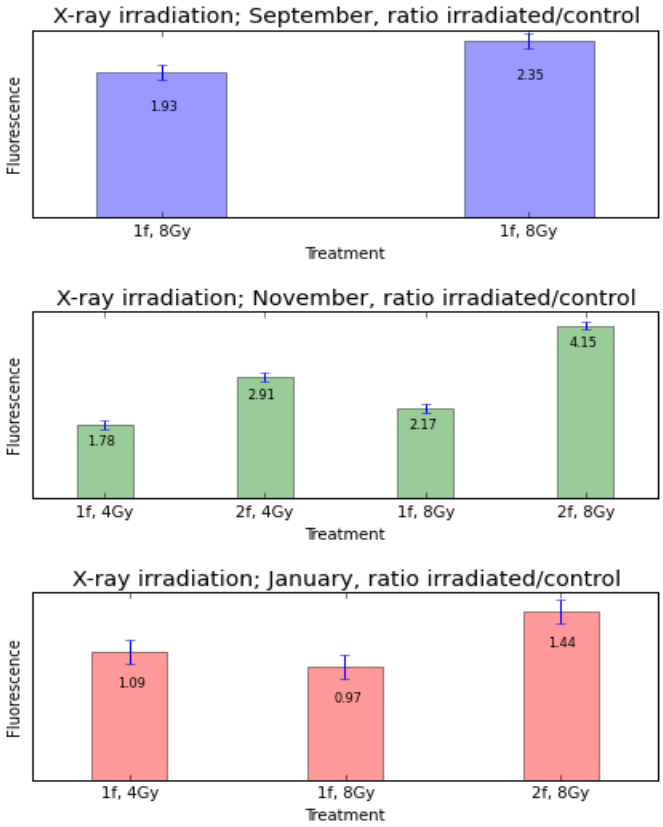

Figure 31 Shown are the results of three separate x-ray experiments with the T98G cell line. The dilutions were as follows; DyLight for barcoding 1:100, primary AB 0.5:100, secondary AB 0.25:100. The flow cytometry for the two upper experiments were performed at the Biophysics building at UiO, whereas the experiment in the lower panel was performed at Radiumhospitalet.

4.1.2 Data not showing membrane-bound calreticulin after x-ray irradiation

Figure 32 shows a selection of the experiments that generated results that could not be attributed to cell-surface accumulation of calreticulin. Unconjugated antibody was used for both experiments. A negative ratio (left panel) indicates that the measured fluorescence of cells treated with only secondary antibody was larger than the cells treated with both primary and secondary antibody. A ratio < 1 indicates that the measured fluorescence in control cells exceeded the measured fluorescence of the irradiated cells. The experiments conducted in the fall of 2018 (September-November) were done without assistance from a supervisor and it is possible that lack of routine with the assays played a role in the varying results.

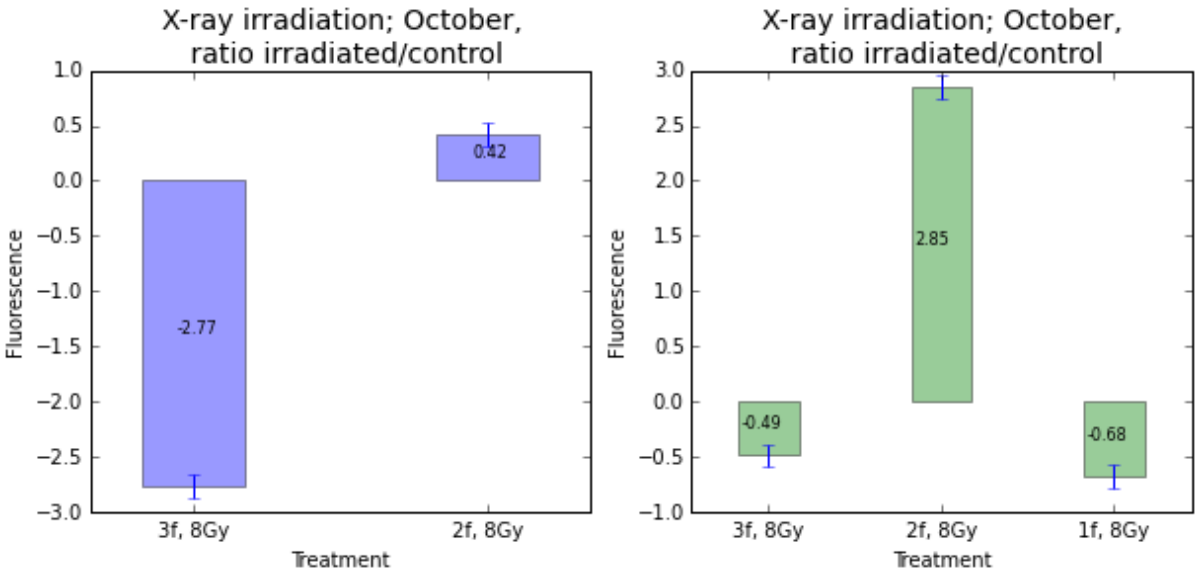

Figure 32 Two separate experiments showing questionable results. Both panels display a negative ratio in the fluorescence of the irradiated sample to the control sample. This indicates higher measured fluorescence from the cells treated only with secondary antibody compared to the cells treated with both primary and secondary antibody. The right bar of the left panel also demonstrates a ratio < 1. This means that the measured fluorescence of the control sample gave a higher median value than that of the irradiated sample. The same dilution factors and treatment were used as previously.

4.2 Protons

Three weeks of proton irradiation were performed for this thesis. Irradiation at the front of the Bragg peak and at the back of the Bragg peak were of specific interest due to the differences in LET for these positions. The position at the back of the Bragg peak was carefully selected to give the exact dose rate as at the front of the Bragg peak. In this way, the effect of LET could be singled out.

The same formula as was used for x-ray irradiation was employed for the proton irradiated data:

$$Ratio = \frac{Irradiated\ (p+s) - Irradiated\ (s)}{Control\ (p+s) - Control\ (s)}$$

This ratio was calculated for each sample irradiated either at the front of the Bragg peak or at the back of the Bragg peak. When these ratios were retrieved, an additional calculation was made by dividing the (ratio) value found for the back of the Bragg peak by the value representing the front of the Bragg peak for each dose. In this way, it is possible to do a comparison of the measured fluorescence by the FL-1 channel at the back of vs. the front of the Bragg peak in terms of LET-effect.

4.2.1 Dosimetry and correction factors

The ionization chamber (IC) that was used during the irradiation to measure the dose rate had a radius of 2.5 mm and so the purpose of the film dosimetry was to give an indication of the homogeneity of the dose distribution hitting the area of the cell dish, which has a diameter of 5 cm. The results from the Gafchromic EBT3 dosimetry films for each of the proton experiment weeks are displayed in Table 6. The average dose received at the center of the film using a radius of 2.5 mm was compared to the average dose received using a radius of 2.5 cm in order to mimick the area of the cell dishes. The result of the dosimetry analysis is therefore a correction factor to the doses received by the cell dishes during proton irradiation and is found by dividing the average dose with a radius of 2.5 mm by the average dose with a radius of 2.5 cm. A script made by Anne Marit Rykkelid (UiO) was used to perform the calculations. It should be noted that dosimetry films were not obtained for every day of proton irradiation but as a minimum of one day per experiment week.

Table 6 Dose correction factors and standard deviations (SD) obtained from the proton weeks in November, February and May with the use of Gafchromic EBT3 dosimetry films.

Date	Absorber	Average dose, 15 pix.	SD 15 pix.	Average dose, 145 pix.	SD 145 pix.	Correction factor	Sd corr. factor
06.05.19	0	1,86	0,06	1,66	0,13	**0,90**	**0,07**
19.02.19	0	4,09	0,09	3,72	0,25	**0,91**	**0,06**
20.02.19	0	4,70	0,12	4,27	0,42	**0,91**	**0,09**
21.02.19	0	6,64	0,17	5,83	0,63	**0,88**	**0,10**
22.02.19	0	4,54	0,12	3,97	0,39	**0,87**	**0,09**
27.11.18	parafilm	8,48	0,16	7,33	0,73	**0,86**	**0,09**

The results show that the correction factor ranges from 0.86 to 0.91 with a standard deviation of 6 to 10 percent. Two of the scanned films from November and February can be seen in Figure 33.

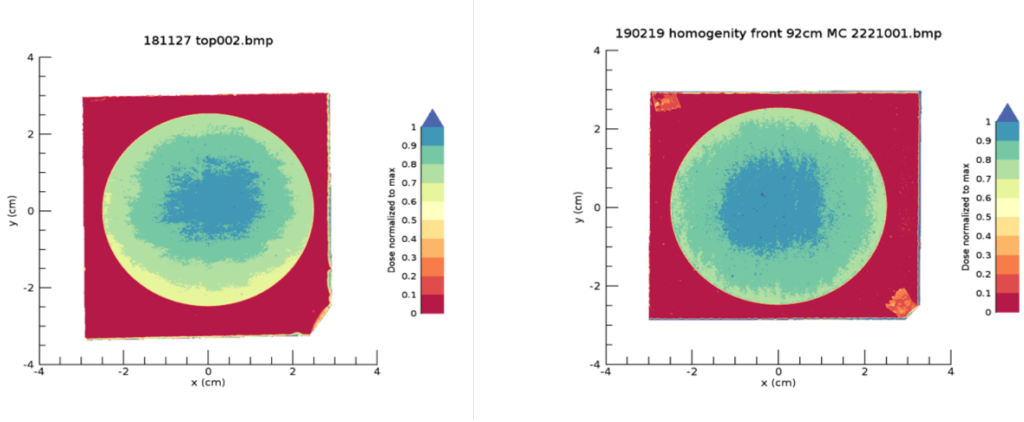

Figure 33 A selection of scanned Gafchromic EBT3 dosimetry films. The dose distribution intensity normalized to maximum is represented by the different colors, see right handside for scale.

4.2.2 Calreticulin measurements after proton irradiation

Figure 34-Figure 39 show the results for the two cell lines (T98G and A549) from the proton irradiation experiments from November, February and May. The left panel shows the ratio of fluorescence of the irradiated cells to the control cells for each position of the Bragg peak and each dose regime. Position a corresponds to the front of the Bragg peak whereas position c corresponds to the back of the Bragg peak. "*1f, 4 Gy, pos a*" means that the cell dish has been irradiated with only one fraction of 4 Gy and the position of the cell dish during irradiation corresponds to the front of the Bragg peak. "*2f, 8 Gy, pos c*" on the other hand, means two fractions were given with a dose of 8 Gy for each fraction, and that the cell dish was placed in the position corresponding to the back of the Bragg peak. The T98G cell line is displayed in purple and the A549 cell line in green. The right panel shows the ratio of the same fluorescence when the value of position c is divided by the value of position a.

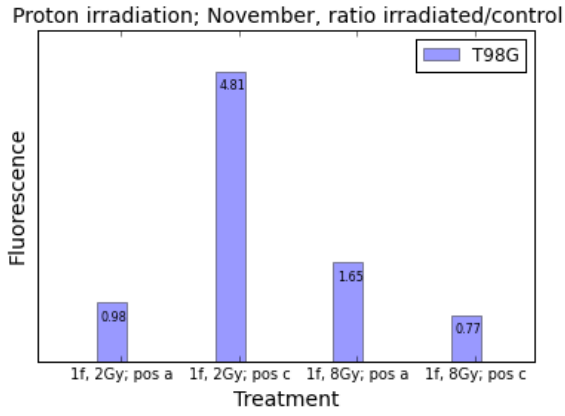

Figure 34 Results showing the ratio of median fluorescence of the irradiated cells to the control cells for each dose and position in the Bragg peak from November. The dilution factors were: DyLight for barcoding; 1:100, primary AB; 1:200, secondary AB; 1:400.

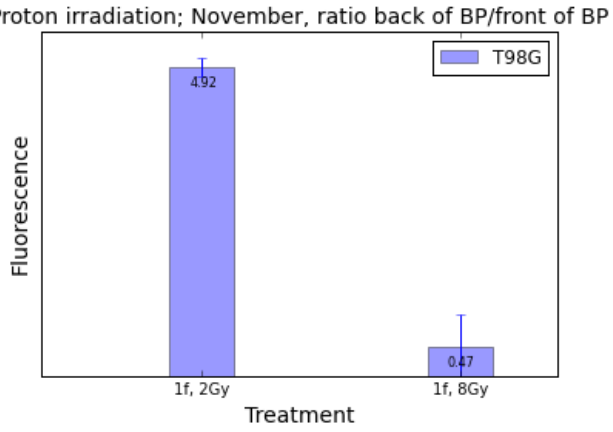

Figure 35 The same data as the previous figure but the ratio of the median fluorescence at the back of the Bragg peak (position c) to the median fluorescence at the front of the Bragg peak (position a) is displayed..

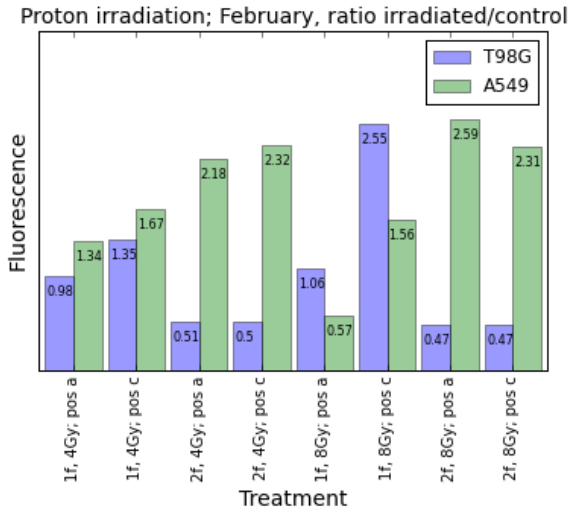

Figure 36 Results showing the ratio of median fluorescence of the irradiated cells to the control cells for each dose and position in the Bragg peak from February. DyLight for barcoding dilution 1:100. Primary AB dilution 1:200, secondary AB dilution 1:1000.

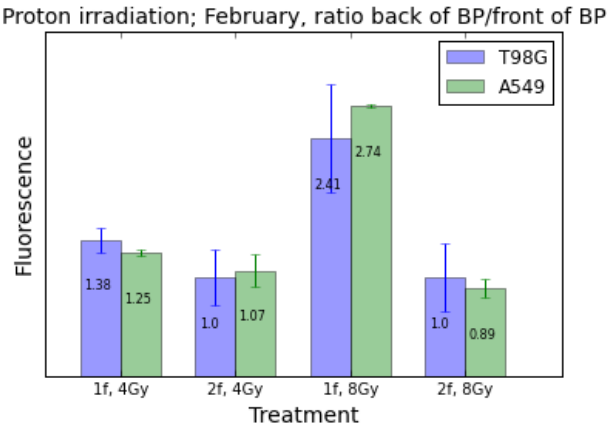

Figure 37 The same data as the previous figure but the ratio of the median fluorescence at the back of the Bragg peak (position c) to the median fluorescence at the front of the Bragg peak (position a).

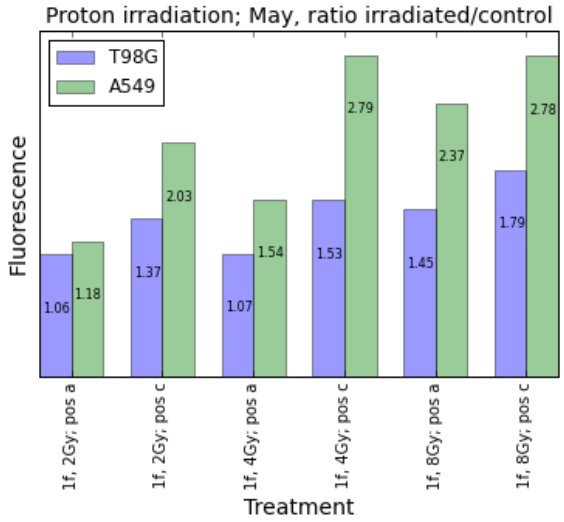

Figure 38 Results showing the ratio of median fluorescence of the irradiated cells to the control cells for each dose and position in the Bragg peak from May. DyLight for barcoding dilution 1:100, fluorochrome-conjugated AB dilution 1:250.

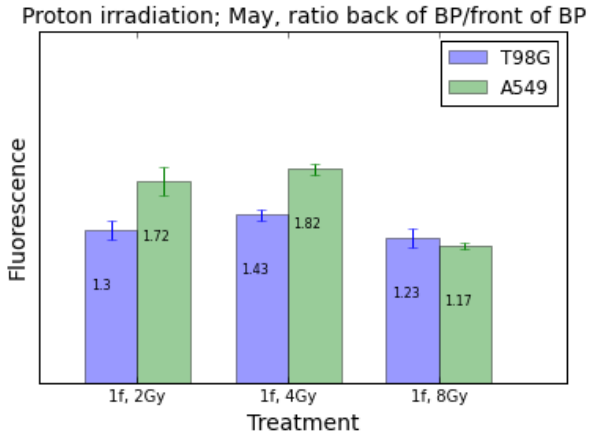

Figure 39 The same data as the previous figure but the ratio of the median fluorescence at the back of the Bragg peak (position c) to the median fluorescence at the front of the Bragg peak (position a).

It should be noted that the data from February and especially May are likely to be more reliable than the data from November. This is a result of more practice in performing the assay, better structure in how to handle large amounts of cell dishes during the proton irradiation weeks and ongoing protocol optimization. The data from May are the only data that have been retrieved using the fluorochrome-conjugated antibody. As will be discussed in further sections, the fluorchrome-conjugated antibody appears to be the most reliable.

From the all proton data Figure 34-Figure 39 it is evident that the fluorescence varies across the experiments for the same cell line even with equal doses and fractionations. However, if we look at Figure 38 and Figure 39 (the most reliable experiments), there are two observations that can be made. First, there generally seems to be a higher fluorescence signal for the A549 cell line compared to T98G for all irradiations. Second, there appears to be a saturation in the signal for A549 cells. Figure 38 shows that an increase in dose from 4 to 8 Gy at the back of the Bragg peak (position c) does not increase the signal for A549 cells. The same tendency of saturation for A549 cells is seen in the experiments from February (Figure 36) when comparing 1 or 2 fractions of 4 or 8 Gy (position c). The fluorescence from T98G cells never reach the level that showed saturation for A549 cells but there could be an indication of a similar effect.

4.3 Tests and protocol optimization

As a result of inconsistencies in results and difficulties in replicating the results of the first experiments, several tests were conducted in order to improve and optimize the analysis.

4.3.1 Barcoding incubation time test

A T75 flask was irradiated with 8 Gy. Analysis was performed at 48 hours post-irradiation. The cells where mixed with control cells incubated for either 3 hours or 30 minutes with DyLight. The results showed little difference: for the sample with the barcoding that had incubated for 30 minutes (normal time), the FL-1 values gave a ratio of 1.15 and for the sample containing cells that had incubated for 3 hours the ratio was 1.13, only a 1.8% difference. (Note: these data were only calculated from the flow cytometry output and are not displayed).

4.3.2 Fixation test

The data from samples using only secondary antibody or no antibody at all showed an increase in fluorescence upon irradiation even when only secondary antibody had been used. This has never been a problem with fixated cells used in other types of experiments. However, the experiments of this thesis were performed without any fixation. The reason for this is that fixation usually results in permeabilization of the cell membrane and likely cause leakage of intracellular content such as calreticulin. This would compromise the integrity of the results. However, it was decided to perform an experiment using fixation with 1% formaldehyde. The results can be seen in Figure 40. The left panel shows the difference in fluorescence between irradiated cells vs. unirradiated cells as a function of treatment (antibody/no antibody, fixation/no fixation). The right panel shows the difference in fluorescence between fixated samples vs. non-fixated samples as a function of antibody treatment.

The fixation test demonstrated that fixation slightly reduced the measured fluorescence in all samples (Figure 40, right panel). The highest reduction was seen for the irradiated cells (up to 15%). It can also be noted that the two bars seen at the very left in the left panel of Figure 40 displaying the unirradiated sample in purple and the irradiated sample in green having received no antibody treatment and no fixation, reveal that the measured fluorescence is

significantly higher for the irradiated sample (>37%). This is clearly problematic in terms of the validity of the results in calreticulin detection. This issue is further addressed at a later stage.

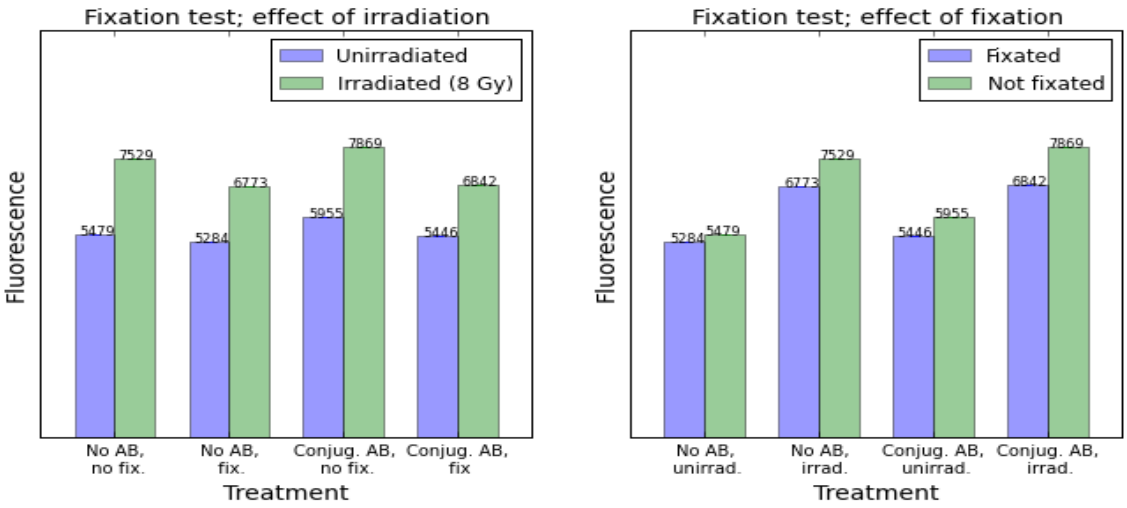

Figure 40 The left panel shows the measured fluorescence of the irradiated cells (green) and the unirradiated cells (purple) as a function of antibody treatment and fixation/no fixation. The right panel shows the fixated cells (purple) and the cells that were not fixated (green) as a function of antibody and irradiation/no irradiation. Dilution factors were: Fluorochrome-conjugated antibody; 1:250, and 1% formaldehyde in 500 µl PBS for fixation.

4.3.3 Titration

To avoid non-specific binding of the secondary antibody, a fluorochrome-conjugated primary antibody was purchased. This is the antibody used in the proton experiments from May (Figure 38 and Figure 39). A titration test was performed to arrive at the optimal dilution of antibody to PBS. The results of this test can be seen in Figure 41. The largest difference in measured fluorescence between the irradiated sample and the control samples was found for a dilution of 1:100 and the smallest difference was found for a dilution of 1:250. It was, however, desirable to reduce the impact of background fluorescence as much as possible, so the dilution of 1:250 was chosen since this resulted in the lowest fluorescence value for the control sample.

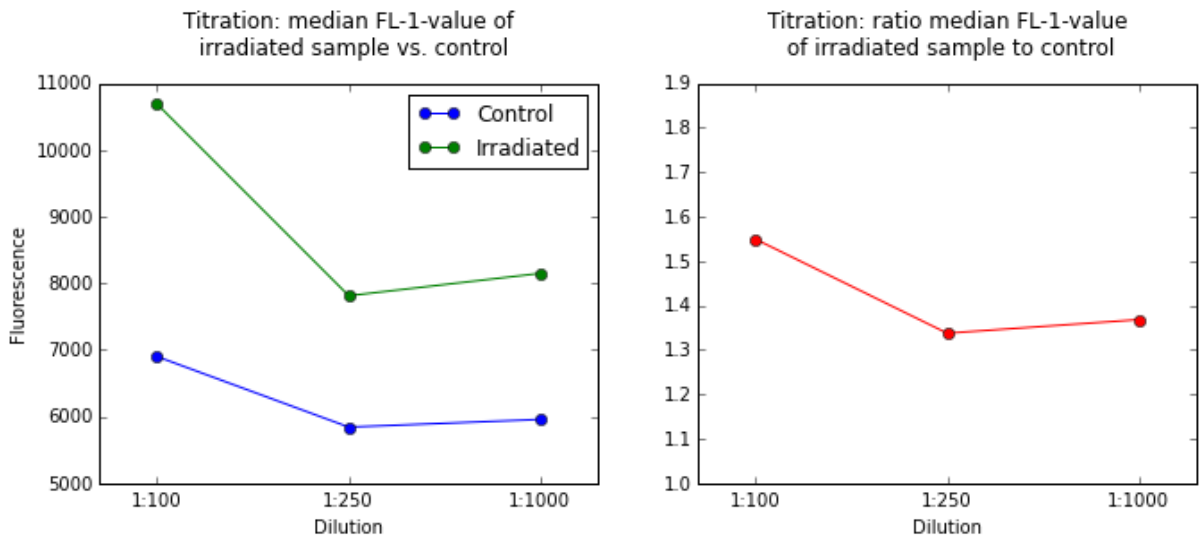

Figure 41 A titration was performed using the newly purchased fluorochrome- conjugated antibody to find the optimal dilution of antibody/BSA-PBS. The irradiated sample had received an x-ray dose of 8 Gy. The left panel shows the results for both the control without antibody treatment and the irradiated sample having received normal antibody treatment. The right panel shows the same data for the irradiated samples, but the fluorescence values have been normalized to the fluorescence values of the untreated control.

4.3.4 Channel sensitivity

The new fluorochrome-conjugated antibody avoided the problem of non-specific secondary antibody, but there still was the worry of an increase in fluorescence in the FL-1 channel from irradiation alone (without antibody added). To explore if this was specific for this channel, an analysis of the fluorescence measured by all channels of the flow cytometer without the use of antibodies was done as presented in Table 7. The difference in fluorescence values between the control cells and the irradiated cells was calculated. It can immediately be observed that the smallest difference between the irradiated sample and the control sample is found in the FL-4 channel. As will be discussed later, the FL-4 channel is connected to a different laser than the other three channels. The largest difference in fluorescence is measured in the FL-3 channel for both experiments. Furthermore, a significant difference is also seen in the FL-1 channel that has been used for calreticulin detection. Consequently, changing the channel that is used to measure calreticulin is something that should be examined in future experiments.

Table 7 The median fluorescence values measured by the different channels for cell samples having received no antibody treatment.

Sample	*FL-1 median value*	*FL-2 median value*	*FL-3 median value*	*FL-4 median value*
Control	6824	3588	12635	985
Irradiated	8588	5355	19979	1119
Difference	1764	1767	7344	**134**
Control	5224	2888	10709	949
Irradiated	7205	4402	17331	1083
Difference	1981	1514	6622	**134**

4.3.5 Autofluorescence and non-specific binding

The results from the x-ray experiments that demonstrated unexpected results (Figure 32) led to the need to investigate the underlying causes. It was speculated that issues concerning high background fluorescence were tampering the credibility of the results – even those that seemed good at first glance. Therefore, three separate experiments were performed at different times – two with the unconjugated antibody and one with the conjugated antibody. Cells having received a dose of 8 Gy of x-rays were used and control cells were either barcoded or left without barcoding in order to rule out spill-over from the barcoding fluorescence into the FL-1 channel. This resulted in three different samples, namely, "irradiated", "C(BC)" and "C(no BC)" respectively. These three samples were each further split into three, so that one batch received no antibody treatment, the second batch received only secondary antibody, and the third batch received full treatment with both antibodies. The results from these tests can be seen in Figure 42-Figure 45. Two separate experiments are displayed in Figure 42 and the same experiments are displayed in Figure 43 but this time

normalized to the control samples without any barcoding. Note that the experiments in Figure 42-Figure 43 were conducted using unconjugated antibody whereas the experiment in Figure 44-Figure 45 was performed using fluorochrome-conjugated antibody.

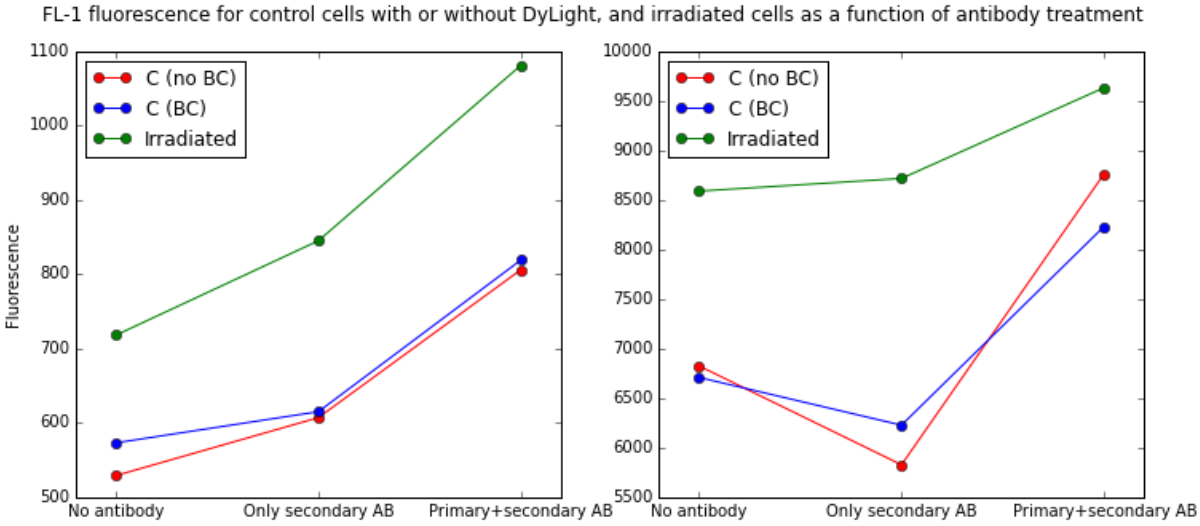

Figure 42 One sample was irradiated with 8 Gy of x-rays 48 hours prior to analysis. Two additional samples were used as control cells, one in which was barcoded (BC) and the other one which was not (C). Each of the three samples was split in two, where one half was kept as is. The other half was further split into two and combined with the other samples. For each original sample, three sub-samples were produced, and these were either treated with no antibody, only secondary antibody or both primary and secondary antibody before analysis by flow cytometry at the Radiumhospital. The fluorescence measured for each original sample was then plotted as a function of the treatments they had received. The left and right panel display two separate experiments.

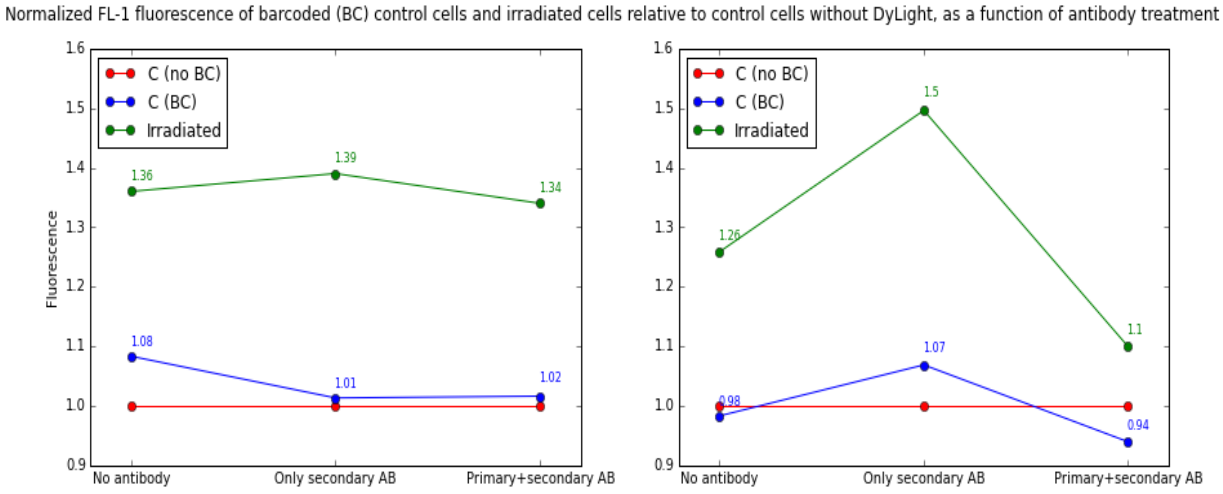

Figure 43 Increase in fluorescence normalized to control sample without barcoding. The left panel corresponds to the data in the left panel of the above plot, and the right panel corresponds to the data in the right panel above.

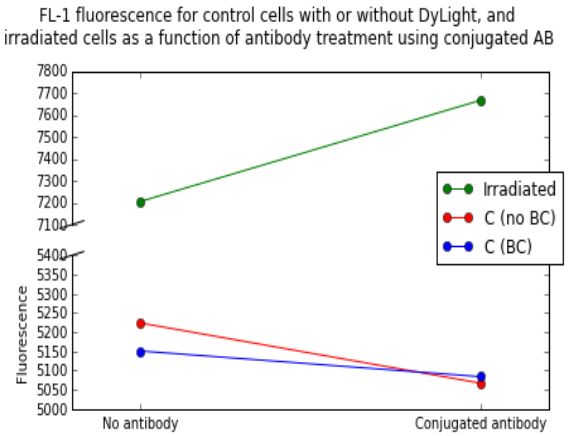

Figure 44 The same test was performed after the purchase of conjugated AB. The fluorescence as a function of treatment is visualized for control cells without BC, control cells with BC or irradiated cells.

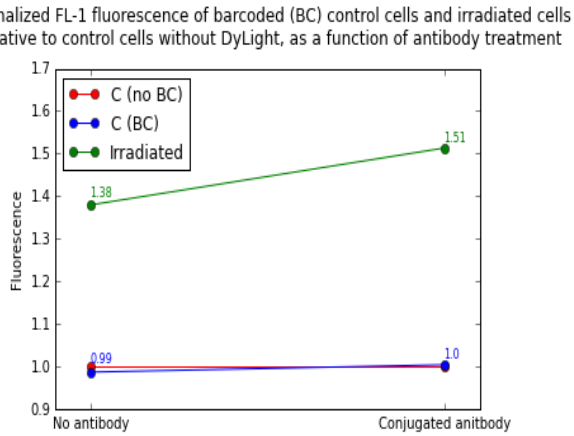

Figure 45 The data displayed corresponds to the data in the left panel but has been normalized to the control sampled without barcoding.

The above tests demonstrate that even without any antibody treatment, there is a significant difference in the measured fluorescence between the irradiated cells and the control cells. This difference ranged between 26-38%. Furthermore, adding only the secondary antibody to the samples generally increased the measured fluorescence. As expected, when the irradiated sample received full treatment of both primary and secondary antibody the highest fluorescence was measured. However, for the two experiments using unconjugated antibodies, full treatment also significantly increased the fluorescence of the control samples. In the right panel of Figure 40, we even observe that the difference in fluorescence between the irradiated sample and both the control samples is smaller with full treatment (primary + secondary antibody) than the difference in fluorescence with no antibody treatment of all. In contrast to this, when using conjugated antibody (Figure 44 and Figure 45), only the fluorescence of the irradiated sample increases when antibody is added. The fluorescence of both control samples stayed stable (or even slightly decreased) when antibody was added. Hence, a signal (fluorescence) was measured in addition to the background signal. The conclusion of these experiments is that only data with the conjugated antibody show more increase in antibody signaling after irradiation than that from unspecific fluorescence. However, in future experiments a sample without antibody should always be included in the analysis.

4.4 Linear regression analysis

The use of bar plots is a display method that can be useful in direct comparison between samples. However, linear regression analysis provides a tool to unmask underlying patterns and dependencies that are not as easily apparent with the use of bar plots. In this section, the proton data has been analyzed in terms of dose- and LET-dependencies. A summary of the statistical results can be seen in Table 8.

Since the previous tests in section 4.3.5 indicated that only the data using conjugated antibody were reliable, this section focuses on the proton data from May for the two cell lines. A linear regression analysis for the remaining proton weeks (November and February) was performed but has therefore been moved to Appendix B.

Table 8 A summary of the statistical results from the Wilcoxon signed-rank test and the linear regression analysis performed on the proton data. The data marked in grey were excluded from further analysis.

Experiment	**Cell line**	**Wilcoxon p-value (irradiated vs. control)**	**Analysis**	**Linear fit**	**p-values (D=dose, L=LET)**	**r^2**	**r^2(adj.)**
February	A549	0.002	Fluorescence vs. Dose	$Y = 55.988x - 19.155$	0.006	0.45	0.41
			Fluorescence vs. LET	$Y = 10.431x + 217.26$	0.122	0.17	0.11
			Fluorescence vs. Dose/LET	$Y = 56.55x_1 + 10.70x_2 - 301.49$	D: 0.002 L: 0.030	0.64	0.58
			Ratio vs. Dose	$Y = 0.085x + 1.025$	0.024	0.33	0.28
			Ratio vs. LET	$Y = 0.012x + 1.474$	0.314	0.08	0.01
			Ratio vs. Dose/LET	$Y = 0.085x_1 + 0.013x_2 + 0.689$	D: 0.022 L: 0.216	0.42	0.32
May	A549	0.003	Fluorescence vs. Dose	$Y = 721.98x + 1974.3$	0.056	0.35	0.28

			Fluorescence vs. LET	$Y = 122.14x + 2238$	0.040	0.39	0.32
			Fluorescence vs. Dose/LET	$Y = 844.87x_1 + 140.91x_2 – 1892.50$	D: 0.0009 L: 0.0007	0.86	0.82
			Ratio vs. Dose	$Y = 0.1454x + 1.422$	0.067	0.33	0.25
			Ratio vs. LET	$Y = 0.0263x + 1.4357$	0.032	0.42	0.35
			Ratio vs. Dose/LET	$Y = 0.172x_1 + 0.030x_2 + 0.597$	D: 0.0009 L: 0.0005	0.86	0.83
May	T98G	0.003	Fluorescence vs. Dose	$Y = 504.62x + 1263.4$	0.03	0.38	0.31
			Fluorescence vs. LET	$Y = 91.517x + 1330.3$	0.02	0.45	0.39
			Fluorescence vs. Dose/LET	$Y = 504.62x_1 + 91.52x_2 – 1024.54$	D: 0.002 L: 0.001	0.82	0.78
			Ratio vs. Dose	$Y = 0.0691x + 1.0575$	0.02	0.42	0.36
			Ratio vs. LET	$Y = 0.0124x + 1.0705$	0.01	0.49	0.44
			Ratio vs. Dose/LET	$Y = 0.069x_1 + 0.012x_2 + 0.748$	D: 0.0001 L: 6.5×10^{-5}	0.91	0.89
February	T98G	0.126	Fluorescence vs. Dose	$Y = -60.25x + 1304$	0.18	0.37	0.14
			Fluorescence vs. LET	$Y = 14.10x + 391.15$	0.30	0.29	0.08
			Fluorescence vs. Dose/LET	$Y = 13.82x_1 - 50.52x_2 + 938.17$	D: 0.18 L: 0.29	0.46	0.21

November	T98G	0.435	Fluorescence vs. Dose	Y = -213.46x + 2453.67	0.26	0.46	0.21
			Fluorescence vs. LET	Y = 44.34x + 111.6	0.25	0.46	0.21
			Fluorescence vs. Dose/LET	$Y = -288.09x_1 + 59.70x_2 + 1450.31$	D: 0.10 L: 0.10	0.75	0.56

4.4.1 The A549 cell line; dose- and LET-dependency from proton experiments performed in May

In the following, the generated scatter plots for each analysis pr. experiment week and cell line are displayed. The raw data from the flow cytometry analysis is found in Appendix A.

The Wilcoxon signed-rank test was first employed to check whether there was a statistically significant difference between the control cells and the proton irradiated samples. A two-tailed test with 0.05 significance level gave a p-value of 0.003. In other words, there is a significant difference between the irradiated samples and the control cells.

With the results from the Wilcoxon signed-rank test a linear regression analysis could be employed. Firstly, the dependency of the measured fluorescence as a function of dose was analyzed, see Figure 46. The lowest median fluorescence value from the FL-1 channel of the control cells population was first identified and subtracted from each of the median values of the irradiated samples. Note that conjugated antibody was only used for the proton data from May.

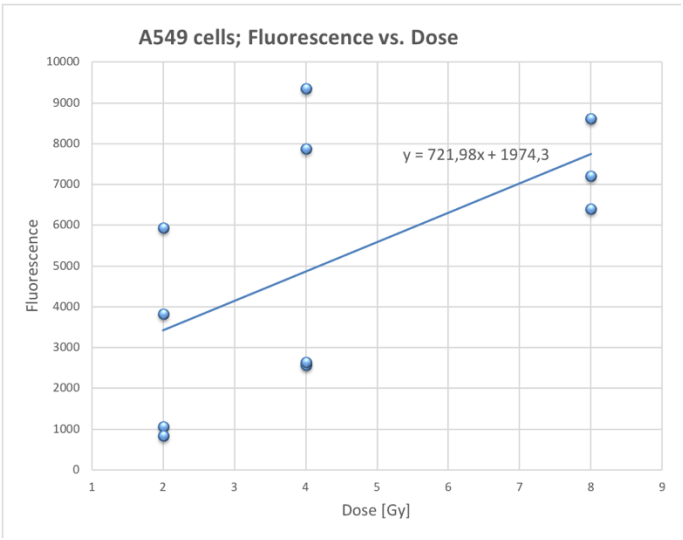

Figure 46 May; fluorescence as a function of dose for A549 cells irradiated with protons. The blue data points represent the irradiated cells The line shows the linear fit of the data points.

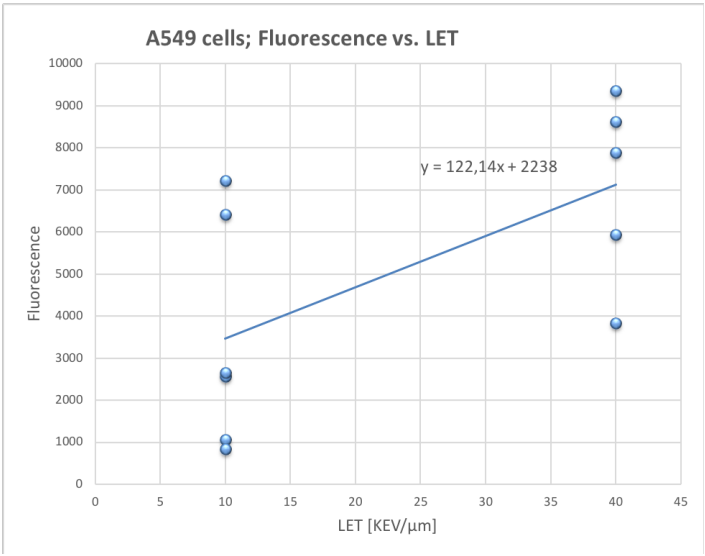

Figure 47 The same data are plotted as fluorescence as a function of LET where low-LET (front of Bragg peak) is assigned a value of 10 whereas the high-LET (back of Bragg peak) is assigned a value of 40.

.

There is a clear appearance of a linear relationship between the fluorescence and the dose. The regression statistics output gives an r^2-value (coefficient of determination) of ~ 0.35 which indicates that a relatively small portion of the variance of the dependent variable around the mean can be explained by the independent variable. Furthermore, the *p-value* of the dose coefficient is ~ 0.056, which falls just outside of the 5% significance level. Clearly, the fluorescence demonstrates a linear dependence of the treatment received but the dose alone is probably not the optimal way to describe the trend.

Next, the LET-dependence was tested. The samples that were irradiated at front of the Bragg peak were assigned a low LET-value of 10, whereas the samples that were irradiated behind the Bragg peak were allocated a LET-value of 40 (Dahle, 2017). The plot can be seen in Figure 47.

The p-value was found to be 0.040 and the r^2 and r^2_{adj}-values were 0.39 and 0.32 respectively. The results were therefore statistically significant, but the *r*-values were still relatively low.

Next, a multivariable regression was performed with two independent variables aiming to describe the dependent variable. This time both dose and LET were used as the independent variables. The results from the multivariable regression gave p-values of 0.0009 and 0.0007 for dose and LET respectively. The r^2-value was 0.86 and r^2_{adj} gave 0.82. Clearly, the

behavior of the median fluorescence values of the irradiated samples is best explained by both dose and LET!

Another way to look at the data is to use the ratios of the irradiated samples against the control samples. In this way, each irradiated sample can be evaluated against its designated control that was measured at the same time during the flow cytometry analysis. The scatter plots for the ratio of fluorescence as a function of dose and as a function of LET can be seen in Figure 48 and Figure 49 respectively.

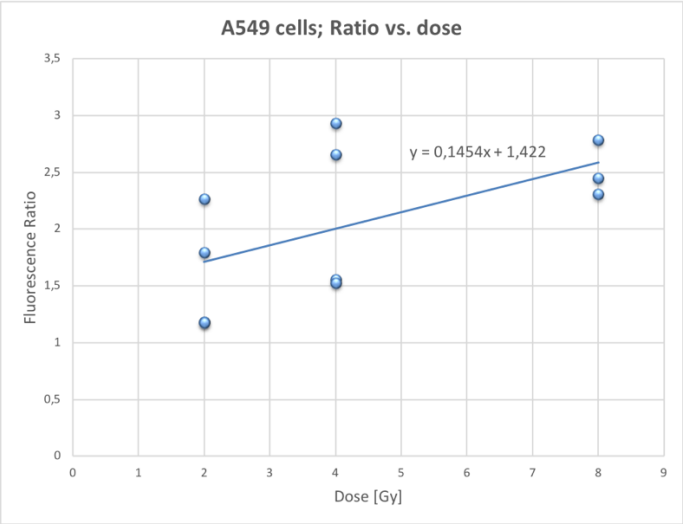

Figure 48 This time the ratio of the fluorescence of the irradiated samples to the control cells are displayed as a function of dose

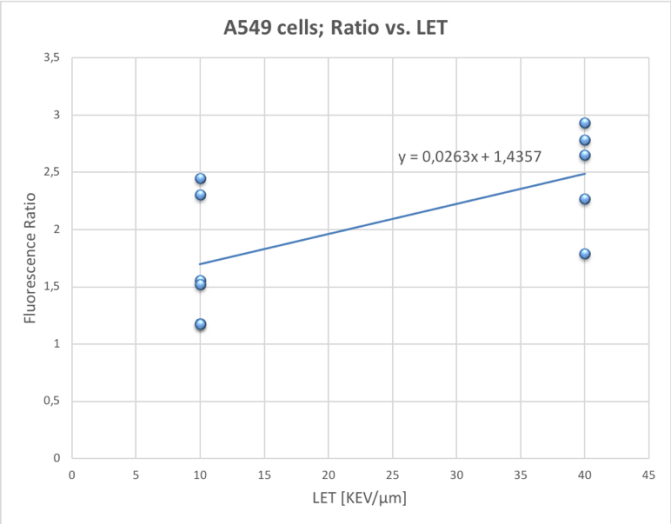

Figure 49 The ratio of the fluorescence of the irradiated samples to the control cells as a function of LET

The linear regression statistics for the ratio of fluorescence of the irradiated samples to control samples gave a p-value of 0.067 when dose was used as the independent variable (not significant). The p-value when LET was used as the independent variable was statistically significant (0.032) with $r^2 \sim 0.42$ and $r^2_{adj} \sim 0.35$.

Again, the statistics were improved when a multivariate analysis of the fluorescence of the ratios as a function of both dose and LET were used. The p-values were 0.0009 and 0.0005 for dose and LET respectively, with $r^2 \sim 0.86$ and $r^2_{adj} \sim 0.83$. These values were very similar to the values obtained from the multivariate analysis above, not using ratios.

4.4.2 The T98G cell line; dose- and LET-dependency from proton experiments performed in May

The T98G cell line was analyzed by linear regression in the same way as the A549 cell line. Note that the following data from May was retrieved using fluorochrome-conjugated antibody for labeling.

The Wilcoxon signed-rank test gave a p-value of 0.003, again implying that there is a statistically significant difference between the irradiated samples and the control cells.

The fluorescence as a function of dose can be seen in Figure 50 and the fluorescence as a function of LET is displayed in Figure 51.

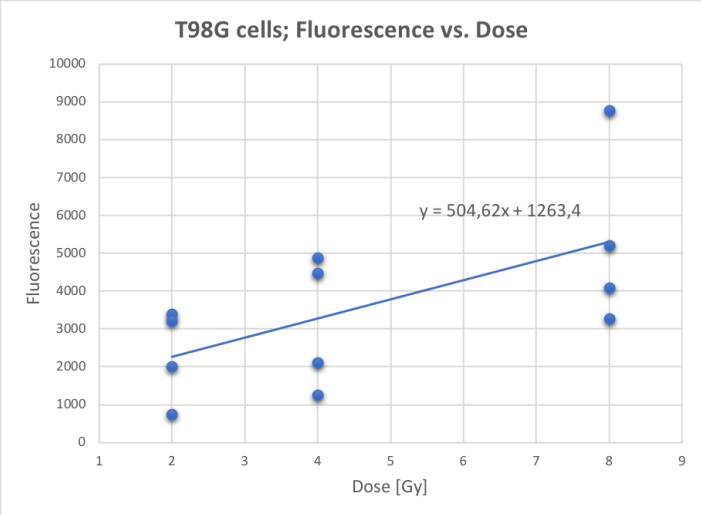

Figure 50 May; fluorescence as a function of dose for T98G cells irradiated with protons. The line shows the linear fit of the data points.

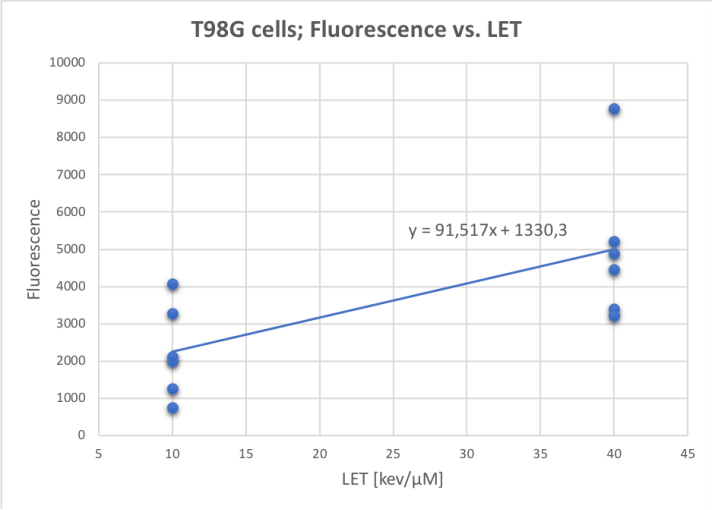

Figure 51 The same data are plotted as fluorescence as a function of LET where low-LET (front of Bragg peak) is assigned a value of 10 whereas the high-LET (back of Bragg peak) is assigned a value of 40.

For the T98G cell line, the statistical output of fluorescence as a function of dose gave a p-value of 0.03. The values of r^2 and r^2_{adj} were 0.38 and 0.31 respectively. The fluorescence as a function of LET gave slightly improved statistical results with a p-value of 0.02, r^2 of 0.45 and r^2_{adj} of 0.39.

Again, the trend was that the multivariate analysis was a better choice to describe the dependencies. The p-values were 0.002 (dose) and 0.001 (LET). r^2 was 0.82 and r^2_{adj} gave 0.78.

The fluorescence of the ratios of the irradiated samples to the control cells were then plotted as a function of dose (Figure 52) and as a function of LET (Figure 53):

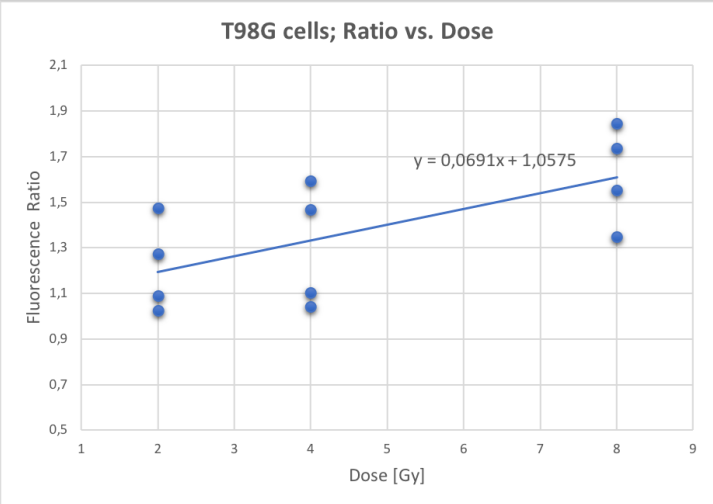

Figure 52 The ratio of the fluorescence of the irradiated samples to the control cells are displayed as a function of dose

Figure 53 The ratio of the fluorescence of the irradiated samples to the control cells as a function of LET

Analysis using the ratios of the irradiated samples to the control cells slightly improved the statistics with a p-value of 0.02 for dose and 0.01 for LET. The r^2 and r^2_{adj} were 0.42 and 0.36 respectively when using dose as the independent variable, and 0.49 and 0.44 when LET was the independent variable.

The multivariate analysis of the ratios for both variables gave the strongest statistics out of all the data analyzed by linear regression. The p-values for dose and LET were 0.0001 and 6.5 x 10^{-5} respectively. The *r^2-value* was 0.91 and the adjusted coefficient of determination, r^2_{adj}, was 0.89.

5 Discussion

5.1 Calreticulin

The initial purpose of this thesis was to examine whether the cell surface-exposed calreticulin in cancer cells could be related to radiation in terms of type (LET) and dose. Several research papers have suggested the role of calreticulin in triggering an immune response in cancer treatment by acting as an 'eat-me' signal (DAMP). However, challenges in characterizing this multi-functional protein include the intrinsic disordered nature of calreticulin in addition to somatic mutations that have been identified along the calreticulin gene in many cancers with the potential effect of creating small differences in the protein activity. In fact, it is argued that it is *"a mistake to consider calreticulin as just one protein"* (Varricchio L., 2017).

However, it became evident fairly quickly during this project that a shift of focus towards protocol optimization was required. Early experiments conducted in the autumn of 2018 showed a range of inconsistencies in the results that questioned the integrity of the protocol used.

5.2 Photon and proton irradiation

5.2.1 Dose dependence

The optimal dose and fractionation regimes in terms of both local tumor control and immune response have been tested widely in a clinical setting. Interestingly, Ko et al. (2018) points out the existence of a threshold dose per fraction *"beyond which radiation becomes less effective in generating tumor immune responses"* (Ko, 2018). In their paper, the authors have reviewed both preclinical and clinical evidence regarding radiotherapy and the dose-fractionation considerations affecting the antitumor immunity. From the preclinical evidence a window of opportunity seems to exist where the optimal regimen in terms of dose and fractionation is a balance between eliciting immunogenic cell death and establishing a tumor microenvironment that is proimmunogenic. For instance, Golden (2014) identified a dose-dependent increase in ATP release, cell surface translocation of calreticulin and HMGP1 release of dying cancer

cells in TSA murine mammary carcinoma cells when receiving single-fraction doses from 2-20 Gy in vitro (Golden, 2014).

Literature using animal models have shown conflicting results in terms of the superiority of a high-dose, single-fraction to a low-dose, multiple-fraction regime in inducing immunogencity. The notion that radiotherapy can induce systemic responses of the immune system is generally based upon the identification of the abscopal effect observed in immune-competent mice. The abscopal effect measured in mouse models usually involves the implant of tumors in both flanks, allowing for irradiation of a single flank and subsequent tracking of tumor response at the untreated region. Whereas some studies found the fractionation approach to generate improved abscopal effect, other studies observed an increased abscopal effect by the use of a high-dose, single-fraction system. The heterogeneity in how these studies have been conducted and the great variety in doses and fractionation pose a challenge as to whether the abscopal effect can be contributed to the total dose, the dose per fraction or to the difference in biological equivalent dose (BED) (Ko, 2018).

These diverse results from literature provided a motivation to study the effect of various doses and fractionations on the cell-surface translocation of calreticulin.

5.2.2 X-rays

Some of the experiments conducted at the start of this thesis seemed promising. Flow cytometry analysis of T98G human glioblastoma cells irradiated with varying doses of x-rays revealed an apparent increase in cell surface calreticulin relative to the unirradiated control cells. Figure 31 shows the results from three separate x-ray experiments. As can be seen, the ratios of fluorescence of the irradiated samples to the control cells appear to show a marked increase in cell surface calreticulin as measured by the FL-1 channel for most of the samples. The samples receiving two fractions of a given dose consistently demonstrate higher fluorescence than the samples only receiving one fraction of the same dose. Furthermore, it can be observed from the mid-panel that there is a larger difference in fluorescence between the irradiated samples versus the control samples for two fractions of 4 Gy compared to one fraction of 8 Gy. This is an interesting observation as despite the fact that the same total dose is given, the two fractions of 4 Gy given in a 24 hour-interval will provide time for the initiation of repair processes, and this seems to result in a larger ratio of fluorescence.

However, the results seemed to vary significantly and isolated experiments using the same cell line and dose would render different results (Figure 32). Initially, it seemed reasonable to assume that the inability to perform the protocol identically for each experiment could impact on the results obtained and that this would become less prominent with more practice. Nonetheless, attempts to reduce the number of cell dishes in each experiment to diminish time and reduce potential errors did not provide more consistencies in the results. Therefore, systematic investigation into the possible weaknesses in the protocol was needed.

5.2.3 Protons

The proton irradiated cells were analyzed in regard to their cell surface calreticulin accumulation by measuring fluorescence in the FL-1 channel as a function of treatment. The fluorescence as a function of treatment and position of the Bragg peak for the two cell lines can be seen in Figure 34, Figure 36 and Figure 38. The ratio of fluorescence from cells irradiated at the back of the Bragg peak versus the cells irradiated at the front of the Bragg peak was calculated and displayed in Figure 35, Figure 37 and Figure 39.

The proton data from November demonstrate a large LET-effect for the T98G cells that received 2 Gy. The cells irradiated at the back of the Bragg peak showed almost five times more fluorescence in the FL-1 channel per cell than the cells irradiated at the front of the Bragg peak. A pattern of such an LET-effect can be seen for most of the samples for all proton experiments. However, a few exceptions exist; for 1 fraction of 8 Gy from November (T98G) and 2 fractions of 8 Gy (T98G, A549) from February no such effect can be seen. Also, for 2 fractions of 4 Gy (T98G, A549) close to no LET-effect can be found. This could reflect a saturation of the signal. Ko et al. (2018) described a threshold dose per fraction in which the tumor immune response decreases beyond such doses. In light of these results, it can be speculated that the saturation reflects actual decrease in calreticulin translocation to the cell membrane, and that other forms of immune-associated responses take over beyond this threshold.

Moreover, there are some similarities and some prominent differences between the two cell lines. First and foremost, the A549 cell lines generally produces a stronger difference between the irradiated cells compared to the control cells. However, especially the data obtained in May show that the amount of fluorescence as a function of the treatment applied demonstrate a pattern that is similar for both cell lines (Figure 38).

Furthermore, if we compare the effective dose and assume that two fractions of 4 Gy renders approximately the same dose as one fraction of 8 Gy for the same radiation type, we observe that the ratio is greater for the two-fraction regime. This holds for the A549 cell line but is not valid for the T98G cell line. Such observations support the concept of a fractionation-effect on the cells. Rubner et al (2014) studied the effects of fractionated radiotherapy (RT) by x-rays in T98G glioblastoma cells. They found that irradiation of 5 x 2 Gy over five consecutive days resulted in an increased number of both apoptotic and necrotic cells compared to single-dose irradiation when analyzed at 48 hours after the last fractionation. They stated that ionizing radiation is known to induce G2-arrest – a mechanism to allow time for repair of sublethal damage. The induction of G2-arrest by RT leaves the cells in a phase highly susceptible to additional radiation doses. The G2-arrest could be seen 4 hours after exposure and lasted at least 48 hours after the last irradiation. Conversely, one single fractionation dose of 10 Gy did not show the same G2-arrest when observed from 4-72 hours post-irradiation (Rubner, 2014). Their findings demonstrate the clinical relevance of the effect of fractionation. They also support the results from the x-ray experiments of this thesis (Figure 31) showing a higher fluorescence of the cells having received two fractions of 4 Gy compared to those cells having received one fraction of 8 Gy. Again, this only holds for the A549 cell line, and x-ray data are only available for the T98G cell line. Consequently, such comparisons are only for observational purposes and only serves to be mentioned as a side note.

When comparing the proton data to the x-ray data for the T98G cell line, it is curious to observe that in this thesis, the fractionation effect behaves contradictory for the two radiation modalities; whereas the x-ray data show that there is a larger accumulation in fluorescence for the fractionated cells compared to the cells receiving the same total dose in only one fraction, the proton data on the other hand, consistently demonstrates less fluorescence accumulation when the cells are subject to fractionation.

Assuming an increased susceptibility to further irradiation after receiving one dose, the increased fluorescence observed in T98G cells with two fractionations of x-rays compared to one fractionation of the same total dose may be a reflection of this susceptibility manifested in an increase in calreticulin translocation to the cell-membrane. Furthermore, Rubner et al argue that fractionated radiotherapy induces a higher abundance of dying cells compared to single-dose radiotherapy, and that this may exhaust the phagocyte system leading to higher amounts

of necrotic cells. They define primary necrotic cells as cells that have full DNA content but have lost their membrane integrity due to high levels of stress. Secondary necrotic cells on the other hand, refers to late apoptotic cells that have degraded the DNA content but have not been properly cleared and therefore lost their membrane integrity. In contrast to primary necrotic cells, secondary necrotic cells have gone through a regulated death path through apoptosis before the occurrence of membrane disintegration.

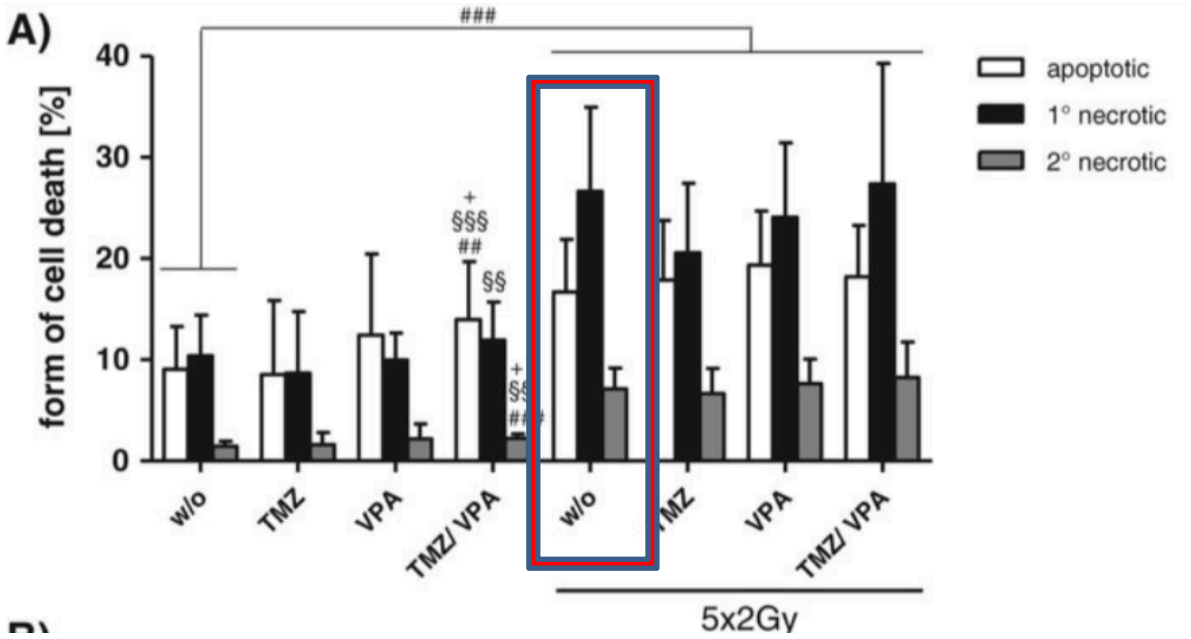

Figure 54 T98G cells given 5 x 2 Gy of x-rays and assessed for percentage forms of cell death at 48 hs post-irradiation (red square). Apoptotic (white bar) refers to cells that have undergone the regular steps involved in apoptotic cell death. Similarily, primary necrotic cells have died a traditional necrotic death having lost their membrane integrity. Secondary necrotic cells refers to cells that are late apoptotic having gone through the same steps involved in apoptotic cell death but that have not been properly cleared in time and therefore have lost their membrane integrity (adapted from (Rubner, 2014).

Figure 54 from (Rubner, 2014) shows that the majority of the T98G cells have died by primary necrosis compared to apoptosis and secondary necrosis when analyzed at 48 hours post-irradiation. Existing literature is divided when it comes to the classification of immunogenic cell death (ICD). The release of calreticulin from the ER has been attributed to immunogenic apoptosis and solely this type of cell death (Inoue, 2014). Apoptosis has traditionally been considered non-immunogenic but there has been increasing evidence that certain chemotherapeutics and RT can induce immune-stimulatory characteristics in apoptotic cells (Zhang, 2018). Other literature describes immunogenic cell death (ICD) as a form of cell death related to necrosis (Portella, 2019). The lack of consistency in literature makes it hard to decide the relevancy of findings such as those of Rubner et al. when it comes to comparing their results to the results of this thesis. However, Rubner et al. found that all three forms of

cell death increased with the fractionation regime and this is in line with the x-ray results of this thesis.

For the proton data another variable is introduced in addition to the fractionation effect; the LET effect. Compared to x-rays, the same dose of protons inflicts a much greater damage to the cells due to the densely ionizing nature of the energy deposition of protons. Consequently, the LET and RBE of protons are much greater than of photons (McKelvey, 2018).

Miszczyk et al compared x-rays to protons and the mechanisms in which they induce different types of cell killing. They irradiated human peripheral blood lymphocytes (HPBL) with 60 MeV protons or 250 kVp x-rays with doses ranging from 0.3 to 4 Gy. The cells were then analyzed 1 and 4 hours after irradiation and visualized by fluorescence microscopy. Generally, they found that proton irradiated cells led to more cell death by necrosis than cells receiving x-rays. Specifically, this difference was more prominent in doses > 1.5 Gy. Interestingly, the percentage of necrotic cells 1 hour post-irradiation was at a maximum for the highest dose (4 Gy). 4 hours after irradiation, the number of necrotic cells peaked at 2.5 Gy (protons) and 2.0 Gy (x-rays) with 48.6 % and 21.9 % respectively. Increasing doses beyond these, led to a decline in necrotic cells for both radiation types which the authors argued may be due to dead cells degradation (Miszczyk, 2018). These observations may suggest that with 4 Gy of proton irradiation the cells die directly by necrosis due to the severe damage inflicted upon the cells, whereas at 2.5 Gy, a larger portion of the cells first enter apoptosis before they proceed to secondary necrosis. Although it remains unclear whether immunogenic cell death can be attributed to apoptosis or necrosis, the findings of Miszczyk et al. can be seen in light of the results of this thesis; the quick necrotic death of cells within a few hours post-irradiation for the higher doses could mean that most of the cells were dead at the time of analysis by flow cytometry. In this way, the cell surface-anchored calreticulin would have been released into the medium, leading to low measurements of calreticulin when the viable portion of the single cells were analyzed. Perhaps is this the cause of the low fluorescence measurements in the T98G cell line for the proton irradiated cells having received doses in two fractions. However, there is vast difference in response to radiation between different cell lines, and the findings of Miszczyk et al. may not be applicable to the cell lines studied in this thesis. Especially glioblastoma cells are known to be highly heterogenous in nature (Riccadonna, 2016), both at the cellular and the molecular level (Inda, 2014).

Irrespective of this, the high density of damage associated with high LET-radiation such as protons compared to photons, and consequently the greater RBE, causes a high generation of cell death at a relatively small area, especially in regard to the cells irradiated at the back of the Bragg peak. This may also have implications for the phagocytic uptake of the portion of the cells dying through immunogenic cell death, leading to saturation with the consequence that other types of mechanisms kick in that are not related to immunogenic cell death. Perhaps is this the explanation to why fractionation causes consistently less fluorescence for the proton-irradiated T98G cell line.

However, the same pattern is not observed for the A549 cell line. In this case, fractionation resulted in the highest fluorescence-ratios for both 4 and 8 Gy. Little literature can be found on the mechanisms of cell death resulting from proton irradiation for this cell line. Narang et al. compared the effects of γ-irradiation (GI) to the effects of proton irradiation (PI) at equitoxic doses assuming an RBE of 1.1. They irradiated A549 cells with 2 Gy (PI) and 2.2 Gy (GI) and measured cell death by apoptosis after 24, 48 and 72 hours post-irradiation. They found that the percentage of apoptosis after 24 and 48 hours were similar for both radiation-types but that the percentage of apoptotic cells was almost double for proton-irradiated cells compared to γ-irradiated cells after 72 hours (Narang, 2015). What these observations imply is that irradiation with protons as opposed to photons causes the greatest damage and subsequent death by apoptosis but that this superiority in apoptosis-induction is not manifested until more than 48 hours post-irradiation. Perhaps is this a characteristic of the A549 cell line – the peak in the percentage of dying cells is delayed by several hours relative to the T98G cell line. As a result, at the time of analysis by flow cytometry, these cells will still have an intact membrane and more membrane-bound calreticulin can be measured compared to the T98G cell line.

Evidently, there are inconsistencies in the results obtained, and it was necessary to investigate the protocol used in the detection of membrane-bound calreticulin exposure and attempt to optimize the assay further.

5.3 Protocol investigations and tests

5.3.1 Barcoding incubation time

Due to differences in number of cell dishes in each experiment, the incubation time of control cells stained with DyLight used for barcoding could vary. Although the incubation time was never less than 30 minutes the duration could be extended to over an hour, especially during proton irradiation weeks that required a large number of cell dishes to be included in each experiment. The impact of this variation in incubation time between experiments was therefore investigated by comparing cells irradiated with 8 Gy of x-rays and then barcoded with an incubation time of 30 minutes or 3 hours. The results were found by comparison of samples with different incubation times from the same experiment and showed that the incubation time did not have any significant impact on the fluorescence measured by flow cytometry with only 1.8% difference in fluorescence between the two samples.

5.3.2 Cell confluency

The population density of proliferating cultured cells will change over time. Such variations in density will have implications on physiological, morphological and biochemical conditions. Trajkovic et al. (2019) studied the variation in protein markers within the cell in relation to the fluctuations in cell density. They found that the expression levels of several of these proteins were affected under highly confluent cell conditions due to starvation of nutrients and cell crowding. Furthermore, they looked at how cell density affects experimental outcomes when using agents that, as a side effect, alters the confluency of a cell culture. To assess this effect, they compared control cells to cells treated with the density-changing agents by doing a density matching. As hypothesized, the results recorded for the different cell density-sensitive proteins (pS6, p62 and Lamp1) were dependent on the controls used. In conclusion, density variations were found to influence the experimental outcomes, and density-matching the controls (similar endpoint density) was suggested to reduce noise. However, the levels of the endoplasmic reticulum located protein *calnexin* remained stable throughout the different cell density tests (Trajkovic, 2019). Calnexin and calreticulin are both chaperones located in the ER and are involved in protein folding and the quality control of proteins. Calnexin is a lectin chaperone whereas calreticulin is a lectin-like chaperone and in contrast to calnexin, calreticulin can also be found in the extracellular matrix and on the cell

surface (Huang, 2016). Other than that, calnexin and calreticulin are related chaperones performing many overlapping functions. In light of the results detected by Trajkovic et al. and the similarities between calnexin and calreticulin, it is reasonable to assume that cell density variations will not influence significantly on the results in our experiments. For the most part, the confluency of the irradiated cells in all experiments was ~80% as estimated by eye measurement in the microscope prior to analysis.

5.3.3 Titration

After the purchase of the conjugated AB, a dilution test (titration) was performed to determine the optimal concentration of antibody/BSA-PBS in order to reduce the non-specific antibody binding. This optimal concentration should maximize the signal of the positive population and minimize the signal of the negative population (Hulspas, 2009). The results of the dilution test can be seen in Figure 41. Although the difference in fluorescence between the irradiated sample and the control was greatest for the lowest dilution (1:100), a dilution of 1:250 was chosen for further experiments as this dilution rendered the lowest signal for the unirradiated control cells.

5.3.4 Flow cytometer at the Radium hospital

Since service had to be performed on the flow cytometer Accuri C6 at The Department of Biophysics at UiO, which required the machine to be sent out of country, some of the experiments were partially conducted at Forskningsbygget at the Radium hospital (Figure 31, lower panel and Figure 42). Specifically, the calreticulin assay was performed as normal at UiO but the flow cytometry analysis was carried out at the Flow Cytometry Core Facilities at Oslo University Hospital (OUS). The cells were then transported to OUS on ice and propidium iodine (PI) was added approximately five minutes prior to the flow cytometry analysis. Despite the inconveniency of not being able to perform the flow cytometry analysis at UiO for a few weeks, the advantage lay in the opportunity to perform analysis at a facility with high quality and with the help of dedicated staff to ensure the analysis was performed correctly. This reduced the possibility that any inaccuracy related to the flow cytometer at UiO would influence the results obtained.

5.3.5 Fixation

Since the experiments concerned live cells and the point was to look at membrane-bound calreticulin accumulation, no fixation or permeabilization steps were included in the protocol for calreticulin detection. Permeabilization would almost certainly have caused leakage of calreticulin from the inside to the outside of the cell, which would undermine the purpose of the experiment. Interestingly, Osman et al. (2017) used a 7 minutes fixation step with 4% paraformaldehyde (PFA) in their experiments when they investigated ecto-calreticulin (cell surface anchored CRT) in JurkaT cells. They irradiated the cells with UVB and found a significant increase in cell-surface calreticulin 30 minutes after irradiation by flow cytometry. Additionally, they measured extracellular calreticulin by conditioning RPMI medium without serum with JurkaT cells, both treated and untreated, and analyzed the supernatant recovered after 30 or 120 minutes for calreticulin by western blotting. Curiously, they detected calreticulin in the cell medium (supernatant) even for the untreated cells. For the UVB-irradiated cells, the cell medium detection demonstrated a reduction in medium-released calreticulin compared to the control cells 30 minutes post-irradiation, and then a clear upregulation of calreticulin at 120 minutes. In light of their other results that showed the highest upregulation of membrane-bound (ecto-) calreticulin analyzed at 30 min after irradiation compared to both cells recovered at 120 min and untreated control cells, they concluded that there is an early accumulation of ecto-calreticulin in pre-apoptotic cells followed by a release of calreticulin into the medium (Osman, 2017).

In the present experiments there was an increase in the fluorescence signal in irradiated cells compared to control cells even without any primary antibody added (see section 4.3.5). Since this was never observed in fixated cells used for other types of experiments, it was hypothesized that the signal was connected to the cells not being fixated. A fixation test was therefore performed to see the impact of fixation on the results compared to the results were no fixation was used. In accordance with Osman et al., no permeabilization was performed. The cells were irradiated with 8 Gy of x-rays and fixated with 1% formaldehyde for five minutes prior to flow cytometry analysis. The results can be seen in Figure 40. The same data are displayed in both plots. The left panel shows the differences between irradiated and unirradiated cells as a function of treatment (antibody/no antibody, fixation/no fixation) and the right panel compares the cells that were fixated to those who were not fixated as a function of treatment (antibody/no antibody, irradiated/not irradiated). The results

demonstrated a relatively small difference in fluorescence between the fixated and non-fixated cells. Generally, fixation seemed to reduce the median fluorescence by a small percentage (up to 15%) for both the irradiated cells and the control cells but the reduction was greatest for the irradiated cells. However, the fixation test still confirmed the earlier observations that even when no antibody was added, the fluorescence of the irradiated cells was higher than the unirradiated control cells. The advantage of fixation was therefore dismissed and not used in any further experiments.

5.3.6 Non-specific antibody binding

Early experiments using a primary and a secondary antibody (also referred to as unconjugated antibodies) showed variations in the fluorescence levels detected. For every experiment each irradiated sample was split into two, where one part was treated with both primary and secondary antibody and the other part was treated with only secondary antibody to provide a reference point for the levels of non-specific binding. Figure 42 shows that despite the sample treated with both antibodies generally demonstrated the highest levels of fluorescence, the sample treated with only secondary antibody also showed a somewhat upregulated level of fluorescence after irradiation (left panel). It was speculated that the secondary antibody was binding non-specifically - a term concerning the *"binding of an antibody to a different epitope than one it was generated against"* (Hulspas, 2009). Despite always blocking with BSA during incubation, this remained a concern throughout the experiments using unconjugated antibodies. The right panel (Figure 42) shows the results from of the same type of test but in a separate experiment. This time the cells treated with only secondary antibody showed a downregulation in fluorescence compared to the cells not treated with any antibody. Clearly, there are variations in the fluorescence across experiments despite the same experimental layout.

To overcome the uncertainty related to any non-specific binding of the secondary antibody, a fluorochrome-conjugated antibody was purchased and used for the later experiments.

Although non-specific binding is usually the main concern in assays using antibodies, it should be pointed out that specific binding can also be undesirable. I.e. different antigens can share the same epitope leading to cross-reactivity and specific, but undesirable, binding (Hulspas, 2009).

5.3.7 Autofluorescence

The ongoing quest for eliminating factors that contributed to unreliable results led to a need to investigate the autofluorescence of the cell line. The tests that can be seen in Figure 42 were performed for both fluorochrome-conjugated and unconjugated antibody. It became apparent that even when no antibody was added to the sample, significant fluorescence was detected in the FL-1 channel and the irradiated sample showed a higher fluorescence than both the untreated samples. The barcoded control and the control that had received no barcoding did not vary significantly from each other, but they both showed an increase in fluorescence when antibody was added. The increase in fluorescence when only secondary antibody was added for all three samples is likely to be due to non-specific binding of the secondary antibody. Furthermore, the increase can also be caused by an increase in autofluorescence caused by the treatment itself.

Challenges with autofluorescence in flow cytometry can lead to serious misinterpretation of results if not accounted for. In their paper "Cellular Autofluorescence following Ionizing Radiation", Schaue et al. (2012) investigated several human and murine cell types and their response to ionizing radiation in terms of autofluorescence. The irradiation was performed with an x-ray unit at various doses and the cells were analyzed by flow cytometry (FACS) without adding any external markers (fluorophores). They found a marked rise in autofluorescence in relation to dose and time for 13 of the 14 cell types investigated, the only exception being erythrocytes. Generally, the more radiosensitive the cell type, the higher the autofluorescence (immune cells), whereas more radioresistant cell types such as PC3 prostate cancer and U87 glioma cancer showed a lesser degree of autofluorescence response (Figure 55). Excluding dead cells did not show much impact on the autofluorescence. Of special interest for this thesis is the results regarding the U87 cell line which is a human glioblastoma cancer type – similar to the T98G cell line. In their attempt to explain the increase in fluorescence measured by the FL-1 channel they investigated the FAD and NADH levels of DC2.4 (mouse dendritic cells). FAD (flavin nucleotide cofactor) is a metabolite and is known to have the highest likelihood of being excited by the 488 nm laser with the subsequent emission of green light (Benson, 1979). On the other hand, NADH (the reduced nicotinamide adenine dinucleotide) has a much higher abundancy in cells and is considered the main source of autofluorescence. Schaue et al. (2012) showed that the level of NADH on a per cell basis consistently rose for every cell line following irradiation with 10 Gy – the only exception

again being erythrocytes. However, the excitation/emission peaks of NADH are found at 340/465 nm (Patterson, 2000), and NADH is therefore assumed to not be directly causing the fluorescence in FL-1. On the other hand, Schaue et al. point out that there is an intimate link between FAD/NADH and that a rise in fluorescence of one corresponds to a rise of the other. To increase the understanding of the cellular mechanism behind the autofluorescence behavior observed, they compared U87 parental cells and U87Rho(0) cells stripped of mitochondria. By direct comparison, U87Rho(0) cells showed a higher baseline NADH and autofluorescence but the increase in the two when given 10 Gy was smaller than that of the parental U87. Mitochondrial function and calcium flux are sophisticatedly linked to FAD/NADH homeostasis and they concluded that the dose-dependent relationship between irradiation and autofluorescence could be attributed to variations in metabolism and cell morphology. In summary, they propose that the observed phenomena reflect a common cellular response to radiation in the cell lines investigated (Schaue, 2012).

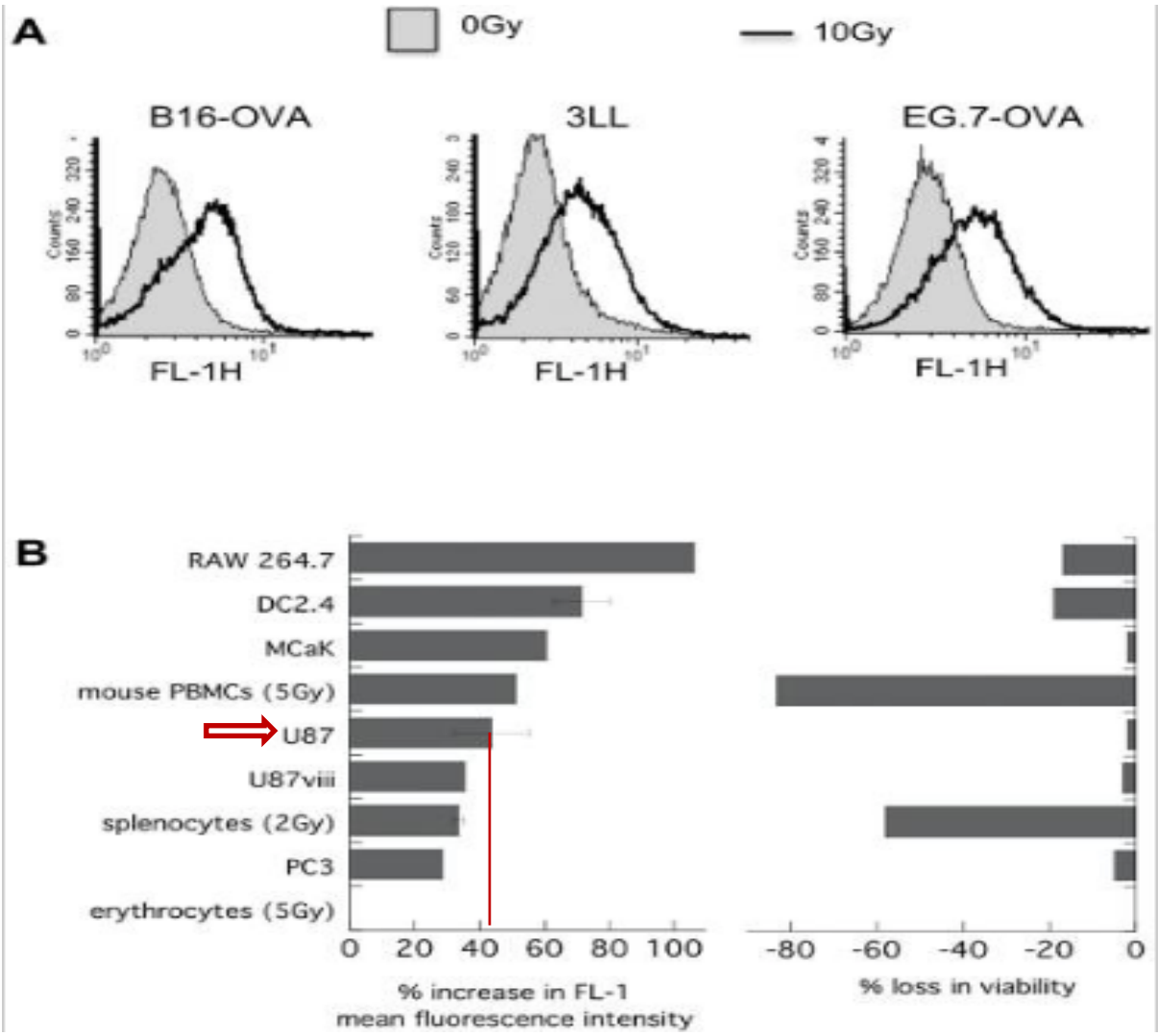

Figure 55 Raise in autofluorescence as a response to radiation; A variety of murine and human cell lines given 10 Gy (or as indicated). Analysis at 24 hours post-irradiation by FACS, FL-1 and viability assessed. A: B16-OVA (murine melanoma), 3LL (lewis lung carcinoma) and EG.7-OVA (murine lymphoma) all demonstrated an increase in autofluorescence for treated vs. untreated cells. B: all cell types except erythrocytes showed a percent increase in mean fluorescence compared to the control and loss of viability. The added red arrow and lines highlight the U87 glioma line (Schaue, 2012)

As seen in Figure 55 the percentage increase in FL-1 mean fluorescence intensity is approximately 40% for the U87 glioma cell line after receiving 10 Gy. This is comparable to the data found in the tests done for this paper (Figure 43, Figure 45 and left in Figure 40). Although Schaue et al. found a somewhat higher mean intensity, this could be attributed to the higher dose (10 Gy) used in their experiments compared to 8 Gy which was used for the experiments of this thesis.

What these tests demonstrate is that due to the increase in fluorescence of the control cells when treated with antibodies, we cannot say that the signal we measure throughout the experiments is due to membrane-bound calreticulin accumulation. This is true for all

experiments using unconjugated antibodies. However, the same test using fluorochrome-conjugated antibody (Figure 45) shows that the measured fluorescence of both control cells stays flat (or slightly decreases) when antibody is added, whereas the fluorescence of the irradiated sample increases. It should be noted that these tests were only performed using x-ray irradiation. The experiment should be repeated with protons, and all future experiments should include a sample analyzed without antibody. However, the result indicate that the use of fluorochrome-conjugated antibody reduces the artefacts from background signaling.

5.3.8 Calreticulin fluorochromes channel

Throughout all experiments the fluorochrome Alexa Fluor 488 has been used. The excitation and emission are subsequently analyzed in the FL-1 channel at the Accuri C6 flow cytometer. This fluorochrome, whether conjugated or unconjugated, is used extensively in literature. However, in light of the results obtained demonstrating a treatment dependence of FL-1 fluorescence even without the presence of any fluorochromes (antibodies), the integrity of the FL-1 channel as a measure of fluorescence in calreticulin-detection must be questioned. This is also supported by the previously mentioned work of Schaue et al. which showed that FAD showed a high likelihood of being excited by the 488 nm laser contributing to fluorescence in the green light spectrum. Little other literature has been found investigating this phenomenon. Furthermore, the presence of any spectral overlap in the fluorescence of the control samples and the irradiated samples could lead to false results. Table 7 shows the raw data (median fluorescence values) obtained by flow cytometry for two of the tests using no antibody to label the cells. The measured median fluorescence for all the four channels is displayed and the difference in these values between the irradiated samples and the control cells are calculated. The channels FL-1, FL-2 and FL-3 all measure fluorescence from excitation by a 488 nm laser, while the FL-4 channel measures fluorescence from excitation with a different laser (640 nm). It is seen in Table 7 that the difference between the irradiated samples and the control cells is much smaller for FL-4. This is in agreement with the hypothesis proposed by Schaue et al. It would therefore be a natural next step to test the use of a fluorochrome excited by the 640 nm laser and emitting in channel FL-4 as discussed in section 4.3.4.

5.4 Linear regression analysis

Overall, the linear regression analysis demonstrated that dependencies can be found throughout both cell lines, and that the measured median fluorescence of each cell sample displays dose- and LET-dependencies to various degrees. Generally, the A549 cell line demonstrated more consistent dependencies than the T98G cell line across both proton experiment weeks (February/May). When the fluorescence of the irradiated cells to the control cells were analyzed as a function of both dose and LET, the results were always significant for the A549 cell line. For the T98G cell line on the other hand, only the samples from the experiment conducted in May were statistically significant in terms of fluorescence vs. dose and LET. Note that this implies that both cell lines demonstrated the strongest dependencies during the proton experiment where the fluorochrome-conjugated antibody was used. In agreement with the experiments measuring the fluorescence without any antibody added, there is a clear trend that the fluorochrome-conjugated antibody generates the most reliable results in terms of calreticulin detection.

It seems tempting to conclude that the fluorescence of the two cell lines demonstrate dose- and LET-dependencies to various degrees. However, several factors must be considered before jumping to conclusions. For instance, due to constraints in the number of samples that could be processed within each proton experiment and further loss of samples due to fungus, aspiration etc., the linear regression analysis would be much more reliable if larger sample sizes were used. Furthermore, the availability of the cyclotron was restricted and only three proton experiments were conducted. Ideally, this number should be increased to improve the statistical relevancy of the analysis. Also, different dose regimes were conducted across these experiments. Any future experiment should settle on a standard dose regime to be followed throughout all experiments.

Nevertheless, the linear regression analysis has proven to be an aid in unmasking the underlying patterns that were not obvious when the data were displayed in bar plots.

5.5 Future perspectives and recommendations

The results obtained during this thesis have not been as straight-forward as anticipated when the experiments started. Varying and unreliable results led to a need to investigate the protocol used for calreticulin detection in detail.

Generally, the A549 cell line has demonstrated to be more promising when investigating membrane-bound calreticulin. It is therefore recommended to investigate this cell line further in any future experiments. X-ray data using this cell line were not retrieved during this work. For that reason, measurements of calreticulin after receiving doses of x-rays should be obtained in order to compare the results to those from proton irradiation experiments. Additionally, it might be of interest to look at other tumor cell lines and their behavior in terms of calreticulin accumulation on the cell surface as a function of dose and LET.

A good starting point for future experiments is to do a test comparing the fluorescence of control cells and irradiated cells with and without antibody treatment using proton irradiation. The results of this thesis imply that the fluorochrome-conjugated antibody should be the antibody of choice.

Furthermore, it is recommended to look at the possibility of changing the channel of the flow cytometer measuring calreticulin. It was clear from the results obtained during this work that the FL-4 channel gave the smallest difference in fluorescence between the irradiated and the control sample when no antibody was used. This channel is excited by another laser than the FL-1 channel, which might be more appropriate to reduce the amount of background signal.

The analysis performed during this thesis was consistently done at 48 hours post-irradiation. Performing the analysis at different time points is recommended to see if this has any implications on the results. As previously mentioned, literature has demonstrated that the form of cell death that dominates may vary as a function of time post-irradiation.

Lastly, it might be interesting to add confocal microscopy to the analysis, to get a visual representation of the distribution of calreticulin. By comparing such images to the results from flow cytometry, a better understanding of whether it is in fact membrane-bound calreticulin that is measured can be obtained.

6 Conclusion

This thesis aimed to measure membrane-bound calreticulin in T98G cells and A549 cells as a function of dose and LET.

An experimental protocol was obtained from collaborators, but it was discovered that a background signal made large contributions to the fluorescence detected and that this background signal was increased by irradiation. This questioned the integrity of the results to such a degree that it could not be concluded that it was calreticulin that was being measured. A lot of effort was therefore put into identification of artefacts and optimization of the protocol.

A change of antibody to a fluorochrome-conjugated antibody finally appeared to improve the reliability of the results even though there still was a problem with background fluorescence. Consequently, only the proton data obtained in May are trusted to generate reliable results.

The conclusions from the data from May are:

A549 cells were found to generally have a stronger membrane-bound calreticulin signal response to irradiation than T98G cells.

When the data were analyzed by linear regression, statistically significant dose- and LET-dependencies were found for both T98G and A549 cells.

The multivariate regression gave even stronger correlations, indicating that the measured fluorescence was dependent on both dose and LET.

References

ADAN, A., ALIZADA, G., KIRAZ, Y., BARAN, Y. & NALBANT, A. 2016. Flow cytometry: basic principles and applications. *Critical Reviews in Biotechnology*.

ALBERTS, B. 2015. *Molecular Biology of the Cell,* New York, US, Garland Science, Taylor & Francis Group.

ATTIX, F. H. 1986. *Introduction to radiological physics and radiation dosimetry,* New York, Wiley.

BENSON, R. C., MEYER, R. A., ZARUBA, M. E. & MCKHANN, G. M. 1979. Cellular autofluorescence--is it due to flavins? *Journal of Histochemistry & Cytochemistry,* 27**,** 44-48.

BIOSCIENCES, B. 2013. BD Accuri C6 Cytometer.

BURMA, S., CHEN, B. P., MURPHY, M., KURIMASA, A. & CHEN, D. J. 2001. ATM phosphorylates histone H2AX in response to DNA double-strand breaks. *J Biol Chem,* 276**,** 42462-7.

BURNET, F. M. 1970. The concept of immunological surveillance. *Prog Exp Tumor Res,* 13**,** 1-27.

CHAO, M. P. E. A. 2014. Calreticulin is the dominant pro-phagocytic signal on multiple human cancers and is counterbalanced by CD47. *Sci Transl. Med.,* 2.

DAHLE, T. J., RYKKELID, A. M., STOKKEVÅG, C. H., MAIRANI, A., GÖRGEN, A., EDIN, N. J., RØRVIK, E., FJÆRA, L. F., MALINEN, E. & YTRE-HAUGE, K. S. 2017. Monte Carlo simulations of a low energy proton beamline for radiobiological experiments. *Acta Oncologica,* 56**,** 779-786.

DI MARTINO, S., CRESCENTE, G., DE LUCIA, V., DI PAOLO, M., MAROTTA, G., DE LUCIA, D. & ABBADESSA, A. 2017. The emerging role of calreticulin in cancer cells. *World Cancer Research Journal* 4.

DUNN, G. P., BRUCE, A. T., IKEDA, H., OLD, L. J. & SCHREIBER, R. D. 2002. Cancer immunoediting: from immunosurveillance to tumor escape. *Nature Immunology,* 3**,** 991-998.

GAFCHROMIC 2014. Gafchromic EBT3 Scan Handling Guide. 12/14 edt. ed.

GAMEIRO, S., ET AL. 2016. Tumor Cells Surviving Exposure to Proton or Photon Radiation Share a Common Immunogenic Modulation Signature, Rendering Them More Sensitive to T Cell-Mediated Killing. *International Journal of Radiation Oncology*Biology*Physics,* 95.

GARG, A. D., DUDEK-PERIC, A. M., ROMANO, E. & AGOSTINIS, P. 2015. Immunogenic cell death. *Int. J. Dev. Biol,* 59**,** 131-140.

GEIGER, H. M., E. 1909. On a Diffuse Reflection of the α-Particles. *Proc. Roy. Soc.,* 82**,** 495-500.

GOLDEN, E. B., FRANCES, D., PELLICCIOTTA, I., DEMARIA, S., BARCELLOS-HOFF. M. H. & FORMENTI, S. C. 2014. Radiation fosters dose-dependent and chemotherapy-induced immunogenic cell death. *Oncoimmunology,* 3.

HALL, E. J. 2012. Radiobiology for the radiologist.

HARRIS, C. R., & SMITH, J. M. 1975. Radiotoxicity of Intracellular 67Ga, 125I and 3H AU *International Journal of Radiation Biology and Related Studies in Physics, Chemistry and Medicine,* 28**,** 225-241.
HOFER, K. G., KEOUGH, G. & SMITH, J. M. 1978. Biological toxicity of Auger emitters: Molecular fragmentation versus electron irradiation. 12**,** 335-54.
HUANG, Y., HUI, K., JIN, M., YIN, S., WANG, W. & REN, Q 2016. Two endoplasmic reticulum proteins (calnexin and calreticulin) are involved in innate immunity in Chinese mitten crab (Eriocheir sinensis). *Scientific Reports,* 6**,** 27578.
HULSPAS, R., O'GORMAN, M. R. G., WOOD, B. L., GRATAMA, J. W., SUTHERLAND, D. R. 2009. Considerations for the control of background fluorescence in clinical flow cytometry. *Cytometry Part B: Clinical Cytometry,* 76B**,** 355-364.
INDA, M. M., BONAVIA, R., & SEOANE, J. 2014. Glioblastoma multiforme: a look inside its heterogeneous nature. *Cancers,* 6**,** 226-239.
INOUE, H., & TANI, K. 2014. Multimodal immunogenic cancer cell death as a consequence of anticancer cytotoxic treatments. *Cell death and differentiation,* 21**,** 39-29.
KAPLAN, H. S. M., L. E. 1964. Biological Complexity and Radiosensitivity. Radiation lethality in cells and viruses is correlated with nucleic acid content, structure, and ploidy. *Science,* 145**,** 21-25.
KEPP, O. E. A. 2014. Consensus guidelines for the detection of immunogenic cell death. *Oncoimmunology,* 3.
KO, E. C., BENJAMIN, K. T., & FORMENTI, S. C. 2018. Generating antitumor immunity by targeted radiation therapy: Role of dose and fractionation. *Advances in radiation oncology,* 3**,** 486-493.
LU, Y. C., WENG, W. C & LEE, H. 2015. Functional Roles of Calreticulin in Cancer Biology. *BioMed Research International,* 2015**,** 9.
MALAMAS, A. S., GAMEIRO, S. R., KNUDSON, K. M. & HODGE, J. W. 2016. Sublethal exposure to alpha radiation (223Ra dichloride) enhances various carcinomas' sensitivity to lysis by antigen- specific cytotoxic T lymphocytes through calreticulin-mediated immunogenic modulation. *Oncotarget,* 7**,** 86937–86947.
MATZINGER, P. 1994. Tolerance, Danger, and the Extended Family. *Annual Review of Immunology,* 12**,** 991-1045.
MAYLES, P., NAHUM, A., ROSENWALD, J. C. 2007. *Handbook of Radiotherapy Physics, Theory and Practice*, Taylor & Francis Group, LLC.
MCKELVEY, K. J., HUDSON, A. L., BACK, M., EADE, T., & DIAKOS, C. I. 2018. Radiation, inflammation and the immune response in cancer. *Mammalian genome : official journal of the International Mammalian Genome Society,,* 29**,** 843-865.
MISZCZYK, J., RAWOJĆ, K., PANEK, A., BORKOWSKA, A., PRASANNA, P. G. S. , AHMED, M. M., SWAKOŃ, J. & GAŁAŚ, A. 2018. Do protons and X-rays induce cell-killing in human peripheral blood lymphocytes by different mechanisms? *Clinical and translational radiation oncology,,* 9**,** 23-29.
NAHM, F. S. 2016. Nonparametric statistical tests for the continuous data: the basic concept and the practical use. *Korean journal of anesthesiology,* 69**,** 8–14.
NARANG, H., KUMAR, A., BHAT, N., PANDEY, B. N. & GHOSH, A. 2015. Effect of proton and gamma irradiation on human lung carcinoma cells: Gene expression, cell cycle, cell death, epithelial–mesenchymal transition and cancer-stem cell trait as biological end points. *Mutation Research/Fundamental and Molecular Mechanisms of Mutagenesis,* 780**,** 35-46.
OSMAN, R., TACNET-DELORME, P., KLEMAN, J.-P., MILLET, A. & FRACHET, P. 2017. Calreticulin Release at an Early Stage of Death Modulates the Clearance by Macrophages of Apoptotic Cells. *Frontiers in Immunology,* 8**,** 1034.

OSTWALD, T. J. M., D. H. 1974. Isolation of a high affinity calcium-binding protein for sarcoplasmic reticulum. *Journal of Biological Chemistry,* 249**,** 974-979.
PATTERSON, G. H., KNOBEL, S. M., ARKHAMMAR, P., THASTRUP, O., & PISTON, D. W. 2000. Separation of the glucose-stimulated cytoplasmic and mitochondrial NAD(P)H responses in pancreatic islet beta cells. *Proceedings of the National Academy of Sciences of the United States of America,* 97**,** 5203-5207.
PINTO, D. M. S. F., A. 2010. Structure and Function of Histone H2AX. *Genome Stability and Human Diseases***,** 55-78.
PODGORSAK, E. B. 2010. *Radiation Physics for Medical Physicists, Biomedical Engineering,* Berlin, Springer-Verlag.
PORTELLA, L. S., S. 2019. Ionizing radiation effects on the tumor microenvironment. *Seminars in Oncology,* 46**,** 254-260.
PRADEU, T. C., E. L. 2012. The danger theory: 20 years later. *Frontiers in Immunology,* 3**,** 1-9.
RICCADONNA, C. E. A. 2016. Decitabine Treatment of Glioma-Initiating Cells Enhances Immune Recognition and Killing. *PLOS ONE,* 11.
ROGAKOU, E. P., PILCH, D. R., ORR, A. H., IVANOVA, V. S. & BONNER, W. M. 1998. DNA double-stranded breaks induce histone H2AX phosphorylation on serine 139. *J Biol Chem,* 273**,** 5858-68.
RÖNTGEN, W. C. 1895. Über eine neue Art von Strahlen. Vorläufige Mitteilung. *Aus den Sitzungsberichten der Würzburger Physik.-medic. Gesellschaft Würzburg***,** 137-147.
RUBNER, Y. E. A. 2014. Fractionated radiotherapy is the main stimulus for the induction of cell death and of Hsp70 release of p53 mutated glioblastoma cell lines. *Radiation Oncology,* 9**,** 89.
SCHAUE, D., RATIKAN, J. A., & IWAMOTO, K. S. 2012. Cellular autofluorescence following ionizing radiation. . *PLoS one,* 7**,** e32062.
SCHNEIDER, A., HOMMEL, G., & BLETTNER, M. 2010. Linear regression analysis: part 14 of a series on evaluation of scientific publications. *Deutsches Arzteblatt international,* 107.
SHOWALTER, A., LIMAYE, A., OYER, J. L., IGARASHI, R., KITTIPATARIN, C., COPIK, A. J. & KHALED, A. R. 2017. Cytokines in immunogenic cell death: Applications for cancer immunotherapy. *Cytokine 97***,** 123-132.
SMITH, M. J., & KOCH, G. L. 1989. Multiple zones in the sequence of calreticulin (CRP55, calregulin, HACBP), a major calcium binding ER/SR protein. *EMBO journal* 8**,** 3581-3586.
TORMOEN, G. W., CRITTENDEN, M. R., & GOUGH, M. J. 2018. Role of the immunosuppressive microenvironment in immunotherapy. *Advances in radiation oncology,* 3**,** 520-526.
TRAJKOVIC, K., VALDEZ, C., YSSELSTEIN, D., & KRAINC, D. 2019. Fluctuations in cell density alter protein markers of multiple cellular compartments, confounding experimental outcomes. *PLoS one,* 14.
VARRICCHIO L., E. A. 2017. Calreticulin: Challenges Posed by the Intrinsically Disordered Nature of Calreticulin to the Study of Its Function *Frontiers in Cell and Developmental Biology* 5**,** 96.
WHITLEY, E., & BALL, J. 2002. Statistics review 6: Nonparametric methods. *Critical care,* 6**,** 509–513.
ZHANG, Y., CHEN, X., GUEYDAN, C. & HAN, J. 2018. Plasma membrane changes during programmed cell deaths. *Cell Research,* 28**,** 9-21.
ZINK, F. E. 1997. The AAPM/RSNA Physics Tutorial for Residents. *Imaging and Therapeutic Technology,* 17**,** 1259-1268.

Appendix A

Raw data from proton experiment weeks

Table 9 Raw data showing the median fluorescence values measured by flow cytometry for the A549 cell line from proton irradiation in May

Treatment	Position Bragg peak	Effective dose [Gy]	LET	Median fluorescence, control	Median fluorescence, irradiated	Ratio
1 frac. à 2 Gy	A	2	10	4832	5702	1.18
	A	2	10	4658	5480	1.18
	C	2	40	4721	8460	1.79
	C	2	40	4662	10570	2.27
1 frac. à 4 Gy	A	4	10	4636	7205	1.55
	A	4	10	4781	7286	1.52
	C	4	40	4713	12513	2.65
	C	4	40	4772	13997	2.93
1 frac. à 8 Gy	A	8	10	4842	11853	2.45
	A	8	10	4788	11046	2.31
	C	8	40	4765	13257	2.78

Table 10 Raw data showing the median fluorescence values measured by flow cytometry for the A549 cell line from proton irradiation in February

Treatment	Position Bragg peak	Effective dose [Gy]	LET	Median fluorescence, control, BOTH AB	Median fluorescence, control, ONLY SEC. AB	Median fluorescence, irradiated, BOTH AB	Median fluorescence, irradiated, ONLY SEC. AB	Ratio
1 frac. à 4 Gy	A	4	10	3544	3292	6249	5904	1.37
	A	4	10	3500	3275	6205	5912	1.30
	C	4	40	3588	3286	9294	8785	1.69
	C	4	40	3565	3260	9191	8686	1.66
2 frac. à 4 Gy	A	8	10	4732	4494	10503	9985	2.18
	C	8	40	4415	3863	14093	13035	1.92
	C	8	40	4562	4130	12802	11624	2.73
1 frac. à 8 Gy	A	8	10	3453	3284	8322	8225	0.57
	A	8	10	3473	3261	8190	8069	0.57
	C	8	40	3604	3360	8763	8376	1.59
	C	8	40	3667	3274	9338	8735	1.53
2 frac. à 8 Gy	A	16	10	4911	4525	13312	12278	2.68
	A	16	10	4767	4355	13180	12147	2.51
	C	16	40	4864	4472	13405	12411	2.54

	C	16	40	5033	4454	13801	12599	2.08

Table 11 Raw data showing the median fluorescence values measured by flow cytometry for the T98G cell line from proton irradiation in May

Treatment	Position Bragg peak	Effective dose [Gy]	LET	Median fluorescence, control	Median fluorescence, irradiated	Ratio
1 frac. à 2 Gy	A	2	10	7727	7927	1.03
	A	2	10	6114	6671	1.09
	C	2	40	7319	9325	1.27
	C	2	40	6199	9143	1.48
1 frac. à 4 Gy	A	4	10	7696	8035	1.04
	A	4	10	6509	7187	1.10
	C	4	40	7366	10808	1.47
	C	4	40	6515	10394	1.60
1 frac. à 8 Gy	A	8	10	5926	9202	1.55
	A	8	10	7426	10007	1.35
	C	8	40	6033	11132	1.85
	C	8	40	8462	14700	1.74

Table 12 Raw data showing the median fluorescence values measured by flow cytometry for the T98G cell line from proton irradiation in November

Treatment	Position Bragg peak	Effective dose [Gy]	LET	Median fluorescence, control	Median fluorescence, irradiated	Ratio
1 frac. à 2 Gy	A	2	10	884	770	0.87
	A	2	10	1452	1578	1.09
	C	2	40	1116	4890	4.38
	C	2	40	662	3473	5.25
2 frac. à 2 Gy	A	4	10	413	-598	-1.45
	A	4	10	547	-258	0.47
	C	4	40	346	-200	-0.58
	C	4	40	598	-1317	-2.20
1 frac. à 4 Gy	A	4	10	450	96	0.21
	A	4	10	361	-100	-0.28
	C	4	40	708	145	0.20
	C	4	40	727	210	0.29
1 frac. à 8 Gy	A	8	10	651	1270	1.95
	A	8	10	1274	1721	1.35
	C	8	40	768	311	0.40

	C	8	40	2002	2286	1.14

Table 13 Raw data showing the median fluorescence values measured by flow cytometry for the T98G cell line from proton irradiation in February

Treatment	Position Bragg peak	Effective dose [Gy]	LET	Median fluorescence, control	Median fluorescence, irradiated	Ratio
1 frac. à 4 Gy	A	4	10	1596	1739	1.09
	A	4	10	1405	1231	0.88
	C	4	40	1952	2487	1.27
	C	4	40	1614	2301	1.43
2 frac. à 4 Gy	A	8	10	3524	2250	0.64
	A	8	10	3120	1168	0.37
	C	8	40	2621	1226	0.47
	C	8	40	2423	1307	0.54
1 frac. à 8 Gy	A	8	10	1503	1594	1.06
	C	8	40	1685	1919	1.14
	C	8	40	992	3920	3.95
2 frac. à 8 Gy	A	16	10	2603	1200	0.46
	A	16	10	3165	1487	0.47

	C	16	40	2390	1517	0.63
	C	16	40	2891	893	0.31

Appendix B

Linear regression

February, A549 cell line

The Wilcoxon signed-rank test gave a p-value of 0.0018, again significant, indicating a clear distinction between the control samples and the irradiated samples.

The fluorescence as a function of dose can be seen in Figure 56 and the fluorescence as a function of LET can be seen in Figure 57.

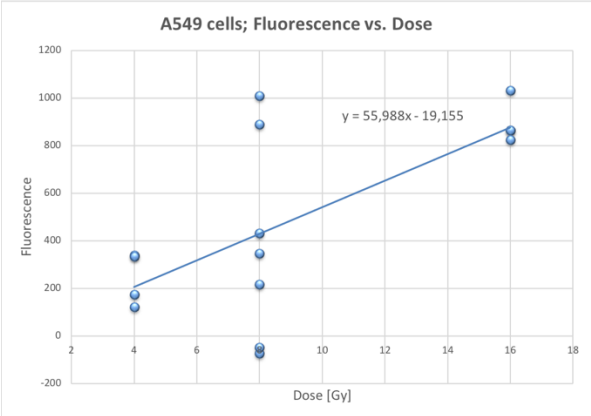

Figure 56 February; fluorescence as a function of dose for A549 cells irradiated with protons. The blue data points represent the irradiated cells. The line shows the linear fit of the data points.

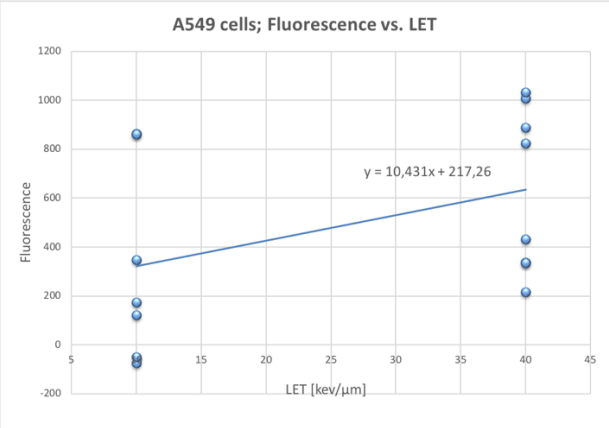

Figure 57 The same data are plotted as fluorescence as a function of LET where low-LET (front of Bragg peak) is assigned a value of 10 whereas the high-LET (back of Bragg peak) is assigned a value of 40.

In this case, the statistical output from the linear regression analysis showed a stronger relationship for the fluorescence as a function of dose (*p-value*: 0.006, $r^2 \sim 0.45$ and $r^2_{adj} \sim 0.41$) than the analysis of the fluorescence as a function of LET (*p-value*: 0.122, $r^2 \sim 0.17$ and $r^2_{adj} \sim 0.11$) which was not statistically significant.

The multivariate linear regression with dose and LET as the independent variables gave a p-value of 0.002 for dose-dependence and a p-value of 0.03 for LET-dependence. The variance in the fluorescence that can be attributed to dose and LET (r^2) was 0.64 and the adjusted coefficient of determination, r^2_{adj}, was 0.58. Consistent with the data from May, the linear

relationship is strongest when both dose and LET are taken into account. However, the statistics from February are weaker than those from May.

Again, the data was plotted with the ratio of the irradiated samples to the control samples for dose dependence (Figure 58) and LET dependence (Figure 59).

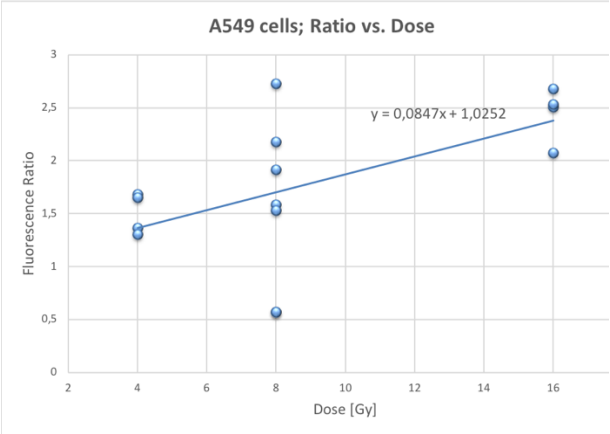

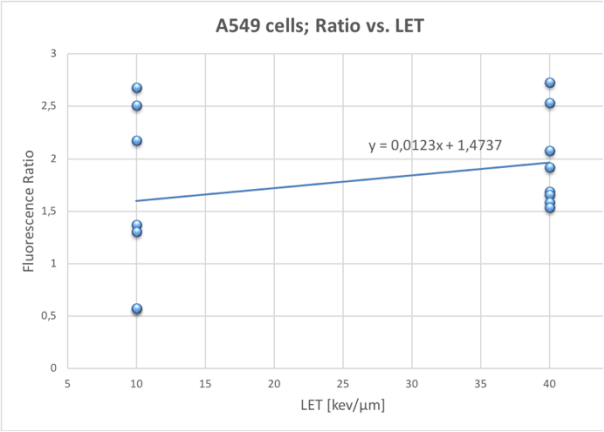

Figure 58 The ratio of the fluorescence of the irradiated samples to the control cells are displayed as a function of dose

Figure 59 The ratio of the fluorescence of the irradiated samples to the control cells as a function of LET

The linear regression analysis of the fluorescence ratios of irradiated samples to control samples were not significant for LET-dependence (*p-value* = 0.314) but significant for dose-dependence (*p-value* = 0.024, r^2 ~ 0.33 and r^2_{adj} ~ 0.28).

The multivariate analysis of the ratios was significant for the dose-variable (*p-value* = 0.02) but not for the LET-variable (*p-value* = 0.216). The r^2-value and r^2_{adj} were 0.42 and 0.32 respectively.

November and February, T98G cell line:

The proton data for the T98G cell line from November and February did not give a statistically significant result when applying the Wilcoxon signed-rank test. The data was therefore excluded from further analysis by linear regression. However, a quick scatter plot display was generated out of curiosity. The results can be seen in Figure 60-Figure 63.

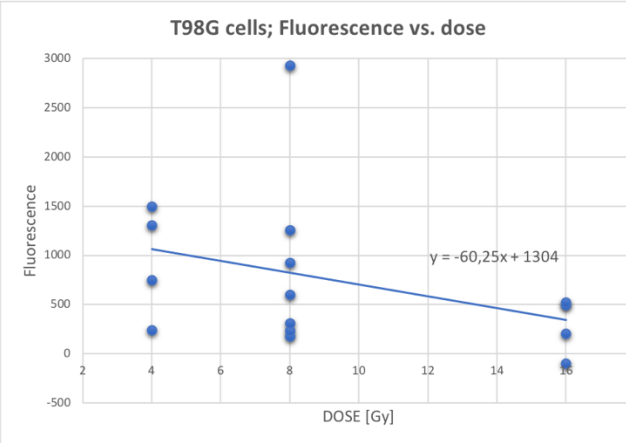

Figure 60 February; the fluorescence as a function of dose. The linear fit shows a negative relationship with dose

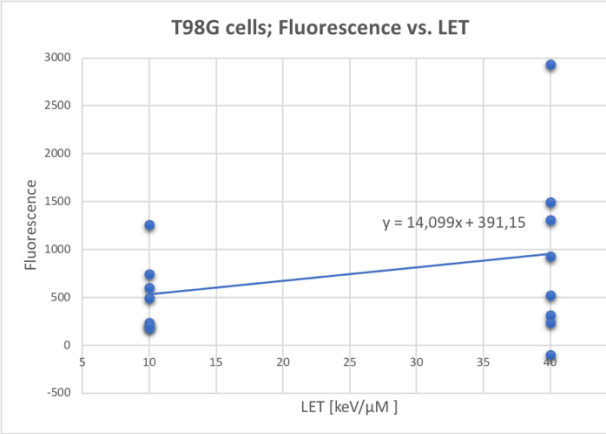

Figure 61 When plotting the same data as a function of LET the linear fit is positive.

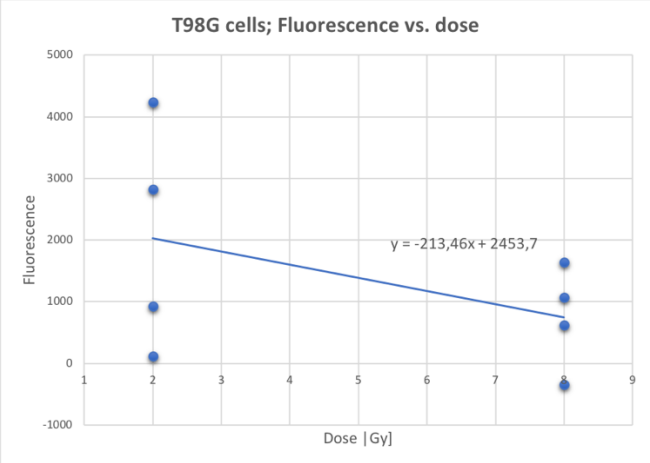

Figure 62 November; also the proton data of the T98G cell line from November shows that there seems to be a negative, linear relationship between the fluorescence as a function of dose.

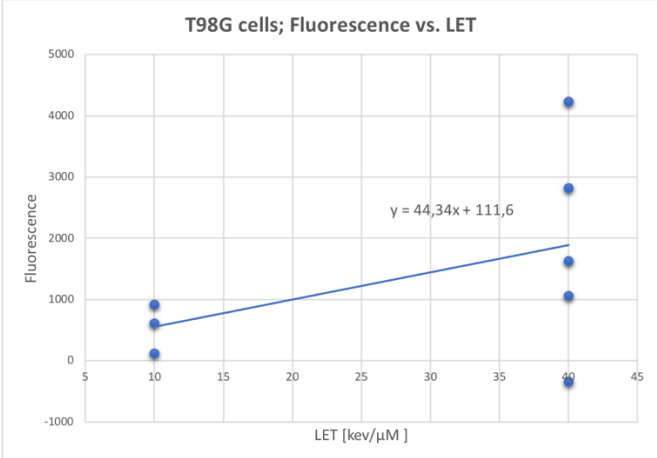

Figure 63 When plotting the fluorescence as a function of LET, the linear relationship appears positive.

Figure 60 and Figure 62 display the fluorescence as a function of dose for November and February. As can be observed, the linear fit shows a negative relationship for both experiments. The LET-dependence displayed in Figure 61 and Figure 63 indicates a positive relationship with this variable. No further analysis was performed for these data.

Appendix C

Calreticulin assay protocol

1. Harvest untreated control sample: Remove medium, rinse dish with **7.5 ml PBS** for big bottle. Add **4 ml TrypLE** Express. Incubate. Wash a few times with the TrypLE. Add **10 ml medium** without removing TrypLE, and transfer to tube. Centrifuge the 14 ml suspension at 200 xg for 5 min.

2. Aspirate the supernatant, and resuspend the cell pellet **1µl DyLight** per 100µl medium for barcoding. Incubate in dark with al. foil for 30 minutes, at room temperature.

3. In the meanwhile, harvest the remaining treated samples as described in step 1; Remove medium and dispose, rinse dish with **5 ml PBS** and dispose and add **2ml TrypLE** Express. Incubate. Wash a few times with the TrypLE. Add **4ml medium** without removing TrypLE and transfer to tube. Centrifuge at 200 xg for 5 min. Aspirate.

4. Resuspend the cell pellets in **10 ml PBS**.

5. Add **PBS** to the DyLight stained sample up to 10 ml, and centrifuge at 200 xg for 5 min. Aspirate. Repeat! Aspirate. Resuspend the pellet in an appropriate volume i.e. **100 microliter/sample BSA/PBS**, and add 100 microliter portions of the barcoded mock sample to each of the other treated samples. Mix well.

6. Split each sample equally to a secondary antibody control, and centrifuge all the samples at 200 xg for 5 minutes. Put on ice.

7. Aspirate the supernatants and resuspend the pellets in **100µl BSA/PBS** with primary anti-CRT antibody (0.5 microliter ab2907/100 µl BSA). Resuspend the pellets of the secondary antibody controls in **100 microliter BSA**. Incubate in dark for 30 minutes on ice.

8. Add **3ml PBS** to each sample, and centrifuge at 200 xg for 5 minutes. Aspirate the supernatant, repeat once.

9. Resuspend the pellets in **100µl BSA/PBS** with secondary antibody (0.25 µl Alexa Fluor 488/100 µl BSA. Incubate in dark for 30 minutes, on ice.

10. Add **3ml PBS** to each sample, and centrifuge at 200 xg for 5 minutes. Aspirate the supernatant, repeat once.

11. Resuspend the pellets in **500µl 1X PBS**. Transfer to flow cytometry tubes, and store at 4°C until flow cytometric analysis.

12. Prior to flow cytometric analysis, add **1µl propidium iodine** (PI) 1,0 mg/ml to the samples, for live/dead staining.

Appendix D

Python scripts used for bar plot displays

X-ray data

```
# -*- coding: utf-8 -*-
"""
Created on Fri Jul 19 11:41:51 2019

@author: emmathingstad
"""
import numpy as np
import matplotlib.pyplot as plt

plt.figure(figsize=(7, 9))
plt.subplots_adjust(hspace = 0.5)


plt.subplot(3,1,1)

sept = [1.93, 2.35]
dev_sept = [0.1, 0.1]
objects = ('1f, 8Gy', '1f, 8Gy')
x = np.arange(len(objects)) #x-axis like mange punkt som ant.barer

for i, v in enumerate(sept):
    plt.text(i-.38, -0.5+sept[i], sept[i], fontsize=8) #tall pa toppen av
barer

bar_width = -0.35

CRT = plt.bar(x+0.5*bar_width, sept, bar_width, color='b', align='edge',
alpha=0.4, yerr=dev_sept) #lage barplot
plt.xticks(x+bar_width, objects)
plt.xlim(-0.7,1)
plt.xlabel('Treatment')
plt.ylabel('Fluorescence')
plt.title('X-ray irradiation; September, ratio irradiated/control',
fontsize=14)
plt.yticks([])


plt.subplot(3,1,2)

nov = [1.78, 2.91, 2.17, 4.15]
dev_nov = [0.1, 0.1, 0.1, 0.1]
objects = ('1f, 4Gy', '2f, 4Gy', '1f, 8Gy', '2f, 8Gy')
x = np.arange(len(objects)) #x-axis like mange punkt som ant.barer

for i, v in enumerate(nov):
    plt.text(i-0.45, -0.5+nov[i], nov[i], fontsize=8) #tall pa toppen av
barer
```

```
bar_width = -0.35

CRT = plt.bar(x+0.5*bar_width, nov, bar_width, color='g', align='edge',
alpha=0.4, yerr=dev_nov) #lage barplot
plt.xticks(x+bar_width, objects)
plt.xlim(-0.8,3.1)
plt.xlabel('Treatment')
plt.ylabel('Fluorescence')
plt.title('X-ray irradiation; November, ratio irradiated/control',
fontsize=14)
plt.yticks([])

plt.subplot(3,1,3)

jan = [1.09, 0.97, 1.44]
dev_jan = [0.1, 0.1, 0.1]
objects = ('1f, 4Gy', '1f, 8Gy', '2f, 8Gy')
x = np.arange(len(objects)) #x-axis like mange punkt som ant.barer

for i, v in enumerate(jan):
    plt.text(i-.4, -0.3+jan[i], jan[i], fontsize=8) #tall pa toppen av
barer

bar_width = -0.35

CRT = plt.bar(x+0.5*bar_width, jan, bar_width, color='r', align='edge',
alpha=0.4, yerr=dev_jan) #lage barplot
plt.xticks(x+bar_width, objects)
plt.xlim(-0.8,2.1)
plt.xlabel('Treatment')
plt.ylabel('Fluorescence')
plt.title('X-ray irradiation; January, ratio irradiated/control',
fontsize=14)
plt.yticks([])
```

Protondata February

```
#protondata, bar chart
import numpy as np
import matplotlib.pyplot as plt


P_means = [1.38, 1.0, 2.41, 1.0] #CRT-values c/a T98G

objects = ('1f, 4Gy','2f, 4Gy','1f, 8Gy','2f, 8Gy') #dose-regime


dev = [0.13, 0.28, 0.55, 0.34] #st.dev

x = np.arange(len(objects)) #x-axis like mange punkt som ant.barer

for i, v in enumerate(P_means):
    plt.text(i-.65, -0.5+P_means[i], P_means[i], fontsize=8) #tall pa
toppen av barer

bar_width = -0.35
```

```
CRT = plt.bar(x+bar_width, P_means, bar_width, color='b', align='edge',
alpha=0.4, yerr=dev) #lage barplot
plt.xticks(x+bar_width, objects) #x-axis labels

plt.xlabel('Treatment', fontsize=14)
plt.ylabel('Fluorescence', fontsize=14)
plt.ylim(0,3.5) #set limit to y-axis
plt.xlim(-1,3.5)
plt.yticks([])

dev2 = [0.03, 0.17, 0.02, 0.1] #st.dev
P2 = [1.25, 1.07, 2.74, 0.89] #CRT-values c/a A549
#P22 = P2[1:]

CRT2 = plt.bar(x, P2, bar_width, color='g', align='edge', alpha=0.4,
yerr=dev2)


for i, v in enumerate(P2):
    plt.text(i-.31, -0.5+P2[i], P2[i], fontsize=8)

plt.legend(['T98G','A549'])
plt.title('Proton irradiation; February, ratio back of BP/front of BP',
fontsize=14)

"""

P_means = [0.98, 1.35, 0.51, 0.50,  1.06,  2.55,  0.47,  0.47] #CRT-values
c/a T98G

objects = ('1f, 4Gy; pos a', '1f, 4Gy; pos c', '2f, 4Gy; pos a', '2f, 4Gy;
pos c', '1f, 8Gy; pos a','1f, 8Gy; pos c','2f, 8Gy; pos a', '2f, 8Gy; pos
c') #dose-regime


#dev = [0.13, 0.28, 0.55, 0.34] #st.dev

x = np.arange(len(objects)) #x-axis like mange punkt som ant.barer

for i, v in enumerate(P_means):
    plt.text(i-.85, -0.2+P_means[i], P_means[i], fontsize=8) #tall pa
toppen av barer


bar_width = -0.45

CRT = plt.bar(x+bar_width, P_means, bar_width, color='b', align='edge',
alpha=0.4) #lage barplot
plt.xticks(x+bar_width, objects, rotation='vertical') #x-axis labels

plt.xlabel('Treatment', fontsize=14)
plt.ylabel('Fluorescence', fontsize=14)
plt.ylim(0,3.5) #set limit to y-axis
plt.xlim(-1,7.1)
plt.yticks([])

#dev2 = [0.03, 0.17, 0.02, 0.1] #st.dev
P2 = [ 1.34, 1.67,  2.18,2.32,0.57,1.56, 2.59,2.31] #CRT-values c/a A549
#P22 = P2[1:]

CRT2 = plt.bar(x, P2, bar_width, color='g', align='edge', alpha=0.4)
```

```
for i, v in enumerate(P2):
    plt.text(i-.41, -0.2+P2[i], P2[i], fontsize=8)

plt.legend(['T98G','A549'], loc='best')
plt.title('Proton irradiation; February, ratio irradiated/control',
fontsize=14)
"""
```

Protondata May

```
# -*- coding: utf-8 -*-
"""
Created on Sat May 11 17:16:55 2019

@author: emmathingstad
"""

import numpy as np
import matplotlib.pyplot as plt

T98G_c_a = [1.30, 1.43, 1.23] #2, 4, 8Gy + noAB 2,4Gy



objects = ('1f, 2Gy', '1f, 4Gy','1f, 8Gy') #dose-regime


dev = [0.08, 0.05, 0.08] #st.dev

x = np.arange(len(objects)) #x-axis like mange punkt som ant.barer

for i, v in enumerate(T98G_c_a):
    plt.text(i-.65, -0.5+T98G_c_a[i], T98G_c_a[i], fontsize=8) #tall pa
toppen av barer

bar_width = -0.35

CRT = plt.bar(x+bar_width, T98G_c_a, bar_width, color='b', align='edge',
alpha=0.4, yerr=dev) #lage barplot
plt.xticks(x+bar_width, objects) #x-axis labels

plt.xlabel('Treatment', fontsize=14)
plt.ylabel('Fluorescence', fontsize=14)
plt.ylim(0,3) #set limit to y-axis
plt.xlim(-1,2.5)
plt.yticks([])

dev2 = [0.12, 0.05, 0.03] #st.dev
A549_c_a = [1.72, 1.82, 1.17] #2, 4, 8Gy + utenAB 2,4 Gy


CRT2 = plt.bar(x, A549_c_a, bar_width, color='g', align='edge', alpha=0.4,
yerr=dev2)


for i, v in enumerate(A549_c_a):
    plt.text(i-.31, -0.5+A549_c_a[i], A549_c_a[i], fontsize=8)
```

```
plt.legend(['T98G','A549'])
plt.title('Proton irradiation; May, ratio back of BP/front of BP',
fontsize=14)



import numpy as np
import matplotlib.pyplot as plt

T98G_c_a = [1.06, 1.37, 1.07, 1.53, 1.45, 1.79] #2, 4, 8Gy + noAB 2,4Gy



objects = ('1f, 2Gy; pos a', '1f, 2Gy; pos c','1f, 4Gy; pos a', '1f, 4Gy;
pos c', '1f, 8Gy; pos a','1f, 8Gy; pos c') #dose-regime



x = np.arange(len(objects)) #x-axis like mange punkt som ant.barer

for i, v in enumerate(T98G_c_a):
    plt.text(i-.65, -0.5+T98G_c_a[i], T98G_c_a[i], fontsize=8) #tall pa
toppen av barer

bar_width = -0.35

CRT = plt.bar(x+bar_width, T98G_c_a, bar_width, color='b', align='edge',
alpha=0.4) #lage barplot
plt.xticks(x+bar_width, objects, rotation='vertical') #x-axis labels

plt.xlabel('Treatment', fontsize=14)
plt.ylabel('Fluorescence', fontsize=14)
plt.ylim(0,3) #set limit to y-axis
#plt.xlim(-1,4.5)
plt.yticks([])


A549_c_a = [1.18, 2.03, 1.54, 2.79, 2.37, 2.78]


CRT2 = plt.bar(x, A549_c_a, bar_width, color='g', align='edge', alpha=0.4)


for i, v in enumerate(A549_c_a):
    plt.text(i-.31, -0.5+A549_c_a[i], A549_c_a[i], fontsize=8)

plt.legend(['T98G','A549'], loc='best')
plt.title('Proton irradiation; May, ratio irradiated/control', fontsize=14)
```

Protondata November

```
#protondata, bar chart
import numpy as np
import matplotlib.pyplot as plt


#c/a
```

```
"""
P_means = [4.92, 0.47] #CRT-values c/a T98G

objects = ('1f, 2Gy', '1f, 8Gy') #dose-regime


dev = [0.14, 0.51] #st.dev

x = np.arange(len(objects)) #x-axis like mange punkt som ant.barer

for i, v in enumerate(P_means):
    plt.text(i-.42, -0.3+P_means[i], P_means[i], fontsize=8) #tall pa
toppen av barer

bar_width = -0.25

CRT = plt.bar(x+bar_width, P_means, bar_width, color='b', align='edge',
alpha=0.4, yerr=dev) #lage barplot
plt.xticks(x+1.5*bar_width, objects) #x-axis labels

plt.xlabel('Treatment', fontsize=14)
plt.ylabel('Fluorescence', fontsize=14)
plt.ylim(0,5.5) #set limit to y-axis
plt.xlim(-1,1.0)
plt.yticks([])



dev2 = [0.1, 0.1, 0.1, 0.1] #st.dev
P2 = [1.25, 1.07, 2.74, 0.89] #CRT-values c/a A549
#P22 = P2[1:]

CRT2 = plt.bar(x, P2, bar_width, color='g', align='edge', alpha=0.4,
yerr=dev2)


for i, v in enumerate(P2):
    plt.text(i-.31, -0.5+P2[i], P2[i], fontsize=8)


plt.legend(['T98G'])
plt.title('Proton irradiation; November, ratio back of BP/front of BP',
fontsize=14)
"""

P_means = [0.87, 1.09, 4.38, 5.25] #CRT-values c/a T98G

objects = ('1f, 2Gy; pos a', '1f, 2Gy; pos c', '1f, 8Gy; pos a', '1f, 8Gy;
pos c') #dose-regime


#dev = [0.14, 0.51, 0.1, 0.1] #st.dev

x = np.arange(len(objects)) #x-axis like mange punkt som ant.barer

for i, v in enumerate(P_means):
    plt.text(i-.46, -0.3+P_means[i], P_means[i], fontsize=8) #tall pa
toppen av barer

bar_width = -0.25
```

```
CRT = plt.bar(x+bar_width, P_means, bar_width, color='b', align='edge',
alpha=0.4) #lage barplot
plt.xticks(x+1.2*bar_width, objects) #x-axis labels

plt.xlabel('Treatment', fontsize=14)
plt.ylabel('Fluorescence', fontsize=14)
plt.ylim(0,5.5) #set limit to y-axis
plt.xlim(-1,3.2)
plt.yticks([])
"""
dev2 = [0.1, 0.1, 0.1, 0.1] #st.dev
P2 = [1.25, 1.07, 2.74, 0.89] #CRT-values c/a A549
#P22 = P2[1:]

CRT2 = plt.bar(x, P2, bar_width, color='g', align='edge', alpha=0.4,
yerr=dev2)


for i, v in enumerate(P2):
    plt.text(i-.31, -0.5+P2[i], P2[i], fontsize=8)
"""

plt.legend(['T98G',], loc='best')
plt.title('Proton irradiation; November, ratio irradiated/control',
fontsize=14)
```